Piezoelectric Buckling Actuators: Form Reduction, Bidirectional Control, and Optimal Switching

by

Lluís Enric Peñalver-Àguila

B.S., Mechanical Engineering
Carnegie Mellon University, 2007

SUBMITTED TO THE DEPARTMENT OF MECHANICAL ENGINEERING IN PARTIAL FULFILLMENT OF THE REQUIREMENTS FOR THE DEGREE OF

MASTER OF SCIENCE IN MECHANICAL ENGINEERING
AT THE
MASSACHUSETTS INSTITUTE OF TECHNOLOGY

June 2014

Signature redacted

Author.....
Department of Mechanical Engineering
May 9, 2014

Signature redacted

Certified by.....
H. Harry Asada
Ford Professor of Mechanical Engineering
Thesis Supervisor

Signature redacted

Accepted by.....
David E. Hardt
Chairman, Department Committee on Graduate Students
Department of Mechanical Engineering

Piezoelectric Buckling Actuators: Form Reduction, Bidirectional Control, and Optimal Switching

by

Lluís Enric Peñalver-Àguila

Submitted to the Department of Mechanical Engineering
on May 9, 2014, in partial fulfillment of the
requirements for the degree of
Master of Science in Mechanical Engineering

ABSTRACT

Piezoelectric stack actuators are generally described as having large force density, high bandwidth response, and limited yet precise displacement properties. As a result, these actuators have been widely applied to precision positioning devices, acoustical and optical instruments, and within vibration control mechanisms. Techniques to efficiently amplify this limited displacement have been central to recent piezo-actuator research. One such technique exploits structural buckling to achieve displacement amplification gains greater than 100 while limiting energy transmission loss into the amplifying mechanism. This thesis first surveys the recently developed piezoelectric buckling actuator and identifies critical design elements that may be further optimized to reduce the mechanism's form factor. Focus is directed towards simultaneously reducing structural compliance and mass in the actuator's frame and rotational joints. Use of carbon fiber and new geometry improves structural efficiency while increased joint stiffness is shown through design and material changes. Discussion then shifts to the non-deterministic output of a standalone buckling actuator and methods to address it. A design is presented which couples the buckling actuator to an energy storing mechanism that alternates output direction by enforcing hysteretic force-displacement behavior using a closed loop cam-follower path. Finally, a dual buckling actuator mechanism is discussed which exhibits both quasi-static and dynamic motion properties through asynchronous activation control. Through the use of phase-plane analysis, an optimal switching control law is described. Prototypes of single and dual buckling actuator mechanisms are shown, and experimental performance is presented.

Thesis Supervisor: H. Harry Asada
Title: Associate Professor

Acknowledgements

First and foremost, I would like to thank Professor Asada for bringing me into the d'Arbeloff lab and for providing me with much guidance in my research. I greatly appreciate his patience in explaining new concepts to me, his trust in my research and design decisions, and lastly his supportive guidance when I faced discouraging research results. I know that the skills I have developed as a researcher are directly attributable to his efforts.

I received generous funding support through Sumitomo Heavy Industries without which I would not have studied such an interesting and promising area of actuator research. This funding was also crucial for the production of several prototypes for which I am very proud to have had a part in designing, building, and testing.

I am also grateful to the MIT ODGE office for providing me with the Diversity Fellowship through the kind generosity of A. Neil Pappalardo (MIT '64). This fellowship allowed me to attend MIT prior to finding a research lab without concern for the financial burden.

My ability to complete this thesis would not have been possible without a great deal of help from all of my fellow d'Arbeloff lab colleagues. In particular, I must thank several members who went above and beyond in guiding me, and whom I consider close colleagues and friends. I thank James Torres and Shinichiro Tsukahara for welcoming me onto their research project, providing a solid foundation to our work, and sharing the spotlight of our collaborative deliverables. The long hours and late nights in the lab would not have been as enjoyable without the frequent conversations with Anirban Mazumdar, Devin Neal, and Federico Parietti that bettered my technical writing, problem solving, and presentation skills.

Last but not least, I would like to thank my parents and brother for their support throughout my graduate school experience. Thank you for pushing me to truly comprehend the privilege of attending MIT and for providing a constant reminder that no matter what challenges I face I can always count on you to provide guidance and reassurance.

Contents

List of Figures

List of Tables

Chapter 1

1. Introduction

Piezoelectric actuators represent a class of capacitive actuator which can provide operational bandwidths as high as 10 kHz as well as power densities of $10^8 - 10^9$ W/m^3 [1]. These performance features along with their compact size have promoted widespread usage of and research into piezo-actuators for small scale actuation in acoustics, vibration control and precision positioning [2] [3] [4] [5]. Yet, piezoelectric actuators remain severely limited in output stroke. Unamplified piezoelectric stack actuators, such as Lead Zirconate Titanate (PZT), only achieve free strain on the order of 0.1% [6]. This small strain and the typical 10^1 mm length scale of commercially available piezo-actuators leads to displacement on the order of $1x10^{-2}$ mm which is generally not sufficient for many larger scale mechatronics or robotics. Thus, a requirement for improved output stroke leads to the utilization of displacement amplification devices.

Piezoelectric displacement amplification comes in many forms. Amplification techniques are generally categorized into internally, externally, or frequency leveraged designs. Internally leveraged devices such as stack, bender, and unimorph actuators use carefully selected material geometries to amplify displacement [6]. Stroke output is limited by the internal stiffness of the actuators. Stack actuators are simple and effective internally leveraged actuators that are commonly used as building blocks in many externally leveraged and frequency leveraged designs. Frequency leveraged mechanisms rely on resonant frequencies to impart motion through friction drives. These devices have been developed for rotary motion, providing unlimited

rotation, or linear motion using "inchworm" and other locomotion techniques to move along a track [7] [8]. While the displacement gain is significant with these inchworm designs, friction drives suffer the disadvantage of requiring high normal forces to maintain appropriate load driving capability.

Many types of externally leveraged, or mechanically amplified, actuators have been developed. These include the flextensional, lever, Moonie and Cymbal mechanisms, or variations thereof, which typically produce amplification of one order of magnitude [9]. Recent research has been performed on amplification mechanisms that exploit non-linear structural buckling. These are of particular interest because they achieve displacement amplification of two orders of magnitude in a single actuator stage [10]. As described in [8] these buckling amplification mechanisms produce "mono-polar" or "bi-polar" stroke at the output node. They are also characterized by significantly non-linear force behavior. Control of the output direction may not be deterministic, and must be enforced through additional actuators, some form of asymmetric stiffness as described in [10] , [11] or through an additional switching mechanism.

This thesis seeks to expand upon existing piezoelectric buckling actuator research by studying some general methods to improve their form factors, to gain deterministic output control of standalone units, and to explore the dynamics and optimal coordination of rapidly actuated multi-unit devices. The objective at the core of this work is to identify additional design and control parameters which if tuned appropriately may make these piezoelectric buckling actuators more readily applicable in mechatronics. The thesis is organized in the following manner. The first content chapter begins with a look at the operating principles behind piezoelectric buckling actuators and the critical areas for careful design or improvement. The third chapter provides alternate material and geometry choices for the buckling actuator components most susceptible to structural compliance and thus loss of energy transmission. The next chapter develops a switching mechanism which couples to base buckling unit and provides deterministic alternating output based on an energy storage and release device. The final content chapter expands upon a previously designed multi-unit buckling actuator. In this iteration, the multi-unit device incorporates a flexure-less design which has been shown previously to improve energy transmission through the amplification mechanism [12].

Chapter 2

2. Fundamentals of Piezoelectric Buckling Actuators

Although the design of the piezoelectric buckling actuator is not the focus of this thesis, this actuator is the basis of the two composite devices described later. It is important to review the nomenclature, operating theory, and understand the key parameters which affect the static and dynamic performance of this building block device. The original development of the buckling actuator concept and the secondary development of a flexure free amplification mechanism is the work of Dr. Devin Neal, and Ph.D. candidate James Torres, respectively, as described in [10] [11] [12] [13] [14].

2.1. Nomenclature and Operating Concept

A simple schematic of a piezoelectric buckling actuator is shown in Figure 2-1. The piezo-stack actuators used in this design are made of Lead-Zirconate Titanate and as such are abbreviated "PZT" in the remainder of this thesis. At its rest condition, the buckling actuator is positioned with stability in a straight configuration with two PZT stack actuators aligned collinearly. Rotational joints exist between the pair of PZTs, one representing the output node known as the "keystone", and between each PZT and the "side blocks" which are fixed to "ground". When the PZTs are energized through an applied voltage, they experience a positive length change, "Z", causing the aligned components of the actuator to "buckle" and the output keystone to move

either up or down. Upon discharging the PZTs, the keystone returns to the central position via the "preload compensation spring" (PCS), visible in Figure 2-2, as it returns to its rest length. The positive and negative output stroke along the y-direction is termed "mono-polar" if it occurs only to one side of the aligned condition, and "bi-polar" if it occurs to both sides. The buckling actuator in this configuration has the potential for full bipolar stroke but the stroke direction is not deterministic. In other words, the output direction cannot be controlled without additional and external input.

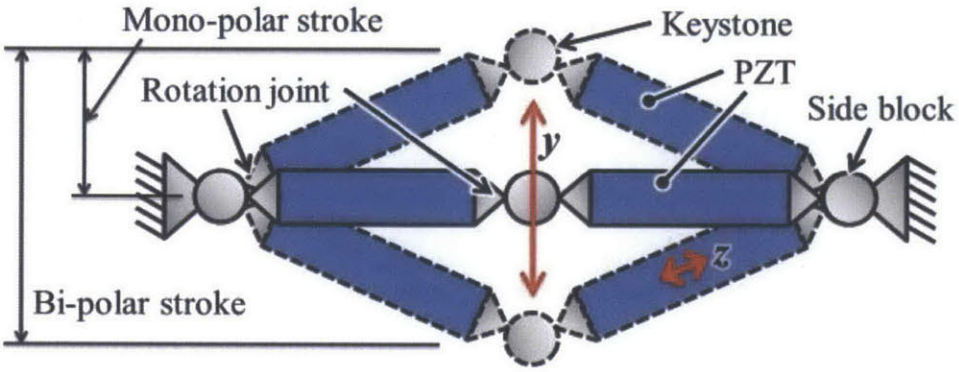

Figure 2-1: Schematic depiction of "Mono-polar" and "Bi-polar" displacement of a stable buckling actuator.

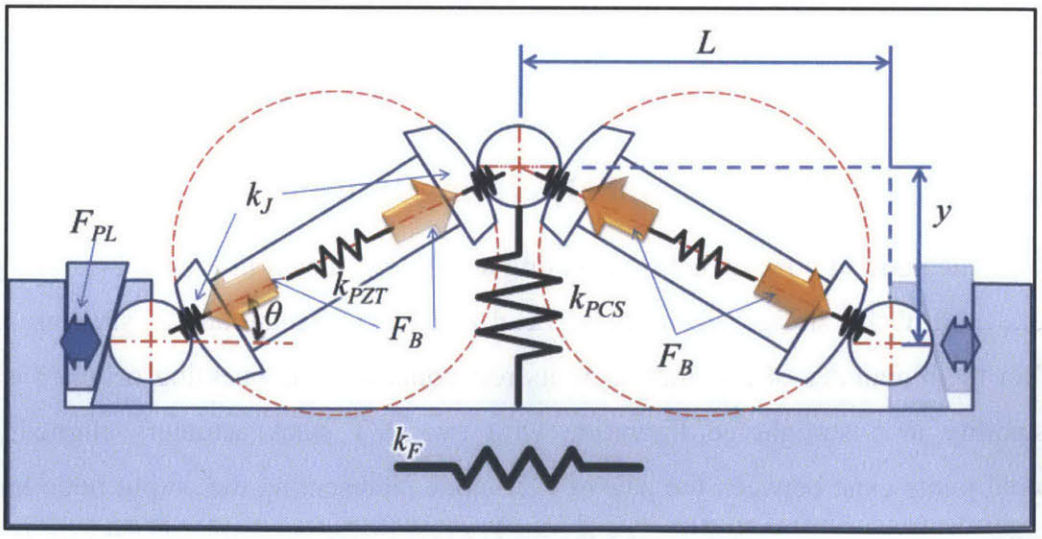

Figure 2-2: Schematic of a flexure free buckling actuator with labelled structural compliances, PZT output forces, and geometric properties.

2.2. Description of Primary Components

The buckling actuator implemented in the two devices described in this thesis is based on the more recently designed flexure free mechanism incorporating stiff rolling contact joints instead of flexures. This flexure free mechanism has an amplification gain of two orders of magnitude, high force transmission through the mechanism, and a virtual length scale which may be tuned independently of the physical size of the device [14].

A more clarified representation of the flexure free mechanism is shown in the CAD image of Figure 2-3. Here, as in Figure 2-2, the three rotational joints from the schematic are physically realized by four rolling contact joints. These joints occur between the side blocks or "End Caps" and the "PZT Caps", and the keystone and "PZT Caps". These caps and the PZTs are within a single frame connected to "ground". As shown in the figure below, the connection of the PCS to the keystone occurs through a component known as the coupler.

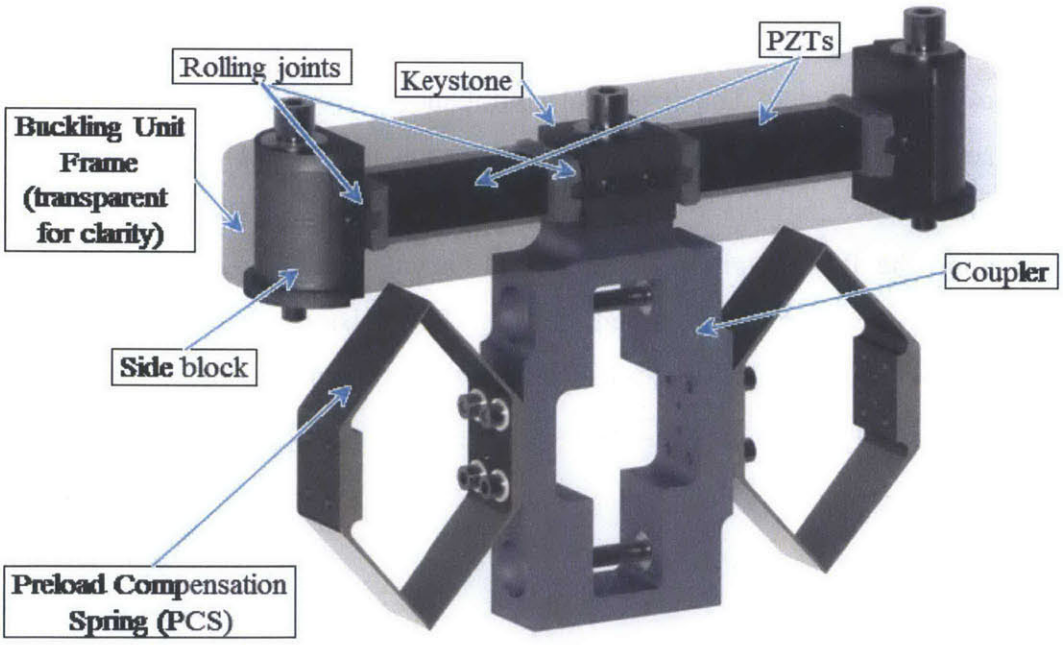

Figure 2-3: CAD Image of a Piezoelectric Buckling Actuator Variant with Labels.

2.3. Theoretical Force Properties

The complete and detailed analysis of the flexure free buckling actuators may be reviewed in [14]. The following discussion does not fully analyze these actuators but rather provides a survey of the system parameters that are later modified in the new composite devices for proper functionality.

The buckling actuator shown schematically in Figure 2-2 includes structural compliances, geometric properties and PZT forces. Structural compliance is considered in the frame structure, $\mathbf{k_F}$, each of the four rolling contact joints, $\mathbf{k_J}$, and in the PZT stack actuators themselves, $\mathbf{k_{PZT}}$. The preload compensation spring stiffness is also shown as $\mathbf{k_{PCS}}$. Geometrically, the keystone position is described by a rotation angle, $\boldsymbol{\theta}$, and a displacement distance, $\mathbf{y}$. The characteristic length of the buckling unit is shown as $\mathbf{L}$. This corresponds to the distance between the centers of the keystone and a side block when the system is in the aligned, singular configuration.

The buckling actuator is symmetric about the keystone centerline and force-displacement properties of a single side may be modelled as representative. This is done in the lumped parameter model of Figure 2-4. Variables for the PZT output force, $\mathbf{F_B}$, and an initial preload force, $\mathbf{F_{PL}}$, are now included. The structural compliances of the frame and the rolling contact joints are also combined into a single term, $\mathbf{k_{SERIAL}}$, as in Eq. (2.1). The force-displacement behavior of this lumped parameter model is described by Eq. (2.2) assuming the displacement, $\mathbf{Z_2}$, occurs along the PZT longitudinal direction. Viewing Figure 2-2, the force-displacement behavior in the y-direction is described by Eq. (2.3). Using geometric and trigonometric approximations of Eq. (2.4), the force-displacement performance in the y-direction, assuming small rotations, is expanded as in Eq. (2.5).

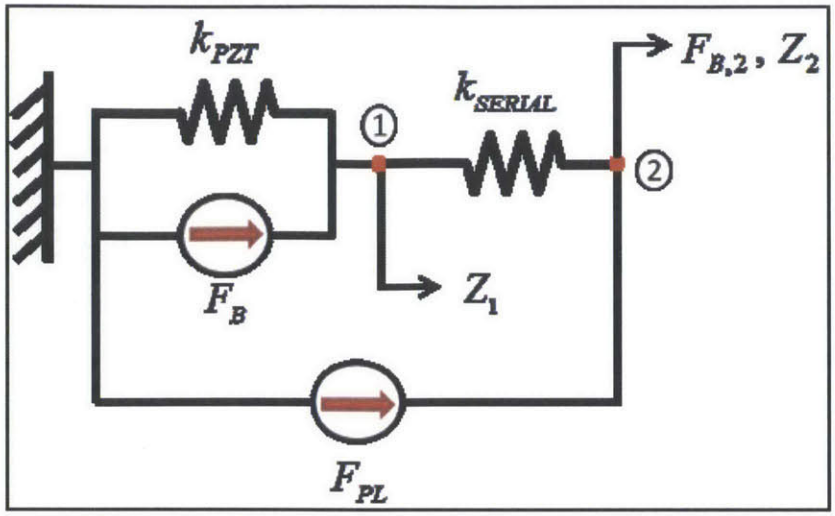

Figure 2-4: Lumped parameter model of a single side of the flexure free buckling actuator

$$k_{SERIAL} = \left(\frac{2}{k_J} + \frac{1}{2k_F} \right)^{-1} \tag{2.1}$$

$$F_{B,2} = F_B \left(\frac{k_{SERIAL}}{k_{SERIAL} + k_{PZT}} \right) + F_{PL} - \left(\frac{k_{SERIAL} * k_{PZT}}{k_{SERIAL} + k_{PZT}} \right) * Z_2 \tag{2.2}$$

$$F_y = 2F_{B,2} \sin(\theta) + F_{PCS} \tag{2.3}$$

$$\begin{cases} Z_2 \cong \dfrac{y^2}{2L} \\ \sin\theta \approx y / L \end{cases} \tag{2.4}$$

$$F_y = 2\left(F_B \left(\frac{k_{SERIAL}}{k_{SERIAL} + k_{PZT}} \right) + F_{PL} - \left(\frac{k_{SERIAL} * k_{PZT}}{k_{SERIAL} + k_{PZT}} \right) \frac{y^2}{2L} \right) \frac{y}{L} - k_{PCS} y \tag{2.5}$$

A plot of the characteristic output performance of the piezoelectric buckling actuator is shown in Figure 2-5. This figure clearly indicates the significantly non-linear force-displacement behavior

of the actuator. In particular, it is important to note that with the PZTs energized the actuator provides zero force at both the start and end of its stroke, and maximum "outward" force at mid-stroke. With the PZTs de-energized, the buckling actuator has a maximum "inward" force at either maximum displacement position, and that force decays towards zero at zero displacement. In this particular plot, there exists a balanced relationship between the PCS stiffness and the preload force, "threshold preloading", which allows the actuator to be stable at zero displacement with the PZTs off. This need not be the case, and "over-preloading" is a situation which is exploited in the switching mechanism described in Chapter 4. It is also clear from this plot that the system output direction, i.e. positive or negative displacement, is not deterministic. A force or displacement perturbation in one direction while the actuator's PZTs are energized and the keystone sits at the central location will bias the output stroke in that same direction.

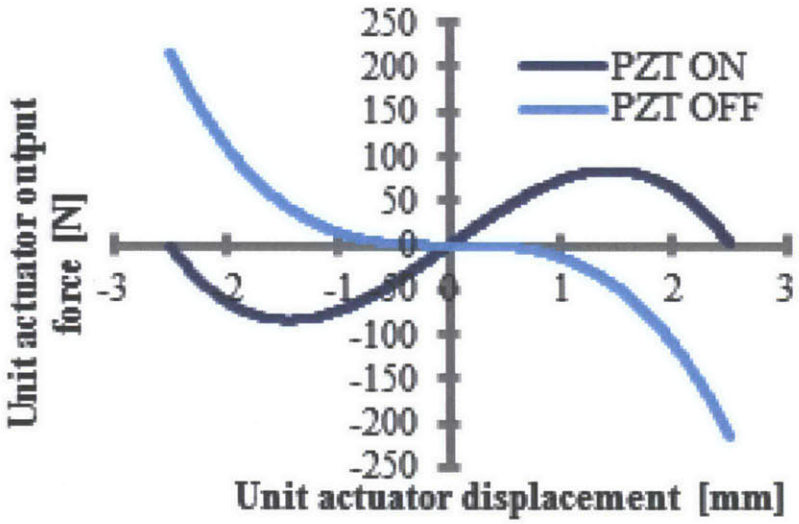

Figure 2-5: Output Property of Piezoelectric Roller Contact Buckling PZT Actuators

Chapter 3

3. Form Factor Reduction in Piezoelectric Buckling Actuators

3.1. Motivation

The piezoelectric stack actuators discussed in Chapter 1 have high force density and are compact devices, but lack displacement output and therefore require amplification to make them more useful in mechatronic or robotic applications. The buckling amplification technique described in Chapter 2 represents an effective method to achieve this amplification however initial prototypes discussed in [12], [14] are proof of concept designs with no requirement for size and weight optimization. Before they can be used effectively in robotic applications, these buckling actuators must be re-designed to have similar performance but with reduced form factors. This section of the thesis describes two methods to reduce the size and weight of the buckling actuators and increase the structural stiffness and energy transmission. An exemplary design is shown which was incorporated into the "Poly-Actuated Linear Motor" of [8].

As is described in [14], the amplification gain of the flexure free buckling mechanism is primarily determined by the characteristic length, **L**, which is defined by the radii of the rolling contact joints and the PZT length. Once this gain value has been selected, the next important design consideration is to provide a high serial stiffness, $\mathbf{k_{SERIAL}}$, as defined in Chapter 2, to maximize force transmission from the PZTs to the keystone output. The serial stiffness, defined in Eq. (2.1), is described by the joint and frame compliances which are discussed next.

3.2. Improving Stiffness, Energy Transfer & Reducing Weight

3.2.1. Alternate Geometry & Material Choices for the Rolling Contact Joint

Rolling contact joints occur between the end caps and PZT caps, and the keystone and PZT caps. In each case, the rolling surfaces represent at least one set of co-planar contacting curves defined by the radii of each cap. Previous iterations of the joint design, [14], used "crowned" or compound curvature contact surfaces to reduce the risk of applying bending loads to the PZTs. In the exemplary design discussed here, the contacting surfaces are parallel cylinders. This parallel cylindrical design represents the optimal contact set with the highest possible stiffness.

Hertzian contact theory provides the solution for contact stiffness and stress between a pair of parallel contacting cylinders. Differential contact stiffness is defined by Eq. (3.1) and maximum compressive stress by Eq. (3.2). In Eq. (3.1), $\mathbf{D_1}$ and $\mathbf{D_2}$ refer to the diameters of the cylinders, **E** is the Young's modulus, **ν** is the Poisson's ratio, **P** is the applied load, and **W** is the contact length between the cylinders. The result of Eq. (3.1) is that the joint stiffness varies non-linearly with the applied load **P**, and nearly linearly with changes in the material properties and contact length. These relationships can be seen in the contour mapping of Figure 3-1 which represents the contact stiffness as a function of applied load and contact length. In this figure, the cap material properties, PZT properties, and cylinder diameters for the design implemented in [8] are used for **E**, **ν**, $\mathbf{D_1}$ and $\mathbf{D_2}$ variables.

A visual representation of the compressive stress defined by Eq. (3.2) can be seen in Figure 3-2. Contact stresses are typically very high even at low contact loads. However the contact surface area increases rapidly as load increases. As a result, contact stresses increase as the square root of applied load. This figure represents the maximum stresses for the implemented design geometry. At the full applied load and at the shortest contact length defined, the stresses approach approximately 2 GPa which is a typical stress limit for hardened bearing steels. Increasing the contact length parameter increases stiffness and decreases stress but with a diminishing return. Thus, the rolling contact joint design requires careful material selection for both stiffness and stress characteristics.

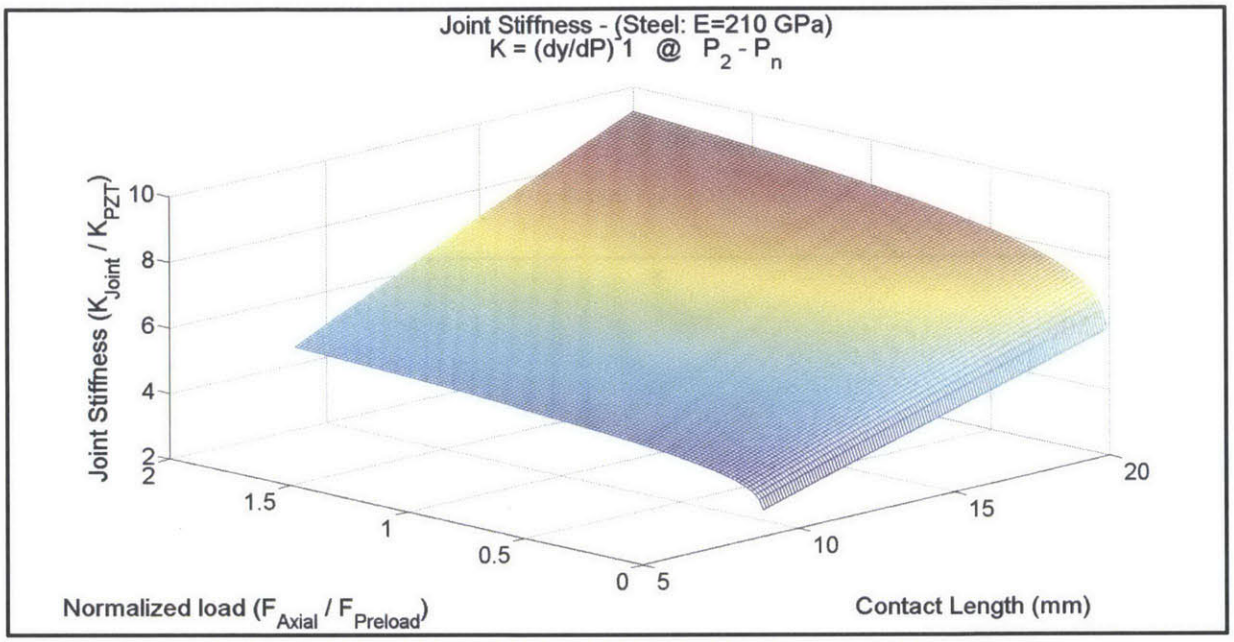

Figure 3-1: Normalized contact stiffness contour map as a function of normalized axial load and the contact length for a parallel cylindrical contact set made of steel.

$$k_J = \frac{\partial P}{\partial \delta} = \left[\frac{2(1-\upsilon^2)}{\pi E L} \left(\frac{2}{3} + \ln\left(\frac{4(D_1 + D_2)}{(1.60^2)\frac{P}{W}\frac{2(1-\upsilon^2)}{E}} \right) \right) \right]^{-1} \tag{3.1}$$

$$\sigma_{Comp} = 0.798 \sqrt{\frac{P}{W K_D C_e}}$$
$$K_D = \frac{(D_1 D_2)}{(D_1 + D_2)} \quad ; \quad C_e = \frac{2(1-\upsilon^2)}{E} \tag{3.2}$$

High strength bearing steel is the most commonly used material for rolling elements however alternate bearing materials exist which have mechanical properties that are advantageous in this application. Table 3-1 lists two additional materials, synthetic sapphire (Al_2O_3) and tungsten carbide, which have an elastic modulus 2 to 3 times larger than that of steel, respectively. From Eq. (3.1), this indicates that simply substituting the keystone, PZT cap and end cap material with the alternate materials will approximately double or triple the stiffness of a single joint. This attribute is listed in the last column of Table 3-1 showing values of the joint stiffness normalized to the PZT stiffness for the exemplary design. The required compressive strength of the alternate

materials matches or exceeds that of steel. In terms of mass, tungsten carbide is denser, but the cap components are relatively small and the caps may be designed such that a tungsten carbide "insert" is used just at the contacting portion of the cap. Additional normalized contact stiffness contour maps using the two alternate materials are shown in Figure 3-3 and Figure 3-4.

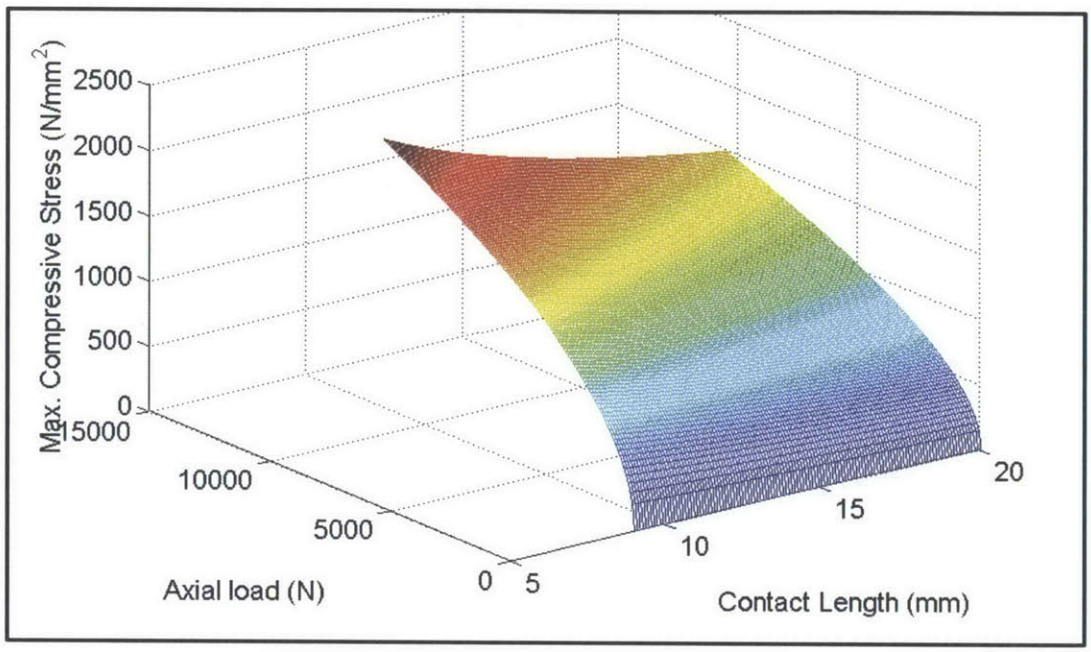

Figure 3-2: Maximum compressive stress as a function of axial load (contact load) and the contact length for the exemplary design parallel cylindrical contact set.

Material	Modulus of Elasticity (GPa)	Compressive Strength (GPa)	Density (g/cc)	k_J / k_{PZT} [-]
Bearing Steel	**210**	**2**	**7.85**	**6.645**
Synthetic Sapphire (Al_2O_3)	**450**	**2.05**	**4**	**12.61**
Tungsten Carbide	**600**	**5.3 – 7.0**	**14.5**	**17.22**

Table 3-1: Alternate Rolling Contact Bearing Materials: Mechanical Properties and Effective Normalized Joint Stiffness.

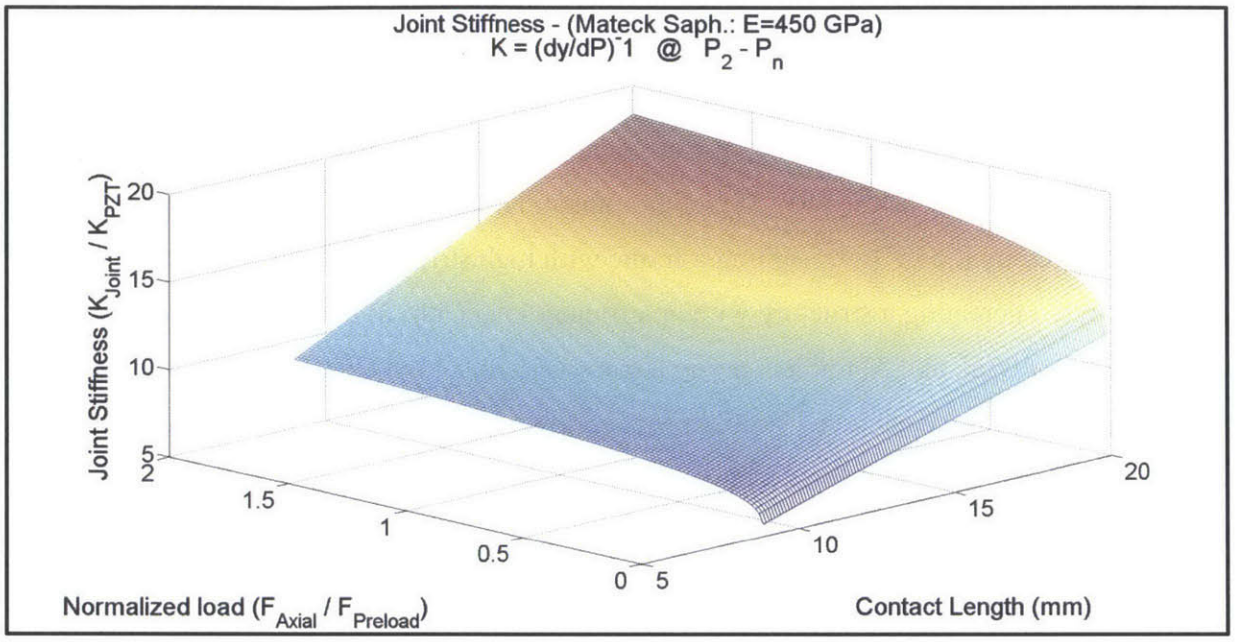

Figure 3-3: Normalized contact stiffness for the contact set made of synthetic sapphire.

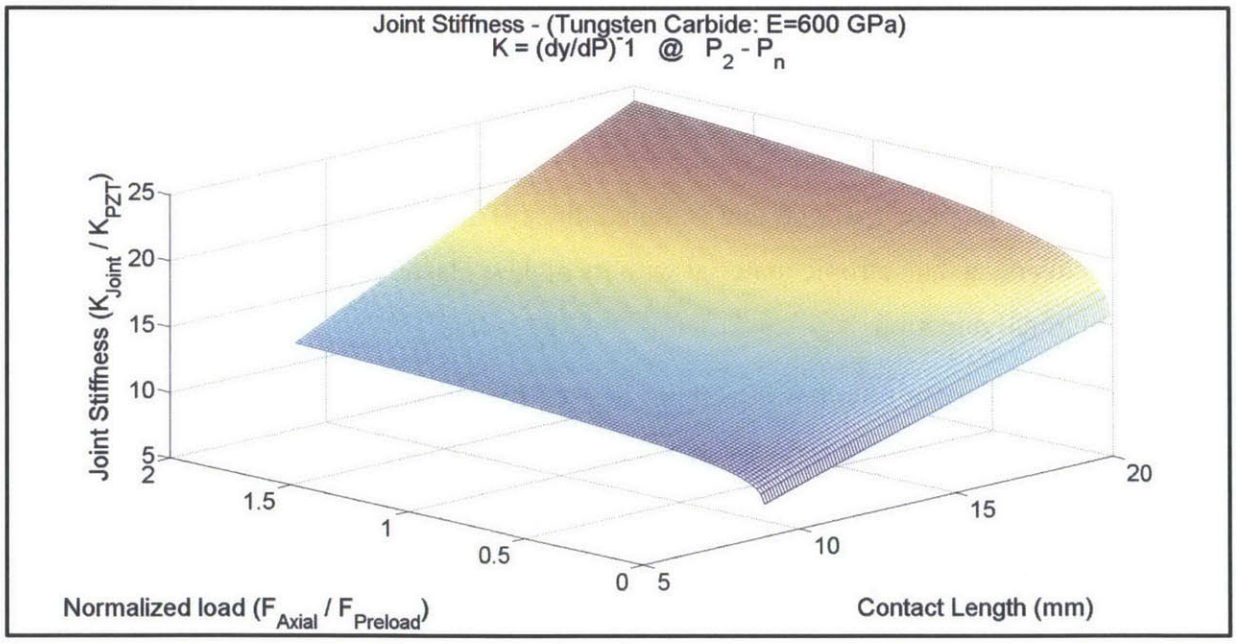

Figure 3-4: Normalized contact stiffness for the contact set made of tungsten carbide.

3.2.2. Carbon Fiber Material for the Actuator Frame

The stiffness of the buckling unit frame plays a role in the maximum output force that can be achieved by the buckling unit as described in Eq. (2.1) and Eq. (2.2). Maximizing this stiffness is critical in approaching the ideal force-displacement property, and also for increasing transmissibility, defined as the ratio of energy transmitted to the load divided by the maximum energy produced by the PZT. Designing a frame with high stiffness can be achieved in three primary ways: 1) creating a structure with an efficient load path, 2) maximizing the amount of load bearing material, and 3) implementing a material with a high elastic modulus. These three design objectives can be achieved simultaneously however in the interest of increasing force density and other size/weight form factors, the efficient load path geometry and high elastic moduli dominate the design space.

The loading produced during a buckling displacement cycle as described by Figure 2-1 is predominantly uniaxial along the centerline of the buckling mechanism. A combination of PZT force input and preload force, this axial force, $\mathbf{F_X}$, represented by red arrows in Figure 3-5, fluctuates between zero and approximately **11 kN** in the exemplary design. In contrast, the maximum force output at the keystone in the y-direction, $\mathbf{F_Y}$, assuming infinite serial stiffness is only **+/- 135 N**. Thus lateral load acting on the frame structure represents approximately 3% of the maximum axial load experienced by the frame. Therefore, a logical frame design would implement a geometry and material that is uniaxially stiff and strong. This also implies the advantage of using an anisotropic material with its highest elastic modulus oriented along the frame longitudinal direction

Unidirectional carbon fiber reinforced plastics (CFRP) achieve the above stiffness and strength properties by oriented carbon fibers along the dominant load path. As shown in Table 3-2, CFRP laminates have elastic moduli 2-3 times larger than steel, and a density of approximately 1/4 that of steel. Thus, the elastic modulus density for CFRP, measured in GPa/(g/cc), may be 8-10 times larger than that of steel. This roughly leads to a force density improvement of the same magnitude. The exemplary CFRP frame geometry implemented in the poly-actuated linear motor of [8] can be seen in Figure 3-6 which shows a side view and section view including the buckling mechanism internals. These frames are constructed using a high modulus carbon fiber comparable to material: K1392U listed in Table 3-2. Thus, a change of the

frame structure material to one with higher elastic modulus allows the same geometry or reduced cross-section geometry to be used while limiting structural compliance. Additionally, using a high modulus unidirectional carbon fiber aligned with the primary load axis allows a reduction of buckling actuator frame weight. As a result, energy transmission can be maintained or improved while force density is increased.

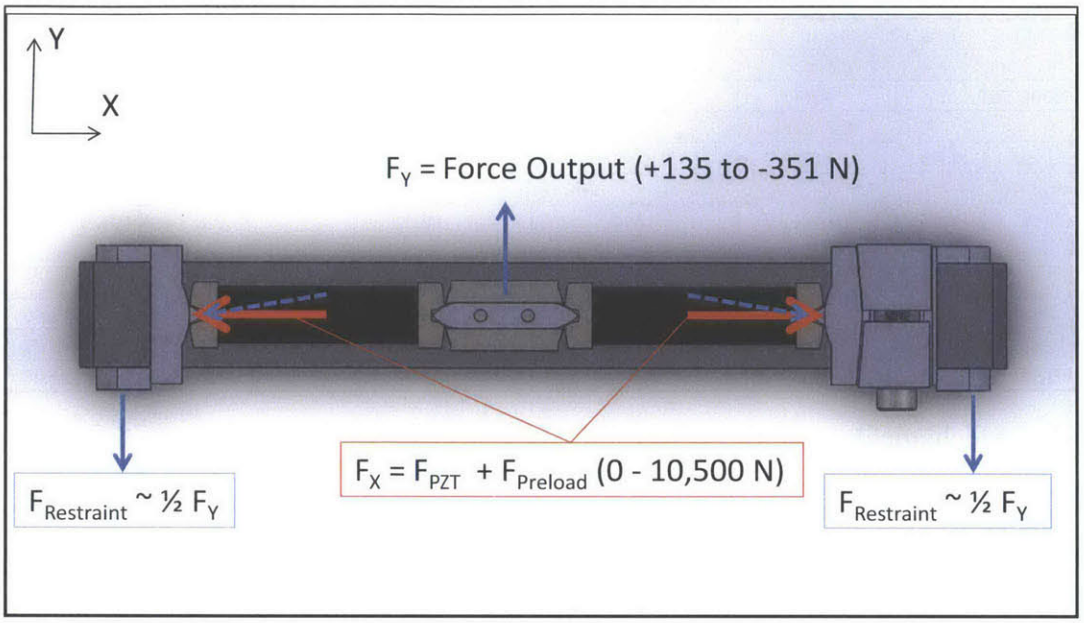

Figure 3-5: Internal forces experienced by the buckling unit frame. The red arrows indicate the dominant uniaxial loading from the preload and PZT force inputs.

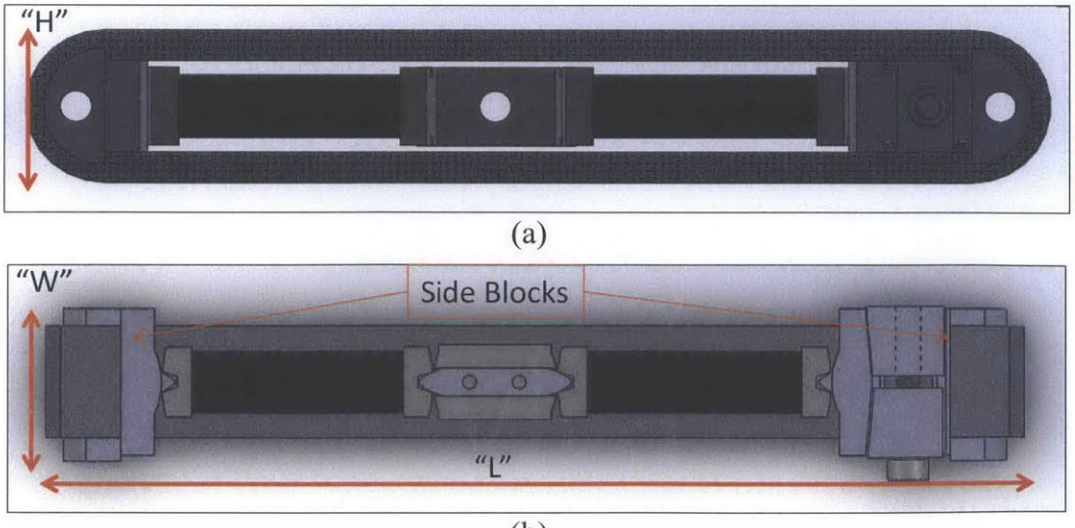

Figure 3-6: A side view (a) of the CFRP frame design indicating the tension structure, and a section view (b) showing the internal components.

Material	Density (g/cc^3)	Yield Strength (MPa)	Ultimate Strength (MPa)	Modulus of Elasticity (GPa)	Mod. E Density (Gpa/(g/cc^3)	Stress Density (Gpa/(g/cc^3)
Steels						
ASTM A36	7.85	250	475	200	25.48	31.85
Stainless 440	7.8	1280	1750	200	25.64	164.10
AISI 1020	7.87	330	450	200	25.41	41.93
AISI 4340	7.85	710	1110	205	26.11	90.45
Aluminum						
Al Aly 6061-T6	2.7	276	310	69	25.56	102.22
Titanium						
Ti-6Al-4V	4.43	880	950	114	25.73	198.65
Fiberglass						
S-Glass	2.46	-----	4890	86.9	35.33	1987.80
E-glass	2.77	-----	3445	80.3	28.99	1243.68
Carbon Fiber (Laminate Properties)						
K1352U	2.12	-----	2000	380	179.25	943.40
K1392U	2.15	-----	2100	460	213.95	976.74
K13D2U	2.21	-----	1800	560	253.39	814.48

Table 3-2: Mechanical properties of several types of structural materials including high strength steels and carbon fiber laminates.

Chapter 4

4. Design of a Switching Mechanism for Deterministic Alternating Output

4.1. Necessity for Bidirectional Control

Analysis in Chapter 2 indicates that a standalone buckling actuator with a kinematically singular "rest" configuration does not have deterministic output. As designed, the direction of the actuator's output stroke cannot be controlled internally and is subject to external force or displacement perturbations. Direction control can only be imposed by connecting multiple buckling actuators together, as described in [13], [10], and in the following chapter, or by introducing direction-biasing forces. The direction-biasing forces may be achieved statically through additional stiffness elements, as described in [11], or dynamically via inertial or magnetic forces. Whichever method is employed, achieving control authority over the output stroke direction is paramount in making the actuators useful and well behaved for standalone applications.

In this chapter, the design and analysis of a bi-stable, mechanically amplified, piezoelectric actuator incorporating a statically deterministic switching mechanism is presented. The piezoelectric buckling actuator is used as the base unit. This actuator is combined with an energy storing and switching mechanism that alternates output direction by enforcing hysteresis in the force-displacement behavior via a closed loop cam-follower path. First the design concept and analysis are presented. A brief discussion of alternative design options follows with emphasis on an exemplary solution being presented. Finally an experimental prototype is shown.

4.2. Design Concept

The objective of coupling a passive switching mechanism to a standalone piezoelectric buckling actuator is to achieve consistently deterministic, and alternating "bipolar" stroke without the use of additional active devices or external force inputs. The large "bipolar" stroke characteristic of the buckling actuator, shown in Figure 2-1, may then be exploited by a standalone unit. Ideally then, the considerable displacement and moderate force of this buckling amplification device may be utilized for a variety of applications while at the same time minimizing complexity and cost by using a minimum number of actuators. One such application might include the actuation of a "shift collar" within a two position transmission with neutral, high, and low gear modes. In this application, the standalone actuator would be connected directly, or through a linkage, to a shift collar. The shift collar would then be moved from a neutral "disengaged" location to either one of two maximum displacement locations corresponding to the high or low gear "engaged" positions. To function in this transmission or other general bi-modal applications, the design should meet the following functional requirements:

- **Deterministic Output:** Achieve an enforced output direction based only on an initial configuration of the device
- **Alternating Output:** Quasi-statically provide alternating stroke direction regardless of initial position
- **Latching:** Physically "lock" the output node at either full displacement position prior to additional control input
- **Stability:** Maintain output stroke stability against external force perturbations in all positions
- **Switch Activation:** Switch quasi-statically between bi-modal output stroke regions as a result of changing the piezoelectric energy states between on and off
- **Force Shaping:** Provide a method to "transform" the force-displacement behavior
- **Efficiency:** The device should not consume power at any static position

4.2.1. Design Flow

The conceptual design flow leading to the coupled buckling actuator – switching mechanism device is shown in Figure 4-1 below. As the flowchart indicates, the design objective is to achieve a compact, bidirectional actuator that is efficient under static conditions, primarily

corresponding to the aforementioned "latched" positions. A clear solution to achieve this compactness and zero-power consumption statically is to incorporate piezoelectric actuators due to their capacitive properties. Piezo-stack actuators are a good starting point, but their displacement is very limited reaching a maximum of approximately 0.1% strain. To amplify this stroke output, one effective design solution is to use the previously developed "flexure free" buckling amplification device. This buckling unit amplifies the stroke of the piezo-stack actuator by approximately two orders of magnitude, but exhibits a nonlinear force behavior and, if operating as a standalone unit, has a non-deterministic output direction.

The remaining design flow shown from this point forward in the flowchart represents the new contribution of the research contained in this thesis chapter. As is described in more detail in the following sections, the non-deterministic output property of the buckling unit can be circumvented by over-preloading the buckling unit such that it becomes bi-stable. This bi-stability limits the standalone buckling unit to "mono-polar" output stroke which can then be managed by the energy storage and release device incorporated into the switching mechanism. The remaining design challenge, dealing with the nonlinear force behavior, is addressed through a closed loop cam-follower path. Implementing a particular shape for the closed loop allows the nonlinear force behavior to be transformed, within some constraints, to another more desirable force behavior.

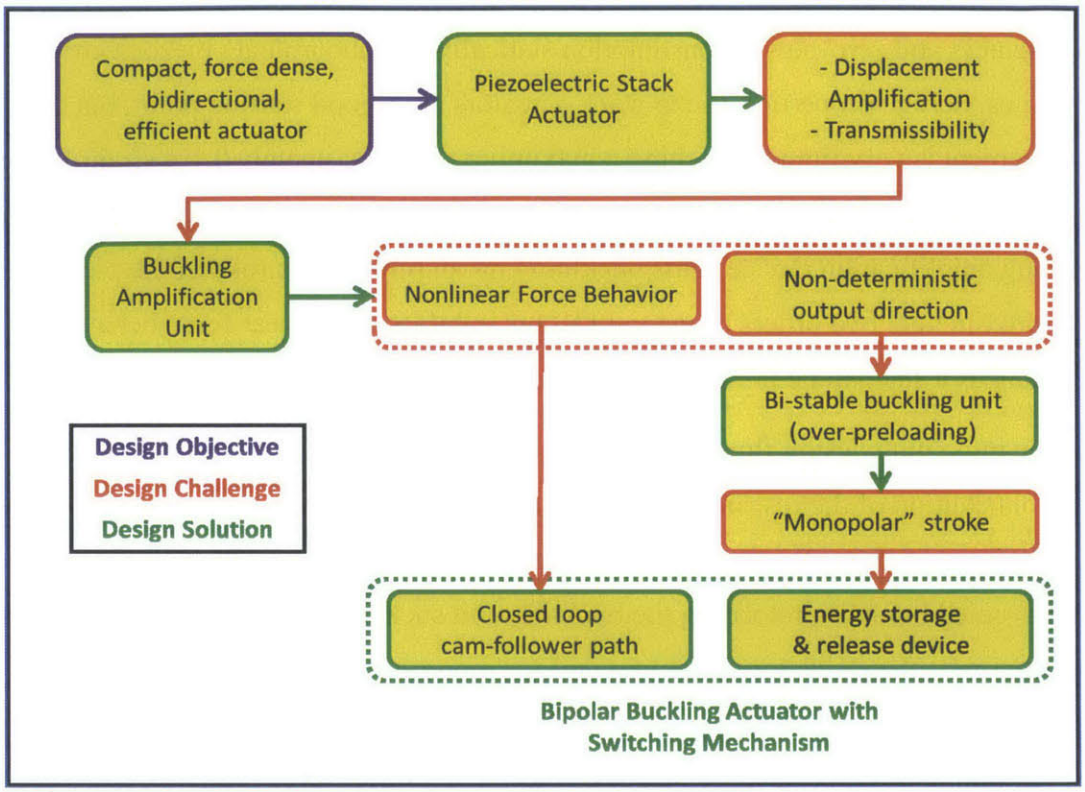

Figure 4-1: Design flow followed in the development of the coupled buckling unit – switching mechanism design. Design objective, challenges, and corresponding solutions are highlighted.

4.2.2. Basic Architecture

A conceptual CAD model of the coupled buckling unit – switching mechanism device is shown in Figure 4-2. Fig. 4-2(a) depicts the general layout of the device as well as the directions of motion of the buckling unit output node and the moving component of the switching mechanism, the cam plate. Fig. 4-2(b) indicates the primary components of the switching mechanism. The three fundamental components of the coupled device which convert electrical input to the piezo-stack actuators into deterministic alternating output of the buckling unit include:

- Cam-Plate with Cam-Follower Groove
- Latching Gate
- Cam Plate Spring

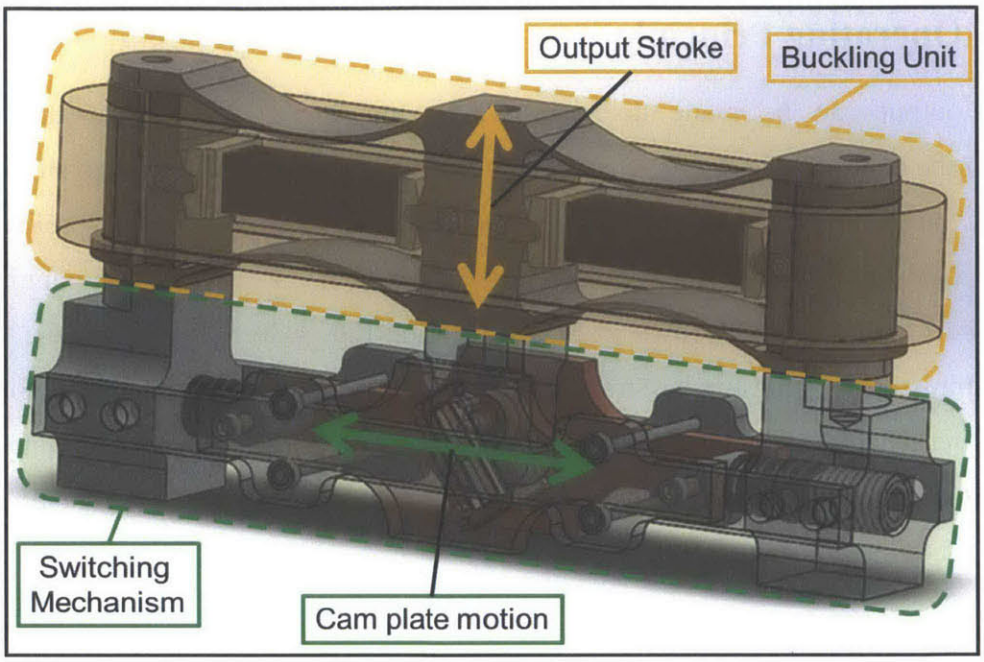

(a)

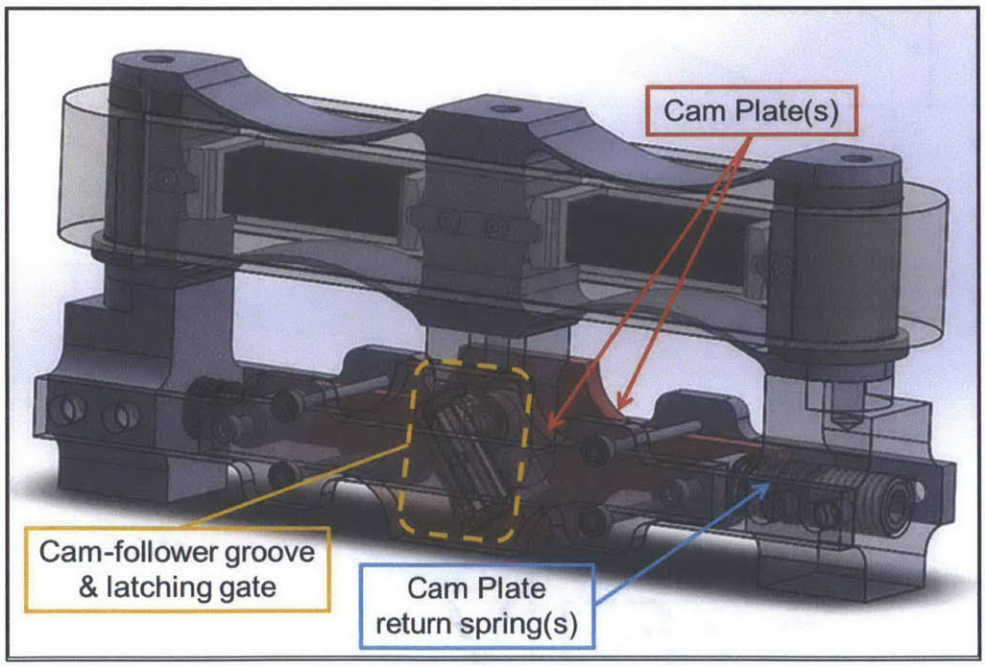

(b)

Figure 4-2: (a) A CAD model of the coupled buckling unit – switching mechanism indicating the motion directions of the buckling unit output node and the switching mechanism cam plate. (b) Labeled CAD model of the device indicating the three fundamental components.

4.3. Operating Principle

The actuator output can be made deterministic by introducing a force or displacement perturbation to the central, singular configuration. One method to do this involves slightly over-preloading the buckling actuator as shown schematically in Figure 4-3. Over-preloading the actuator leads to bi-stability with rest configurations at positions "A" and "B" of magnitudes +/- $Y_{BISTABLE}$, as described later. As shown in Fig. 4-3(a) and Fig. 4-3(c), energizing the PZT pair leads to deterministic and mono-polar stroke from A to A' and B to B', respectively. Fig. 4-3(b) illustrates the "reset" stroke; the distance between bi-stable positions which the buckling actuator cannot quasi-statically traverse without an additional external force input. Deterministic output is now achieved, but bipolar stroke is not.

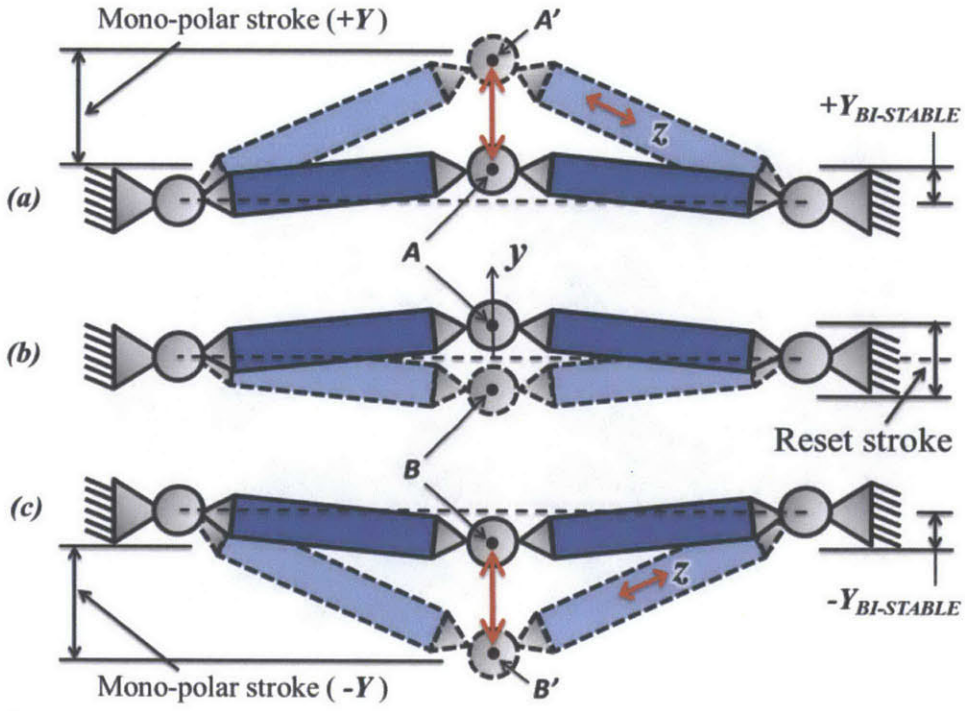

Figure 4-3: Schematic depiction of bi-modal displacement behavior of an over-preloaded buckling actuator. (a) Deterministic mono-polar displacement in (+) Y-region between A ←→ A', (b) Region corresponding to the "reset" stroke between A ←→ B which requires external force input, and (c) deterministic mono-polar displacement in (-) Y-region between B ←→ B'.

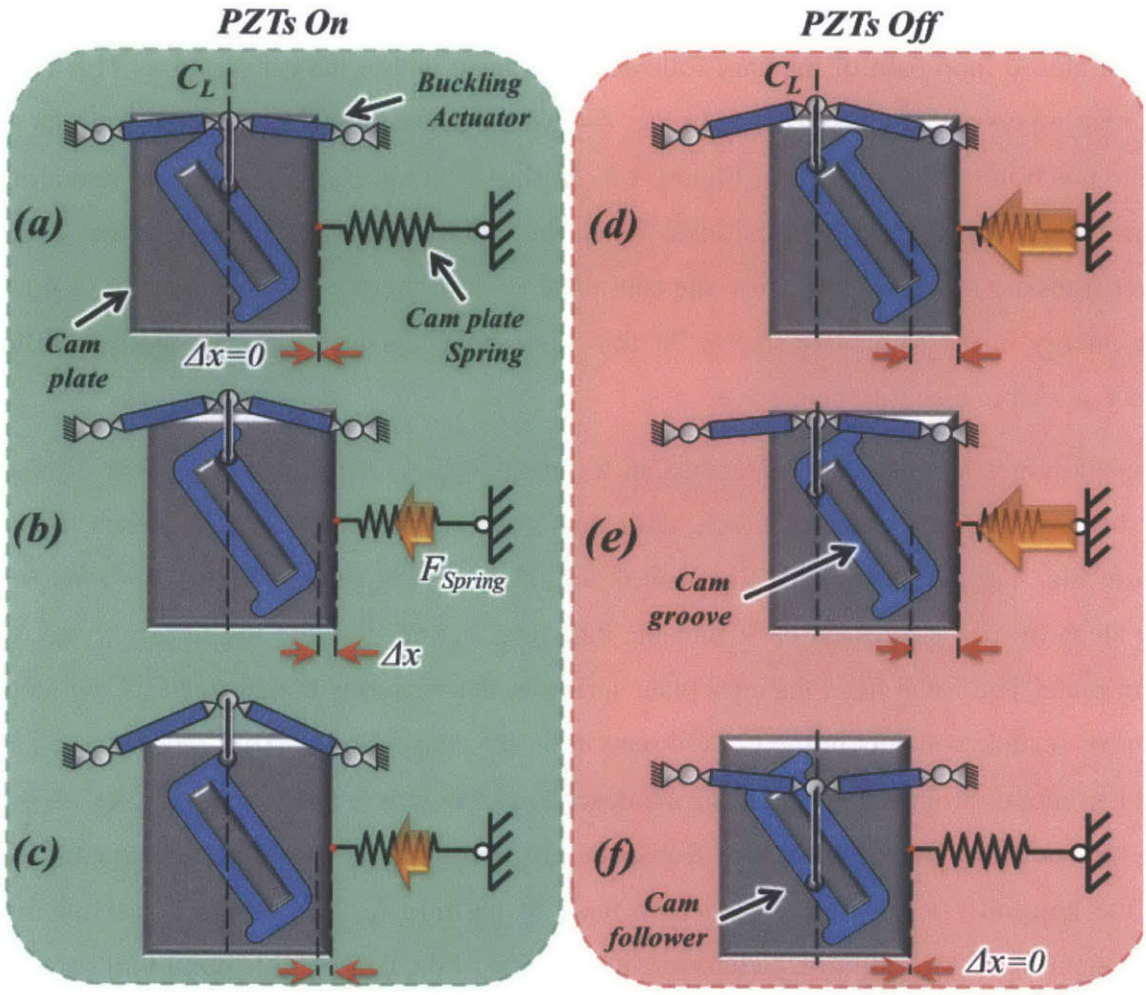

Figure 4-4: (a) Buckling actuator and cam-plate at their upper "rest" positions, (b) PZTs energized, cam follower shifts up, cam plate to the right, (c) cam-follower "latches", (d) PZTs de-energized, cam-follower shifts down, cam-plate shifts farther right, (e) cam-follower "resets" , cam plate spring forces buckling unit through the "reset" stroke, and (f) buckling actuator and cam-plate at lower "rest" positions.

The method proposed to achieve deterministic, alternating output and full bipolar range simultaneously is illustrated in Figure 4-4. In this schematic, an over-preloaded piezoelectric buckling actuator is coupled to the switching mechanism comprised of a translating cam plate connected to a return spring. The cam plate has one degree of freedom, lateral translation, and experiences a restoring force from the cam plate spring whenever it is displaced from its central rest position. A cam follower moving within a groove in the cam plate establishes the link between the buckling actuator force and displacement, the cam plate translation, and the cam plate spring restoring force.

The cam groove, cam plate spring, and a latching gate described in the next section, all enforce a closed loop path of the cam follower movement within the cam-groove. This leads to the alternating output of the keystone. In Fig. 4-4(a), the buckling actuator begins at the positive bi-stable position "A" described in Figure 4-3. At this location, both the buckling actuator and the cam plate are at their "rest" positions. When the PZTs are energized, the keystone and cam follower translate upwards, and cause the cam plate to shift laterally to the right, Fig. 4-4(b)/(c), storing energy in the cam plate spring. At full mono-polar displacement, A', the cam-follower latches in a visible notch in the groove.

Considering a latching gate described in the next section, if the PZTs are then discharged while the cam-follower is in this notch, the cam-follower continues along the closed loop path shown in Fig. 4-4(d)-(f). Between Fig. 4-4(e) and (f), the energy stored in the cam plate spring during steps (a)-(d) is released back into the buckling actuator through the restoring motion of the cam plate. The force from the cam plate spring in this region is transformed by the slope of the groove surface and acts in the (–) y-direction on the cam-follower. This causes the buckling actuator to move through the "reset" stroke described in Figure 4-3. The actuator device is now at the "B" position from Figure 4-3. Subsequently energizing and discharging the PZTs will move the keystone to position B' and then back to position A. This comprises a full bipolar displacement loop. Any additional charging/discharging of the PZTs at this point will continue to cycle the actuator through the alternating bipolar stroke.

4.4. Description of Primary Components

Cam Plate with Cam-Follower Groove

The consideration of an over-preloaded buckling actuator as the base component in this device requires the energy storing element to be at rest when the actuator is similarly at rest in either bi-stable position. Since the cam plate translates laterally as a function of keystone vertical position and is linked to the cam spring, the bi-stable conditions require that the cam plate be centered for two different y-positions of the keystone. The cam-follower groove must therefore have a hysteretic and closed loop path as shown in Figure 4-4. Ideally a smooth, continuously differentiable path would be chosen, however to satisfy the "latching" functional requirement, it is necessary to have a notch in the path. As a result, the schematic and the subsequent analysis

section assume a piecewise continuous path. Additionally, contact between the cam-follower and groove will occur on both the outer and inner surfaces of the groove depending on PZT energy state and cam follower location. Thus, an "island" of material defining the internal contact surface of the closed loop path is necessary.

Latching Gate

During PZT discharge, when the device is in the latched condition shown in Fig. 4-4(c), motion along the closed loop path indicated in steps (d)-(f) is not possible without a gate and moveable contact surface that prevents the cam-follower from back-tracking towards the position shown in Fig. 4-4(b). The latching gate must open during steps (a)-(c) to allow the cam-follower to pass from the first contact surface slope up to the latching notch. While the cam-follower is in the notch, the latching gate must then close to provide the first portion of the second contact surface slope. A variety of designs may be employed here to prevent this motion. The design of the gate used in the experimental prototype is shown in more detail in the analysis section.

Cam Plate Spring

The role of the cam plate spring is to provide a restoring force to the cam plate when it is shifted away from its central position. The energy stored in the spring is fed back to the buckling actuator keystone providing the necessary external force input to quasi-statically move it through the "reset" stroke, positions A to B & B to A, as shown in Figure 4-3. The return spring may have a simple linear or a more complex non-linear stiffness provided that it is chosen with the shape of the cam-groove path and the fundamental force-displacement properties of the selected buckling actuator in mind. Energy storage into the spring is allowable through any range of output stroke up to the reset position approximately shown in Fig. 4-4(e). All stored energy in the spring must then be released between the reset position and the opposite bi-stable location.

4.5. Theoretical Force-Displacement Properties

The following section describes the force-displacement characteristics of the switching mechanism individually and combined with a buckling actuator. To ensure that the device will

have quasi-static, alternating deterministic output, the combined force properties of the two components must display a hysteretic path in the force displacement domain as described below.

4.5.1. Preload Modifications

Reviewing the buckling actuator shown in Figure 2-1, one can see that it is stable at the central, aligned position when the PZTs are discharged. This is due to a condition where the preload compensation spring stiffness, $\mathbf{k_{PCS}}$, is tuned to a maximum desired preload force, $\mathbf{F_{PL}}$. In Figure 4-3, the buckling actuator is preloaded above this critical force value causing it to become unstable in the aligned condition, and exhibit bi-stability which is central to the design solution for deterministic output.

Eq. (4.1) describes the approximate desired design relationships between $\mathbf{k_{PCS}}$ and $\mathbf{F_{PL}}$, and provides the stability conditions for two regions of preload force. Figure 4-5 illustrates the force-displacement behavior described by Eq. (2.5) for the stable and bi-stable buckling actuators. The stable actuator, with PZTs OFF, demonstrates a zero slope at $\mathbf{y = 0}$ displacement while the over-preloaded actuator has positive slope at $\mathbf{y = 0}$. This leads to the bi-stable positions, $\mathbf{Y_{BISTABLE}}$, marked by the vertical black lines. Another effect of increasing $\mathbf{F_{PL}}$ is the increased actuator free displacement, $\mathbf{Y_{MAX}}$, and peak force over the stable actuator. Equations describing $\mathbf{Y_{BISTABLE}}$ and $\mathbf{Y_{MAX}}$ are listed in Eq. (4.2) and (4.3), respectively.

$$\begin{cases} F_{PL} \leq \frac{L}{2} k_{PCS} & stable \\ F_{PL} > \frac{L}{2} k_{PCS} & bi-stable \end{cases} \tag{4.1}$$

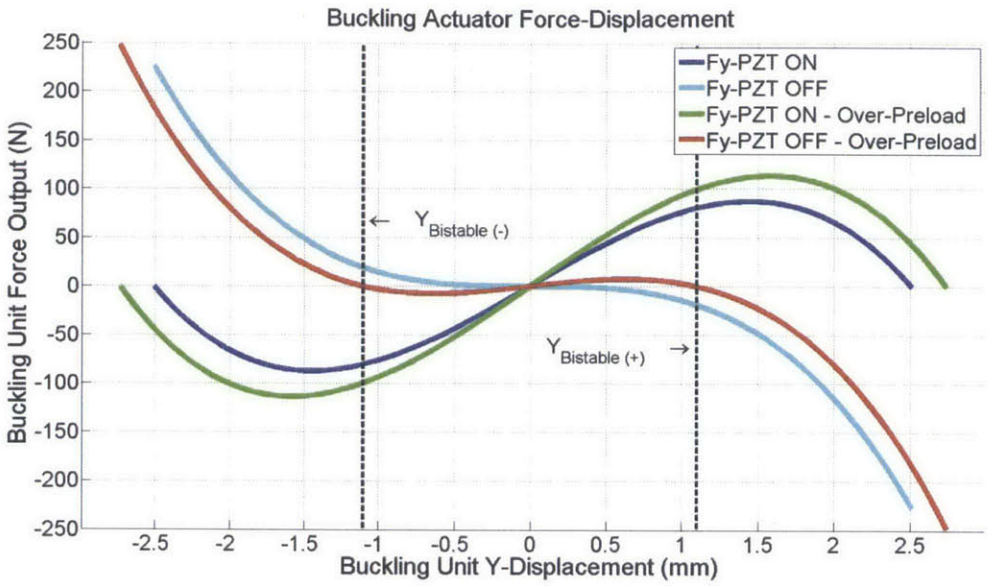

Figure 4-5: Force-displacement behavior of stable and over-preloaded buckling actuators

$$y_{BISTABLE} = \pm\sqrt{\left(2F_{PL}L - k_{PCS}L^2\right)\left(\frac{k_{SERIAL} + k_{PZT}}{k_{SERIAL} * k_{PZT}}\right)} \tag{4.2}$$

$$y_{MAX} = \pm\sqrt{\left(\frac{2F_B L}{k_{PZT}}\right) + \left(2F_{PL}L - k_{PCS}L^2\right)\left(\frac{k_{SERIAL} + k_{PZT}}{k_{SERIAL} * k_{PZT}}\right)} \tag{4.3}$$

4.5.2. Force Properties of the Switching Mechanism

Overview and Nomenclature

The energy storing function of the switching mechanism is described schematically in Figure 4-4. Here a groove in the cam-plate creates a hysteretic path for the cam-follower to trace as the buckling unit displaces along the y-direction. Figure 4-6 provides a closer view of one simple closed loop path, the latching gate, and a number of key positions that the cam-follower traverses.

Positions 1 & 4 correspond to the +/- $\mathbf{Y_{BISTABLE}}$ locations of the buckling actuator. When the cam-follower is at these locations the cam plate is centered about its lateral position, **x = 0**, and the cam-spring is at rest length. With the PZTs ON, the cam-follower will tend to move vertically away from the **x-axis**, constrained to move only along the **y-axis**, from **1→2** or from **4→5**. Positions 2 & 5 correspond to "latched" locations wherein the latching gate has opened, the cam-follower has reached the secondary slope, and the gate has closed. With the PZTs OFF, the cam-follower will tend to move towards the **x-axis**, again constrained along the **y-axis**, from **2→3** or from **5→6**. Cam-follower motion along these two slopes of the groove will store strain energy in the cam plate spring. Positions 3 & 6 are the "reset" positions. The cam-follower, passing the cusps on the inner contact surface, approaches the +/- $\mathbf{Y_{BISTABLE}}$ location. At the same location, the cam-plate experiences the maximum restoring force from the cam plate spring which tries to move it towards **x = 0**. From Figure 4-3 and Figure 4-5, the required energy to move the keystone across the "reset" stroke, represented by motion from **3→4** and **6→1**, is low in comparison with the actuator's available work output during the energy storage movement, **1→2→3** and **4→5→6**.

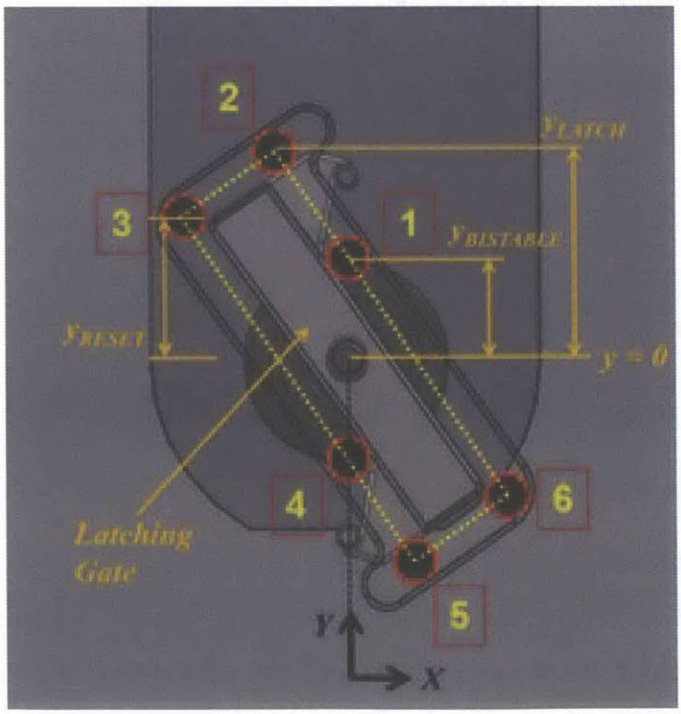

Figure 4-6: Close up of the cam-follower groove with key positions labeled.

The cam plate experiences a restoring force in the x-direction from the cam plate spring whenever it is displaced from the central, $\mathbf{x = 0}$, position. This force acts upon the buckling actuator cam-follower through the contact surfaces of the closed loop path. Using the instantaneous slope, this restoring force may be transformed, point by point, into the y-direction force component of the switching mechanism. As is shown in the next section, combining this *y*-direction force component with the buckling actuator force behavior fully describes the quasi-static performance of the coupled buckling actuator – switching mechanism device.

Force Behavior – Simplified Configuration

Derivation of the y-direction force component begins by defining the spring restoring force in the x-direction, $\mathbf{F_{Spring\text{-}x}}$, as a function of buckling unit displacement. As mentioned previously, the cam plate spring may have linear or non-linear stiffness depending on desired performance. For the simplified situation, a linear spring has been assumed with force behavior directly proportional to lateral cam plate movement as described in Eq. (4.4). Furthermore, the cam-groove path here has been chosen to have constant slope in each "region" where a region is defined as the portion of the cam-follower path between each set of points shown in Figure 4-6. The region-specific restoring force, $\mathbf{F_{Spring\text{-}x,\ n}}$, as a function of buckling unit displacement and the contact surface slope, is then defined by Eq. (4.5).

Due to symmetry in the selected cam-groove path, the force in region 1 (**1→2**) is equal and opposite to that of region 4 (**4→5**), force in region 2 (**2→3**) is equal and opposite to that of region 5 (**5→6**), and force in region 3 (**3→4**) is equal and opposite to that of region 6 (**6→1**). Figure 4-7 illustrates the force component breakdown of $\mathbf{F_{Spring\text{-}x,\ n}}$ acting on the cam-follower. The force, $\mathbf{F_{bal\text{-}Y,\ n}}$, represents the cam-plate spring force acting on the cam-follower in the direction of output stroke. By statically combining the output force of the buckling actuator, $\mathbf{F_Y}$, with $\mathbf{F_{bal\text{-}Y,\ n}}$, point by point along each region, the actuation and switching performance of the device can be determined.

$$F_{Spring-x}(\Delta x) = -K_{Spring}\Delta x \tag{4.4}$$

$$F_{Spring-x,n}(\Delta y) = -K_{Spring}\left.\frac{\Delta x}{\Delta y}\right|_n \Delta y \tag{4.5}$$

$$where\ \left.\frac{\Delta x}{\Delta y}\right|_n = slope^{-1},\ and \begin{cases} n=1;\ region\ 1 \\ n=2;\ region\ 2 \\ n=3;\ region\ 3 \end{cases}$$

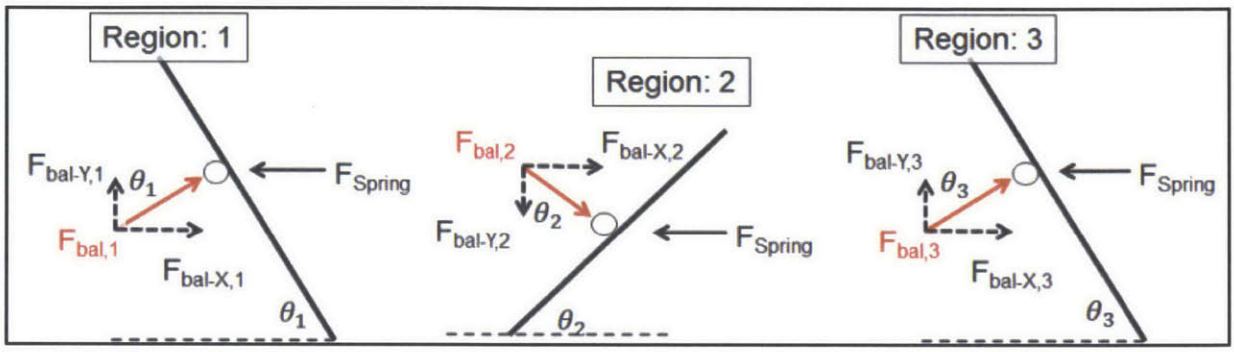

Figure 4-7: Force component breakdown by slope region.

Calculation of $\mathbf{F_{bal\text{-}Y,\ n}}$ at each slope region is described trigonometrically in Eq. (4.6) & (4.7) and through the set of piecewise equations, Eq. (4.8) – (4.10). As noted above, symmetry between regions 1 & 4, 2 & 5, and 3 & 6, indicate that the piecewise equations, Eq. (4.8) – (4.10) for regions 1, 2, and 3, respectively, are equally representative for regions 4, 5, and 6, only with opposite sign. Eq. (4.6) describes the static force balance and slope transformation, while Eq. (4.7) provides the simplified force equation including a term that represents the initial force condition at the start of the $\Delta\mathbf{y}$ displacement. Note that $\Delta\mathbf{y}$ represents relative displacement, not absolute displacement, as this must be used to deal with the piecewise nature of this specific closed loop path.

$$Since: \quad \frac{1}{\tan(\theta_n)} = \left.\frac{\Delta x}{\Delta y}\right|_n \qquad and statically: \quad F_{bal-x,n} = F_{Spring-x,n}$$

$$F_{bal-y,n} = F_{bal-x,n}\frac{\cos(\theta_n)}{\sin(\theta_n)} = \left(-K_{Spring}\left.\frac{\Delta x}{\Delta y}\right|_n \Delta y\right)\left(\frac{1}{\tan(\theta_n)}\right) \tag{4.6}$$

$$\textit{then}: \quad F_{bal-y,n} = -K_{Spring}\left(\left.\frac{\Delta x}{\Delta y}\right|_n\right)^2 \Delta y + C_n = -K_{Spring}\left(\frac{1}{\tan(\theta_n)}\right)^2 \Delta y + C_n \tag{4.7}$$

where C_n = *initial conditions* (*force*)

The force in region 1 is described by Eq. (4.8a-c), where (a) is the general form, (b) is the term representing initial force condition, and (c) is the complete form. The relative y-displacement occurs from $\mathbf{Y_{BISTABLE\,(+)}} \rightarrow \mathbf{Y_{LATCH}}$, (points **1→2**), as defined in Figure 4-6. Eq. (4.8b) indicates a zero-force initial condition which results from the cam-plate being at the central "rest" location when $\mathbf{Y=Y_{BISTABLE\,(+)}}$.

$$(a) \qquad F_{bal-y,1}(y) = -K_{Spring}\left(\left.\frac{\Delta x}{\Delta y}\right|_1\right)^2 \left(y - y_{BISTABLE(+)}\right) + C_1$$

$$(b) \qquad C_1 = F_{bal-y,1}\Big|_{y_{BISTABLE(+)}} = 0 \tag{4.8}$$

$$(c) \qquad F_{bal-y,1}(y) = -K_{Spring}\left(\left.\frac{\Delta x}{\Delta y}\right|_1\right)^2 \left(y - y_{BISTABLE(+)}\right)$$

The force in region 2 is described by Eq. (4.9a-c), where (a) is the general form, (b) is the term representing initial force condition, and (c) is the complete form. The relative y-displacement occurs from $\mathbf{Y_{LATCH}} \rightarrow \mathbf{Y_{RESET}}$, (points **2→3**), as defined in Figure 4-6. Eq. (4.9b) indicates that the initial force condition at $\mathbf{Y= Y_{LATCH}}$ for region 2 differs from the region 1 force at the same y-position by a negative valued, fraction of the cotangents of the slopes angles. This term accounts for the "instantaneous" slope change at the $\mathbf{Y_{LATCH}}$ position. Unless the slope angles match between regions 1 and 2, a force discontinuity will occur. Further, the negative sign is required to indicate the change in force direction, since the angles shown in Figure 4-7 are defined in opposite directions from the horizontal reference line.

$$(a) \qquad F_{bal-y,2}(y) = -K_{Spring}\left(\left.\frac{\Delta x}{\Delta y}\right|_2\right)^2 (y - y_{LATCH}) \; + \; C_2$$

$$(b) \qquad C_2 = F_{bal-y,2}\Big|_{y_{LATCH}} = -\frac{\cot(\theta_2)}{\cot(\theta_1)} F_{bal-y,1}\Big|_{y_{LATCH}}$$

$$(c) \qquad F_{bal-y,2}(y) = -K_{Spring}\left(\left.\frac{\Delta x}{\Delta y}\right|_2\right)^2 y + D \tag{4.9}$$

$$D = K_{Spring} y_{LATCH}\left[\frac{\cot(\theta_2)}{\cot(\theta_1)}\left(\left.\frac{\Delta x}{\Delta y}\right|_1\right)^2 + \left(\left.\frac{\Delta x}{\Delta y}\right|_2\right)^2\right] - K_{Spring}\frac{\cot(\theta_2)}{\cot(\theta_1)}\left(\left.\frac{\Delta x}{\Delta y}\right|_1\right)^2 y_{BISTABLE(+)}$$

The force in region 3 is described by Eq. (4.10a-c), where (a) is the general form, (b) is the term representing initial force condition, and (c) is the complete form. The relative y-displacement occurs from $\mathbf{Y_{RESET}} \rightarrow \mathbf{Y_{BISTABLE\,(-)}}$, (points **3→4**), as defined in Figure 4-6. Eq. (4.10b) again indicates a difference in initial force condition at $\mathbf{Y = Y_{RESET}}$ between regions 2 and 3.

$$(a) \qquad F_{bal-y,3}(y) = -K_{Spring}\left(\left.\frac{\Delta x}{\Delta y}\right|_3\right)^2 (y - y_{RESET}) \; + \; C_3$$

$$(b) \qquad C_3 = F_{bal-y,3}\Big|_{y_{RESET}} = -\frac{\cot(\theta_3)}{\cot(\theta_2)} F_{bal-y,2}\Big|_{y_{RESET}}$$

$$(c) \qquad F_{bal-y,3}(y) = -K_{Spring}\left(\left.\frac{\Delta x}{\Delta y}\right|_3\right)^2 y + E \tag{4.10}$$

$$E = K_{Spring} y_{RESET}\left[\frac{\cot(\theta_3)}{\cot(\theta_2)}\left(\left.\frac{\Delta x}{\Delta y}\right|_2\right)^2 + \left(\left.\frac{\Delta x}{\Delta y}\right|_3\right)^2\right]$$

$$- K_{Spring} y_{LATCH}\frac{\cot(\theta_3)}{\cot(\theta_2)}\left[\frac{\cot(\theta_2)}{\cot(\theta_1)}\left(\left.\frac{\Delta x}{\Delta y}\right|_1\right)^2 + \left(\left.\frac{\Delta x}{\Delta y}\right|_2\right)^2\right] + K_{Spring}\frac{\cot(\theta_3)}{\cot(\theta_1)}\left(\left.\frac{\Delta x}{\Delta y}\right|_1\right)^2 y_{BISTABLE(+)}$$

Discussion of Alternative Closed Loop Paths and Generalized Force Behavior

In the previous section, the slopes of the closed loop path are chosen to be constant for simplicity. Analysis of the relationship between lateral cam plate displacement and y-direction force acting on the cam-follower is also simplified by assuming a cam plate spring with linear stiffness. These two simplifications do not need to be used. More generalized forms of Eq. (4.4) and (4.5) are listed below as Eq. (4.11) and (4.12).

$$F_{Spring-x}(\partial x) = -K_{Spring}(g(x))\partial x \tag{4.11}$$

$$F_{Spring-x,n}(\partial y) = -K_{Spring}(g(x))\left.\frac{\partial x}{\partial y}\right|_n \partial y \tag{4.12}$$

$$where \left.\frac{\partial x}{\partial y}\right|_n = slope^{-1}, \; and \; \{n = \#\ of\ smooth,\ continuous\ slopes\}$$

The combined buckling unit – switching mechanism force behavior discussed in the next section clearly shows that constant cam-groove slopes and linear cam plate stiffness only apply linearly increasing or decreasing forces to the buckling actuator output. However, it is possible to select a cam-follower closed loop path which opposes the inherent non-linear force behavior of the buckling unit as a way to "shape" a more desirable force output. Another potential design choice is to utilize a non-linear spring such that the cam plate spring restoring force acting on the buckling unit output modifies the force behavior to make it more linear or to bias the available force towards the "outward" or "inward" stroke.

4.5.3. Combined Buckling Unit – Switching Mechanism Force Behavior

The analytical solutions for the buckling actuator force behavior, Eq. (2.5), and the switching mechanism force behavior, Eq. (4.8) – (4.10), may be combined point by point for the aggregate force behavior in each region of the closed loop cam-follower groove. The switching mechanism is passive and is fully described in each region by Eq. (4.8) – (4.10) and the y-position. The buckling actuator force behavior, however, is dependent on both the y-position and the energy state, "on" or "off", of the piezo-stack actuators. As described earlier, the buckling actuator

piezo-stacks are energized in region 1 & 4 and de-energized in all other regions. The piecewise combination of these forces by region is listed below in Eq. (4.13). The positive (+) or negative (-) sign refers to the y-direction of the contributing force.

$$
\begin{aligned}
&\text{Region 1}: (Y_{\text{BISTABLE (+)}} \rightarrow Y_{\text{LATCH (+)}}): && F_{y-region\ 1} = \Big((+)F_y(PZT\,ON)\Big) + \Big((-)F_{bal-y,1}(y)\Big) \\
&\text{Region 2}: (Y_{\text{LATCH (+)}} \rightarrow Y_{\text{RESET (+)}}): && F_{y-region\ 2} = \Big((-)F_y(PZT\,OFF)\Big) + \Big((+)F_{bal-y,2}(y)\Big) \\
&\text{Region 3}: (Y_{\text{RESET (+)}} \rightarrow Y_{\text{BISTABLE (-)}}): && F_{y-region\ 3} = \Big((-)F_y(PZT\,OFF)\Big) + \Big((-)F_{bal-y,3}(y)\Big) \\
&\text{Region 4}: (Y_{\text{BISTABLE (-)}} \rightarrow Y_{\text{LATCH (-)}}): && F_{y-region\ 4} = \Big((-)F_y(PZT\,ON)\Big) + \Big((+)F_{bal-y,4}(y)\Big) \\
&\text{Region 5}: (Y_{\text{LATCH (-)}} \rightarrow Y_{\text{RESET (-)}}): && F_{y-region\ 5} = \Big((+)F_y(PZT\,OFF)\Big) + \Big((-)F_{bal-y,5}(y)\Big) \\
&\text{Region 6}: (Y_{\text{RESET (-)}} \rightarrow Y_{\text{BISTABLE (+)}}): && F_{y-region\ 6} = \Big((+)F_y(PZT\,OFF)\Big) + \Big((+)F_{bal-y,6}(y)\Big)
\end{aligned}
\tag{4.13}
$$

Figure 4-8 illustrates the individual force-displacement behaviors of the buckling actuator and switching mechanism as functions of region. In this figure, the non-linear force characteristic of the buckling actuator is clearly visible. By close inspection, it is also apparent that the buckling actuator is over-preloaded because the $\mathbf{F_{Y\text{-}PZT\ OFF}}$ curve has positive slope at $\mathbf{y = 0}$. The solid green, red, and blue lines represent the force contribution of the switching mechanism at positive y-positions. The "dashed" green, red, and blue lines alternatively represent the switching mechanism force contribution for negative y-positions. Several vertical "dashed" and labeled lines in the figure indicate the y-positions for the bi-stable, latching, and resetting locations of the coupled device. Referring back to Eq. (4.9b) and (4.10b), the force discontinuities in the switching mechanism which result from the "instantaneous" change in slope at the latching and resetting locations are now apparent.

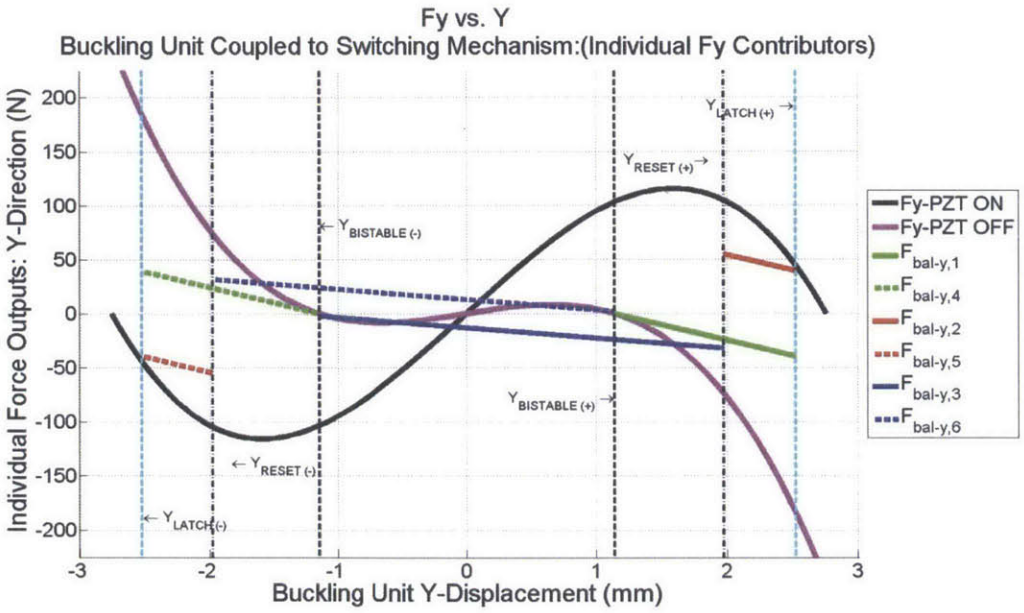

Figure 4-8: Force-displacement behavior of the individual force contributors. Forces from the switching mechanism are shown by region, 1-6, and the buckling actuator force is shown for the full actuator displacement range

The aggregate force-displacement behavior for the coupled device is demonstrated in Figure 4-9. The six individual curves each represent one of the six regions previously discussed. The solid and "dashed" green, red, and blue lines represent the combined force output for positive and negative y-displacements, respectively. Starting at the positive bi-stable position, when the PZTs are energized, the coupled device produces approximately its maximum positive output force as shown by the jump to the start of the green curve. Following the solid green curve, representing region 1, the y-displacement from this position to the latching point provides the available output force than can do work on a load. At the latching position, the PZTs are turned off and the force drops to the maximum negative value at the lower end of the solid red curve. This red curve, representing region 2, is the negative aggregate force pulling the keystone of the buckling actuator inwards towards the central "aligned" position.

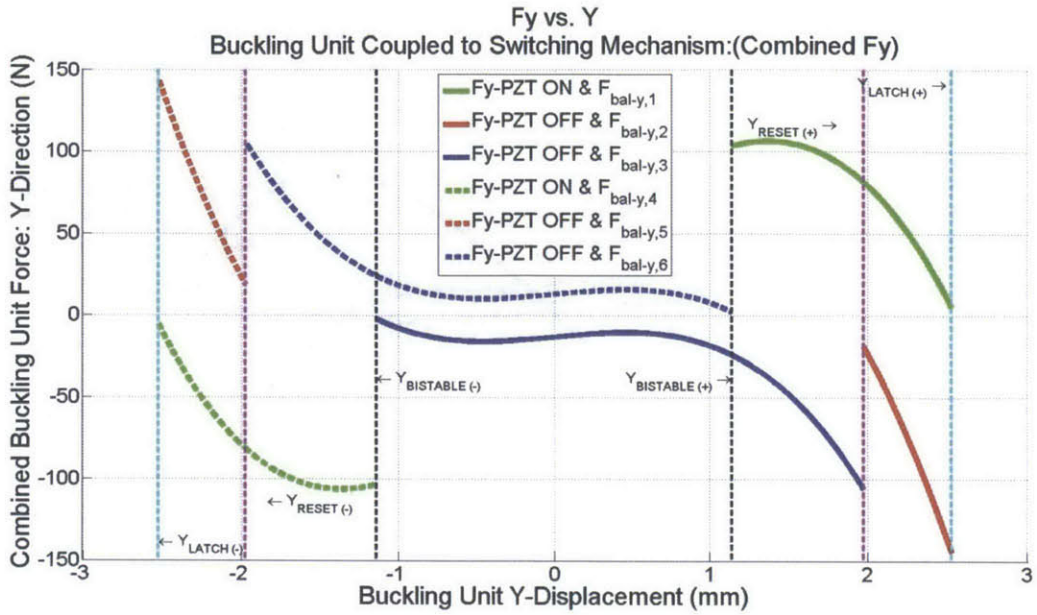

Figure 4-9: Aggregate force-displacement behavior of the combined buckling actuator – switching mechanism.

At the vertical magenta line marked "$\mathbf{Y_{RESET}}$", the cam-follower in the closed loop path passes over the cusp described in Figure 4-6. Also, as indicated in Eq. (4.13), this location marks the start of region 3 where the signs of the buckling actuator and switching mechanism forces are both negative. Whereas in regions 1 & 2, the two force components oppose each other, in region 3 they align in the same direction leading to the jump in force magnitude visible at $\mathbf{Y_{RESET}}$. This places the force-displacement behavior of the keystone at the lower end of the solid blue curve. This blue curve remains negative in magnitude from $\mathbf{Y_{RESET\,(+)}}$ over to $\mathbf{Y_{BISTABLE\,(-)}}$. Thus this blue curve represents the quasi-static force input used to move the over preloaded buckling actuator through the "reset" stroke. This solid blue curve reaches a force value of zero at the negative bi-stable position demonstrating that the energy stored in the cam plate spring during region 1 & 2 motion is fully released back into the buckling actuator during region 3 motion.

The preceding discussion covers the positive y-displacement portion of the coupled device's alternating output. From symmetry in the closed loop cam-follower path and in the governing equations, the force behavior of the three remaining regions, regions 4-6, are identical but opposite in magnitude to the preceding discussion.

4.6. Measured Performance

4.6.1. Prototype Implementation

A prototype has been implemented to verify the functionality and performance of the coupled buckling actuator – switching mechanism device. Figure 4-10 shows a CAD model and an image of the implemented prototype. In Fig. 4-10(a), label "A" encircles the buckling actuator contained within a large steel frame representing the "grounded" structure. Label "B" depicts the "load frame" which contains the measurement load cell and a loading screw. Label "C" encompasses the switching mechanism including: the cam plate and cam-follower groove, cam plate springs, and a latching gate. Finally, label "D" encircles a displacement amplification linkage implemented in this prototype to increase output stroke while reducing force. This linkage modification has been utilized to allow the switching mechanism components to be made by quick production but lower strength 3D printing methods. This is particularly useful for quick redesign and production of iterative cam plate and cam-follower path designs.

In the image of Fig. 4-10(b), three arrows are shown indicating the primary locations of motion. Label "E" references the actual output stroke of the buckling actuator which is amplified through the linkage resulting in a larger output stroke at label "F". Label "F" points directly to the location of the cam-follower and its engagement within the cam- follower groove. Label "G" then represents the "lateral" translational motion of the cam plate.

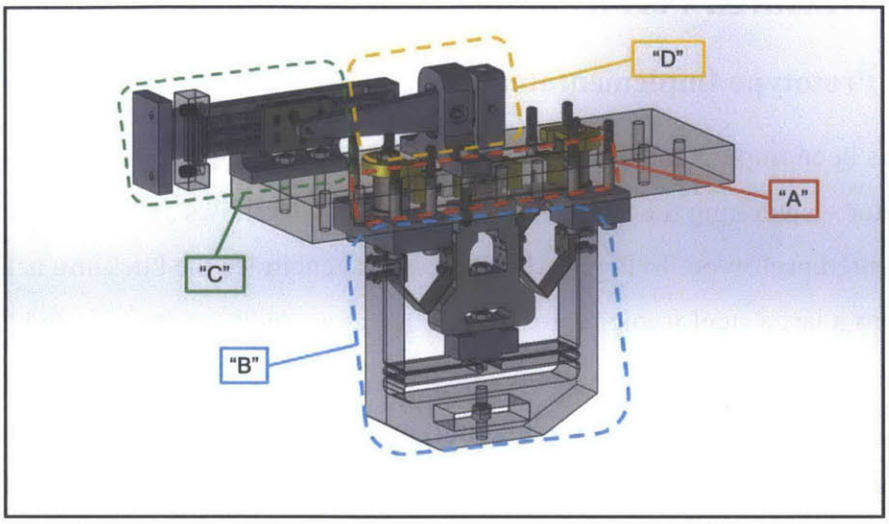

(a)

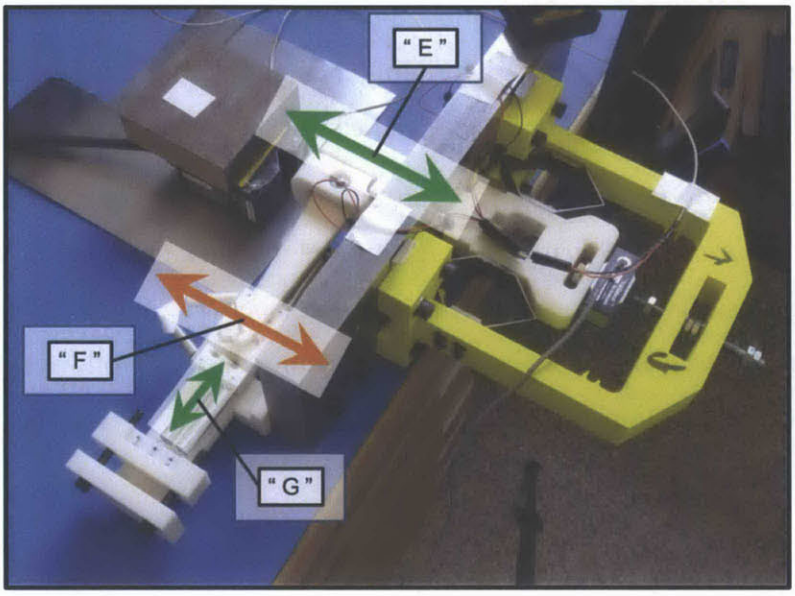

(b)

Figure 4-10: Bench top prototype of the buckling actuator – switching mechanism. (a) CAD model and (b) an image of the experimental prototype.

4.6.2. Performance

The bench top prototype has been subjected to several experiments to establish switching functionality and to compare its performance with the simulated force-displacement behavior described in the analysis section. In the two experiment types, functionality and performance, the PZTs in the buckling actuator are turned on and off at the $\mathbf{Y}_{\mathbf{BISTABLE}}$ and $\mathbf{Y}_{\mathbf{LATCH}}$ positions,

respectively. This is in accordance with the theory of operation described schematically in Figure 4-4, and represented in simulation in Figure 4-9. All experimental results are therefore with respect to this PZT activation sequence.

Figure 4-11 provides the most representative survey of the force-displacement performance and functionality of the device. In this figure, the simulated force-displacement behavior in all six regions is shown by the green, red and blue curves while the experimentally measured results are represented in the black curve. Vertical dashed lines represent the y-positions of PZT activation/deactivation, $\mathbf{Y_{BISTABLE}}$ and $\mathbf{Y_{LATCH}}$, as well as the "reset" positions. From the figure, it is clear that the prototype under-performs in regions 1 & 4 (green curves), closely follows simulation values in regions 2 & 5 (red curves), and then again under-performs in regions 3 & 6 (blue curves). Level of performance is biased towards the (-) y-displacement regime where region 4 measurement data is closer to the simulated value than the measured data in region 1. This bias is less prevalent in the rest of the figure.

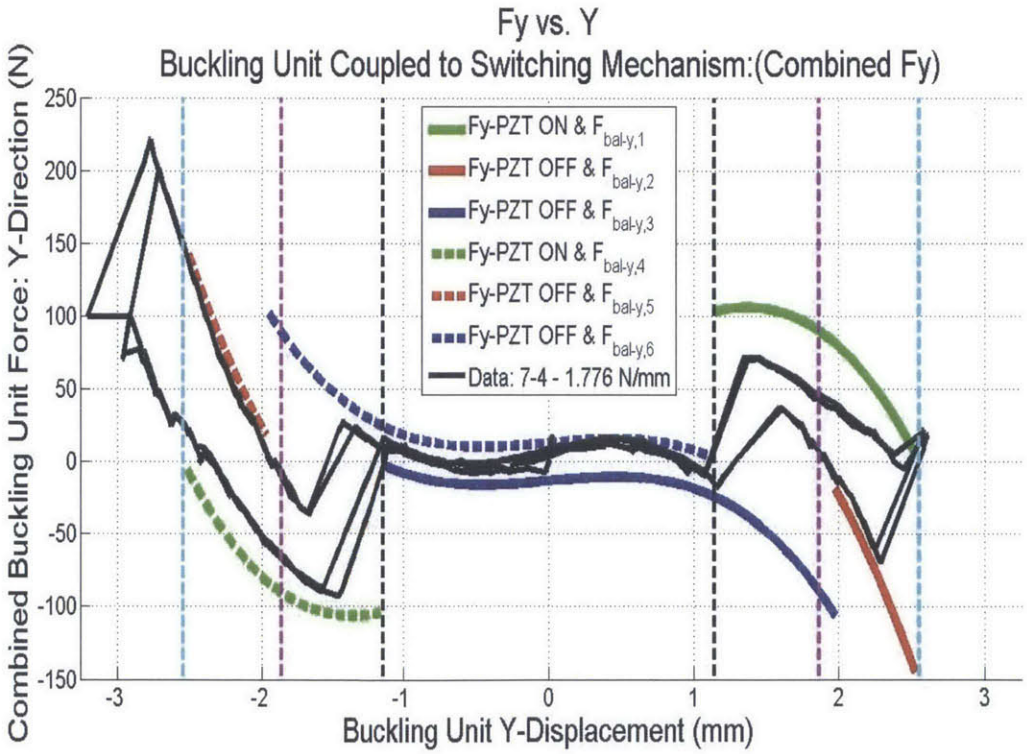

Figure 4-11: Measured force-displacement performance of the buckling actuator engaged with the switching mechanism and cycled through bipolar stroke as compared to simulation values. Vertical dashed lines represent positions: $Y_{BISTABLE}$ (black), Y_{LATCH} (cyan), & Y_{RESET} (magenta).

At six locations in Figure 4-11, corresponding to the $Y_{BISTABLE}$, Y_{LATCH}, and Y_{RESET} positions, the measured data displays a linear force-displacement slope. These are the locations where the PZT activation/deactivation has been performed during the experiment. Analytically, these locations should correspond to discontinuous changes in the force with zero displacement however the compliance of the load frame allows some unwanted displacement. Implementation of a stiffer load frame and any other components along the load path would diminish this effect and align the results more closely with the simulation.

Referring to Figure 4-11, switching functionality of the device in this experiment would not be achieved since the measured data crosses the zero-force line between regions 2 & 3, and regions 5 & 6. However in practice, and in video taken of the experiments, switching does in fact occur. This discrepancy results due to the compliance in the load frame. As the cam-follower approaches the Y_{RESET} position, where the change in slope should discontinuously increase the load, the load frame deflects to a point where the buckling actuator output reaches zero force prior to the cam-follower reaching the reset position. Although a force jump occurs immediately after this zero-force "crossing", the force behavior which has been simulated may be achieved through improved load frame stiffness.

The under-performance in regions 1 & 4 and 3 & 6 is attributable to under-performance of the buckling actuator itself. This is visible in Figure 4-12 where the measured data (red curve) represents the force output of the buckling unit disengaged from the switching mechanism. Here too, the region 1 & 4 performance does not match the simulation. The performance bias towards (-) y-displacement is also visible. Thus, the underperforming coupled device is fundamentally hindered by the low performance in the buckling actuator.

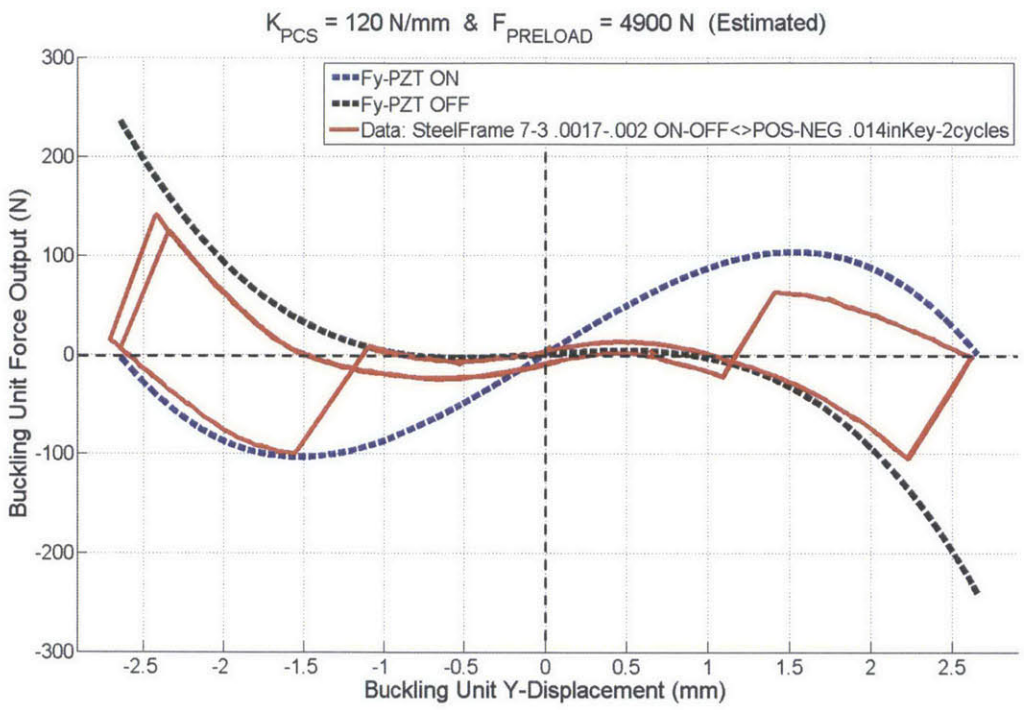

Figure 4-12: Measured force -displacement performance of the standalone buckling actuator compared to simulation values. The measured performance (red curve) contains discontinuities at the PZT energizing/de-energizing positions.

Chapter 5

5. Dual Unit Buckling Actuator

5.1. Design Background

The importance of having bidirectional control authority in a piezoelectric buckling actuator was discussed in Chapter 4. The solutions presented in the preceding chapter and in the literature [11] for achieving controllable, quasi-static, bidirectional motion from an otherwise non-deterministic standalone buckling actuator are viable yet their performance may be improved through other methods. One such method is to place two buckling actuators in parallel and couple their output nodes together with a spatial difference in the output positions of each node relative to their local reference frames as described in [13].

A schematic of this type of dual unit buckling actuator in its de-energized state is shown in Figure 5-1. Referencing figures from preceding chapters, it is clear in this figure that the dual unit actuator is simply the aggregation of two individual piezoelectric buckling actuators connected to the same "ground" reference at their "side blocks", and connected to each other at their output keystones through a rigid coupler. The figure indicates that the preload compensation springs are present and that each buckling actuator in this configuration has an initial displacement relative to its central aligned position, defined by the constant initial angle, Θ. The initial displacements of each buckling actuator are in opposite directions leading to the relative spatial difference of each keystone in its local reference frame.

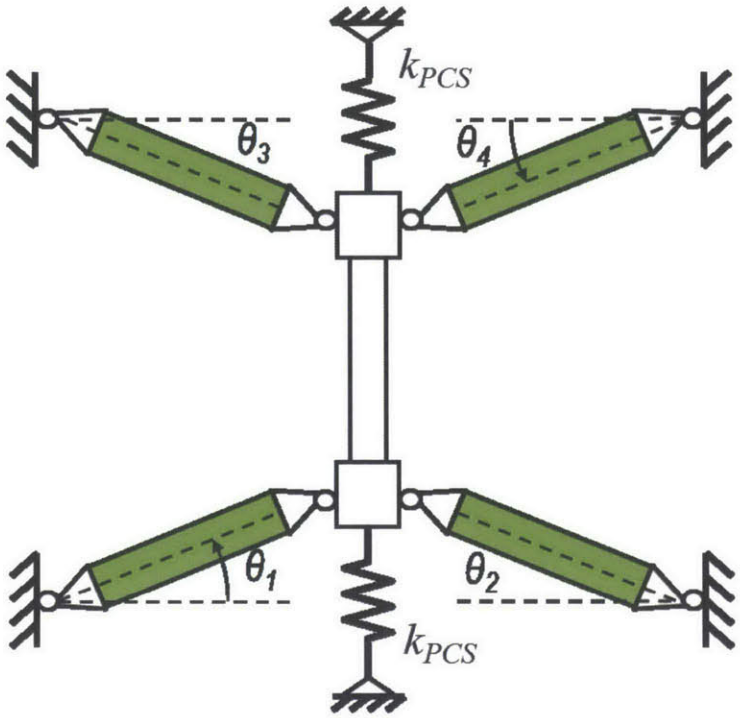

Figure 5-1: Schematic of the Dual Unit Buckling Actuator layout.

5.2. Theory of Operation

In a standalone buckling actuator, two PZTs drive the motion and force characteristics whereas in the dual unit actuator four PZTs are now present. It is assumed throughout this thesis that the PZTs for an individual buckling actuator are energized or de-energized synchronously. In a single unit device this leads to two activation states: 1) both units off or 2) both units on. In the dual unit actuator, the PZTs for an individual buckling actuator are still activated synchronously, but the activation of one actuator with respect to the other may be synchronous or asynchronous. This leads to four possible activation states in the dual unit actuator: 1) both units on, 2) "upper" unit on, "lower" unit off, 3) both units off, and 4) upper unit off, lower unit on. Due to the constant offset in the keystone positions with respect to their local reference frames, asynchronous activation has the effect of biasing the common output force in one direction or the other. This means that the dual unit device can be "steered" effectively to positive or negative y-displacement. Figure 5-2 and Figure 5-3 demonstrate the four activation states of the dual unit actuator and the five resulting static equilibrium configurations: $\mathbf{Y = 0}$, $\mathbf{Y = +/- Y_{EQUIL\text{-}MID}}$, and $\mathbf{Y = +/- Y_{EQUIL\text{-}OUTER}}$.

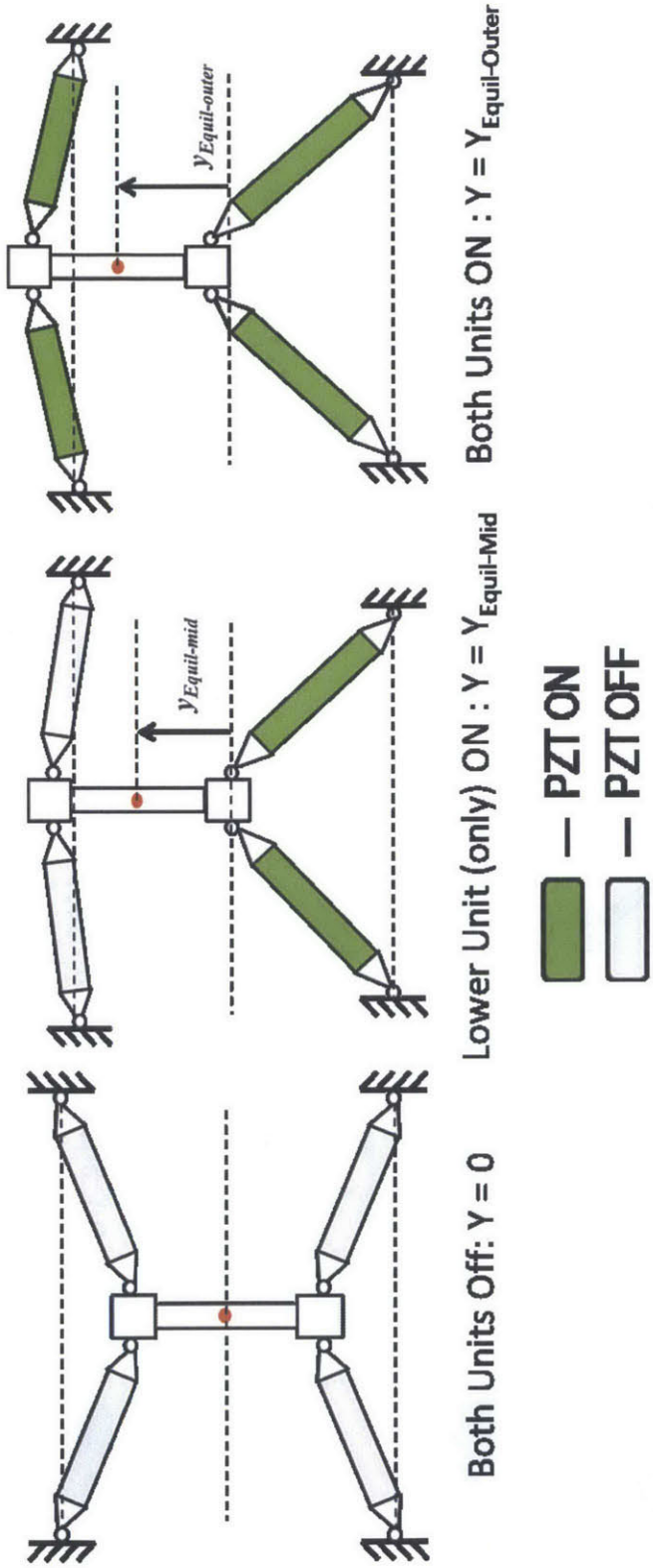

Figure 5-2: Schematic depicting the displacement motion of the dual unit buckling actuator and the basic equilibrium positions.

Figure 5-3: Activation states, corresponding equilibrium configurations, and the color code for the static force properties.

An important observation in Figure 5-2 and Figure 5-3 is in the activation states where only one unit is on. During these states, defined as state (2) and state (4), the energized buckling actuator has sufficient force and displacement output to push the de-energized buckling actuator through its kinematic singularity represented by the dashed line. At this point, both buckling actuators of the dual unit are on the same side of their respective kinematic singularities and energizing the buckling actuator that is currently "off" to reach activation state (1) will continue force and displacement output in that direction.

Understanding this part of the operating principle then leads to the following requirements: 1) there must exist some offset between the keystone's separation distance and the distance between the fixed side blocks of the individual actuators and 2) there is a maximum offset in these relative distances, beyond which the activations of one buckling actuator will not be sufficient to push the other unit through its kinematic singularity. In other words, the constant initial angle θ defined in Figure 5-1 may not be equal to zero, and has an upper limit before some of the motions in Figure 5-3 are no longer achievable.

5.3. Static Force Properties

As described above, the dual unit actuator is an aggregation of two individual buckling actuators operating in parallel with a common output, but with a relative offset between the individual keystone positions in their own reference frames. This allows the static force property of the dual unit actuator to be calculated by simply adding together the individual force contributions of each actuator. Referring to the discussion in Chapter 2, the static force property of an individual buckling actuator is defined by Eq. (2.5) which is reproduced here, for convenience, as Eq. (5.1). Note that in Eq. (5.1), the displacement position, **y**, is referenced to the central aligned position of the individual actuator. This means that at the initial resting configuration shown in Figure 5-1, the y-position for the lower unit will be positive in its local reference frame, while the y-position for the upper unit will be negative. The magnitude of these values will depend on the initial rest angle Θ, and the characteristic length, **L**, described in Chapter 2. For the basic derivation of static force properties, the following assumptions have been made:

- $\boldsymbol{\Theta_1 = \Theta_2 = \Theta_3 = \Theta_4 = \Theta}$
- $\boldsymbol{F_{B\text{-}1} = F_{B\text{-}2} = F_{B\text{-}12}}$ **&** $\boldsymbol{F_{B\text{-}3} = F_{B\text{-}4} = F_{B\text{-}34}}$

- $\mathbf{k_{PCS-1} = k_{PCS-2} = k_{PCS}}$
- $\mathbf{F_{PL-12} = F_{PL-34} = F_{PL}}$

$$F_y = 2\left(F_B\left(\frac{k_{Serial}}{k_{Serial} + k_{PZT}} \right) + F_{PL} - \left(\frac{k_{Serial} * k_{PZT}}{k_{Serial} + k_{PZT}} \right) \frac{y^2}{2L} \right) \frac{y}{L} - k_{PCS} y \tag{5.1}$$

The aggregate force of the dual unit actuator is then described generally by Eq. (5.2). At this point it is convenient to apply a single and common output position reference as is shown in Figure 5-4 at the coupler connecting the keystones of the two units.

$$\begin{aligned} F_{y,dual} &= f(y, \theta, L, k_{SERIAL}, k_{PZT}, F_B, F_{PL}, k_{PCS}) \\ &= \sum_{n=1}^{2} F_{y,dual,n} \end{aligned} \tag{5.2}$$

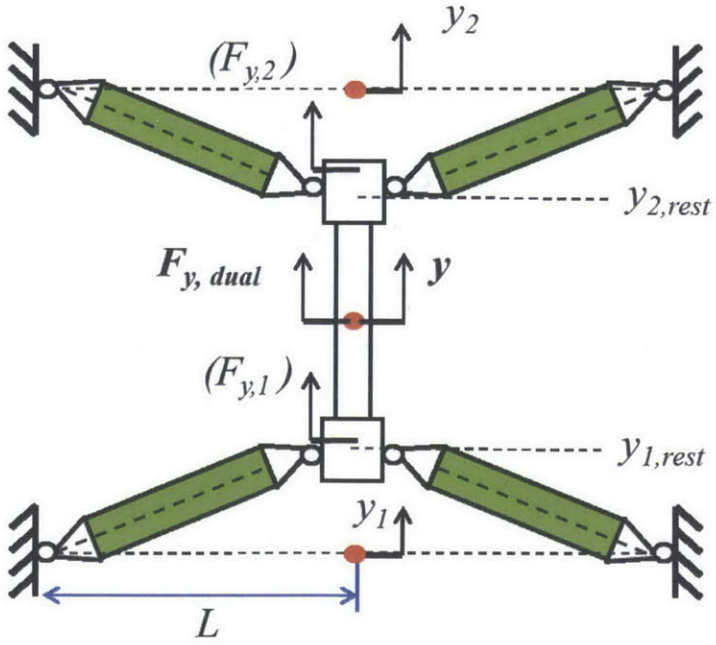

Figure 5-4: Definition of the individual and common displacement references for the Dual Unit Buckling Actuator.

In this figure, the previous discussion of the keystone positions relative to their own reference frames is clarified. At rest, the lower keystone sits at position, $\mathbf{y}_{1,\,\mathbf{REST}}$ and the upper keystone sits at $\mathbf{y}_{2,\,\mathbf{REST}}$. From Figure 5-1 and Figure 5-4 the value of these initial offsets is described by Eq. (5.3). The offsets in Eq. (5.3) can be combined with the common displacement reference, **y**, shown in Figure 5-4 to yield the displacement position of each actuator in its local reference frame as a function of the common displacement reference, Eq. (5.4).

$$\begin{aligned} y_{1,rest} &= L\tan(\theta_1) \\ y_{2,rest} &= L\tan(\theta_3) \end{aligned} \tag{5.3}$$

$$\begin{aligned} y_1 &= y + y_{1,rest} = y + L\tan(\theta) \\ y_2 &= y - y_{2,rest} = y - L\tan(\theta) \end{aligned} \tag{5.4}$$

Now the aggregate force property of the dual unit actuator can be represented using the common position reference instead of individual, local displacement positions. This is shown in Eq. (5.5). Using the relationship of Eq. (5.6) and combining it into Eq. (5.5), the final reduced form of the static force property is shown in Eq. (5.7).

$$\begin{aligned} &F_{y,dual} = \\ &2\left(F_{B12}\left(\frac{k_{Serial}}{k_{Serial}+k_{PZT}}\right)+F_{PL}-\left(\frac{k_{Serial}*k_{PZT}}{k_{Serial}+k_{PZT}}\right)\frac{(y+L\tan(\theta))^2}{2L}\right)\frac{(y+L\tan(\theta))}{L} \\ &-k_{PCS}(y+L\tan(\theta)) \\ &+ \\ &2\left(F_{B34}\left(\frac{k_{Serial}}{k_{Serial}+k_{PZT}}\right)+F_{PL}-\left(\frac{k_{Serial}*k_{PZT}}{k_{Serial}+k_{PZT}}\right)\frac{(y-L\tan(\theta))^2}{2L}\right)\frac{(y-L\tan(\theta))}{L} \\ &-k_{PCS}(y-L\tan(\theta)) \end{aligned} \tag{5.5}$$

$$[y+L\tan(\theta)]^3+[y-L\tan(\theta)]^3 = 2y^3+6L^2y\tan^2(\theta) \tag{5.6}$$

$$F_{y,dual} =$$

$$-2\frac{K_1}{L^2}y^3 + \left[4\frac{F_{PL}}{L} - 2k_{PCS} - 6K_1\tan^2(\theta) + 2\frac{K_2}{L}\left(F_{B12} + F_{B34}\right)\right]y$$

$$+ 2K_2\tan(\theta)\left[F_{B12} - F_{B34}\right] \tag{5.7}$$

$$where\ K_1 = \left(\frac{k_{Serial} * k_{PZT}}{k_{Serial} + k_{PZT}}\right) \quad \& \quad K_2 = \left(\frac{k_{Serial}}{k_{Serial} + k_{PZT}}\right)$$

Plotting Eq. (5.7) over a range of y-displacement values, the static force property for each of the four activation states is shown in Figure 5-5. Also shown in this figure are the labels indicating which force curves lead to the five static equilibrium positions. As is noted, the static force in this plot assumes that the preload and PZT-ON forces are set at 5250 N, the PCS stiffness is 120 N/mm, and there is an initial rest angle $\theta = 0.85$ degrees.

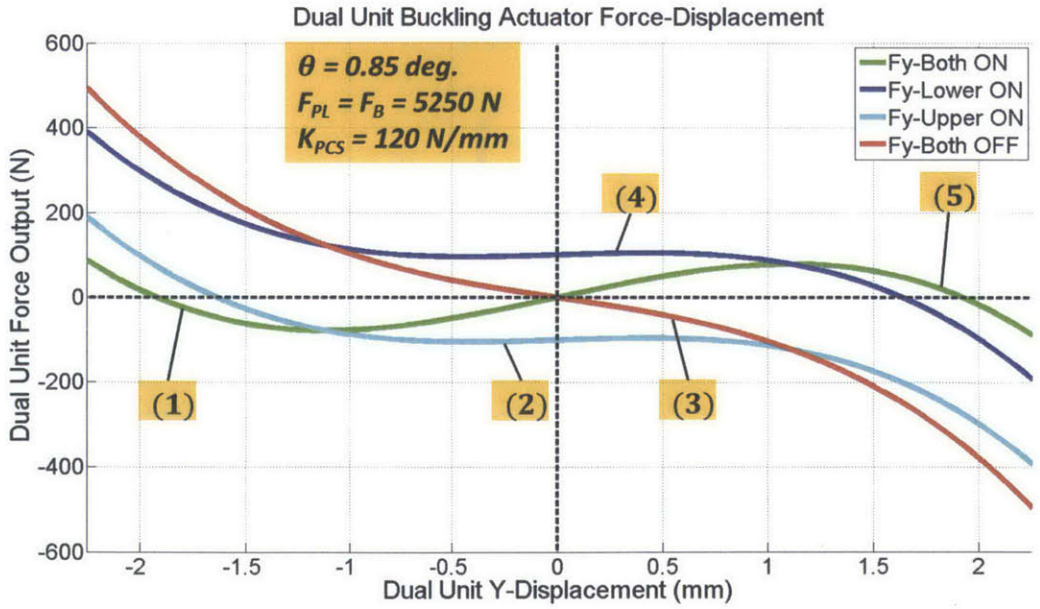

Figure 5-5: Static force property of the dual unit buckling actuator across the four activation states.

An inspection of the static force plot reveals some interesting behavior. Perhaps the most useful is the near linear and constant output force during activation states (2) and (4) represented in the light and dark blue curves. Between approximately 1.6 mm and the (-) maximum displacement, the dark blue curve of activation state (4) remains in the positive force regime, and vice versa for the light blue curve. The significance of this behavior is prominent in the discussion of dynamic switching in the next section. The red curve indicating that both actuators are off and the green curve indicating that both actuators are on generally follow the force displacement behavior of the standalone buckling actuator discussed in Chapter 2. The buckling actuator properties in Figure 5-5 are identical to those in the Chapter 2 discussion, Figure 2-5. Due to the enforced rest position displacements, the state (3) restoring force (red curve) maintains a negative slope near zero displacement, and the state (1) output displacement drops from approximately +/- 2.5mm in Figure 2-5, down to roughly +/- 2.0 mm in Figure 5-5.

5.4. Dynamic Modeling

The dual unit actuator has well behaved and useful static force properties, but not all operating conditions of piezo-actuators are static or quasi-static. In fact, many piezo-actuators are used in applications that require the output load to be moved or acted upon at high frequencies. Some specific applications include: active vibration damping, oscillating optical lenses and mirrors, and high frequency driven acoustic instruments. Creating a dynamic system model and gaining an understanding of appropriate switch timing is crucial for effective dynamic control. In particular, understanding how the system parameters affect speed of response and overshoot is important for designing dual unit actuators for specific applications.

5.4.1. System Model

For dynamic analysis, the dual unit actuator may be modelled as a second order mass-spring-damper system with a nonlinear force input as defined in the previous section. The total system mass should be obtained by summing the mass of the driven load and the equivalent mass of the moving components in the actuator. The "spring" of the system model is already included in the nonlinear force properties derived above, and the damping is best estimated through experimental measurements. The dual unit actuator being analyzed in this section is built up

from two flexure free buckling actuators. It is expected that the damping coefficient will be relatively small, but that energy dissipation will also occur as a result of friction. For the following equations of motion, a coulomb friction model is implemented which results in energy dissipation independent of actuator velocity and therefore of driving frequency. The magnitude of the coulomb friction may be difficult to determine analytically, so it is best deduced experimentally. Figure 5-6 shows the corresponding schematic of the second order dynamic system for the dual unit actuator. The general form of the equation of motion is listed in Eq. (5.8).

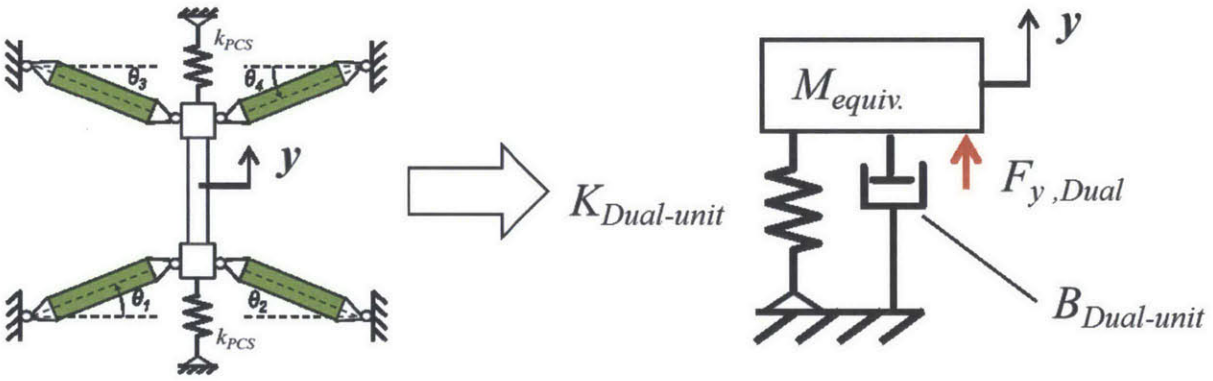

Figure 5-6: Conversion of the dual unit actuator schematic to a nonlinear second order dynamic system.

$$
\begin{aligned}
&m\ddot{y} = F_{y,dual} - B\dot{y} - Csign(\dot{y}) \\
&where: \\
&F_{y,dual} = f\left(y, y^3\right) \\
&m = Mass_{Equiv.} + Mass_{Load}\ (kg) \\
&B = damping\ coefficient\left(\frac{N-\sec}{m}\right) \\
&C = Friction\ constant\ force\ (N)
\end{aligned}
\tag{5.8}
$$

Since the dual unit actuator has a nonlinear force property with respect to output position, the general solutions for second order linear systems are not applicable. As a result, determining the system overshoot, natural frequency, rise time, and other dynamic performance characteristic is not trivial. A closed form analytical solution may in fact not exist. To deal with the nonlinear

system dynamics, numerical integration will need to be employed. Additionally, some general intuition into the system's response may be observed using phase plane analysis. In the following sections, phase plane trajectories are used to determine optimal timing for activation state switching sequences.

5.4.2. Phase Plane Analysis

In phase plane analysis, two states of a state determined system are plotted on a plane to observe the behavior of one state with respect to the other as time varies. With a set of initial conditions which do not represent a static equilibrium, the values of the two states will change as a function of time and create a curve or "trajectory" [15]. These trajectories provide information as to the nature of the nonlinear system.

For equations of motion of second order systems, it is particularly useful to plot trajectories corresponding to states of position and velocity. To do this for the dual unit actuator, first plug Eq. (5.7) into the general equation of motion of Eq. (5.8). Then place Eq. (5.8) into a state determined form as is shown in Eq. (5.9). Note that the variables PP, QQ, RR, SS, and CC have been substituted into the nonlinear force property of Eq. (5.7) as well as into the damping and coulomb friction terms to make the state determined form more readable.

$$\frac{d}{dt}\begin{Bmatrix} y \\ \dot{y} \end{Bmatrix} = \begin{bmatrix} 0 & 1 \\ \left(PPy^2 + QQ\right) & SS \end{bmatrix}\begin{Bmatrix} y \\ \dot{y} \end{Bmatrix} + \begin{bmatrix} 0 \\ \left(RR + CCsign(\dot{y})\right) \end{bmatrix}$$

where:

$$PP = -2\frac{K_1}{L^2 m}$$

$$QQ = \left[4\frac{F_{PL}}{Lm} - \frac{2k_{PCS}}{m} - \frac{6K_1}{m}\tan^2(\theta) + 2\frac{K_2}{Lm}\left(F_{B12} + F_{B34}\right)\right] \tag{5.9}$$

$$RR = 2\frac{K_2}{m}\tan(\theta)\left(F_{B12} - F_{B34}\right)$$

$$SS = -\frac{B}{m}$$

$$CC = -\frac{C}{m}$$

Although a closed form solution for the two first-order differential equations in Eq. (5.9) does not exist, numerical integration and a pair of initial conditions may be used to extract the position and velocity states. The most simple numerical integration method to use here would be the Euler method based on forward finite differences [16]. For these set of states, the Euler method would be solved is as shown in Eq. (5.10).

$$\dot{y}(t_{i+1}) = \left[PP * y(t_i)^3 + QQ * y(t_i) + RR + SS * \dot{y}(t_i) + CC * sign(\dot{y}(t_i)) \right] \Delta t + \dot{y}(t_i)$$

$$y(t_{i+1}) = \left[\dot{y}(t_i) \right] \Delta t + y(t_i) \tag{5.10}$$

and

$$\Delta t = t_{i+1} - t_i$$

In the velocity-position phase plane plots of the next section, both the Euler and more advanced Runga-Kutta methods have been used. A MATLAB script and function using the above numerical integration to tabulate the position and velocity states from a pair of initial conditions is listed in APPENDIX A.

An example of the phase plane trajectories for the dual unit actuator is shown in Figure 5-7 where an activation state (4) has been set, and a number of initial conditions defined. In this figure, each blue curve represents a trajectory beginning along the x-axis, where the initial conditions are defined as having zero velocity and some position value. The blue arrows indicate that in quadrants I and II of the phase plane the velocity state is positive and as time progresses the point corresponding to the current velocity and position state will progress clockwise along the trajectory. This implies that all trajectories begin at their most counter clockwise position which is this phase portrait belongs entirely to the x-axis, i.e. zero velocity. At the most clockwise position of the trajectories in this phase portrait, the trajectories spiral around a "final" position exhibiting positive and negative velocities and an oscillating position. These "spiral" conditions in a phase plot indicate that a given system is underdamped.

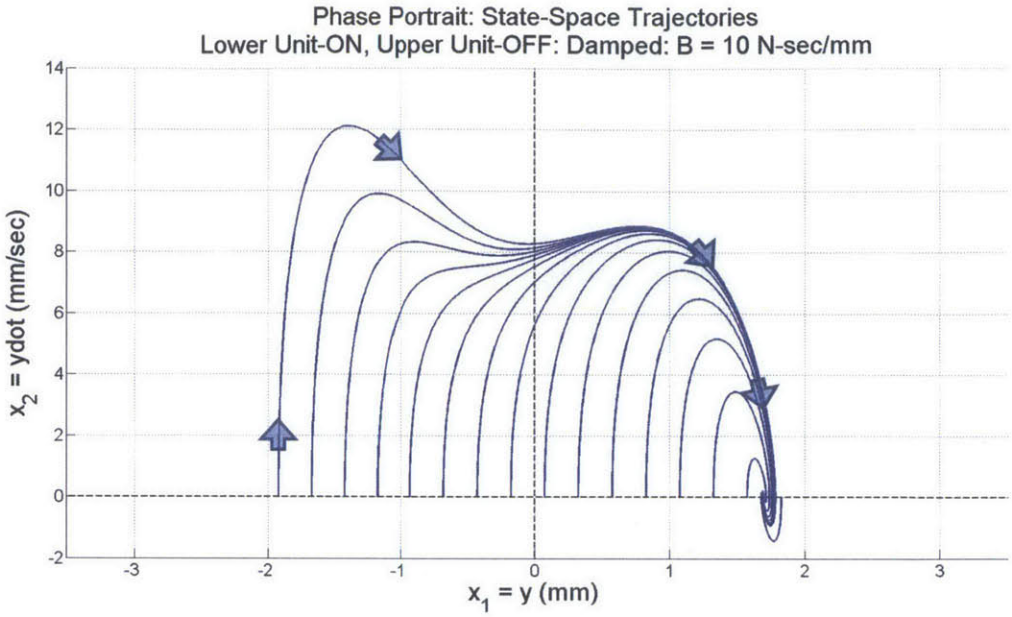

Figure 5-7: Set of trajectories for the dual unit actuator on the velocity-position phase plane.

5.4.3. Switching Sequences

Now that the nonlinear dynamic model has been derived and the technique for solving it explained, the dual unit actuator's behavior during "switching" may be studied. Switching refers to the actuator's position change from one equilibrium point, as defined in Figure 5-2 and Figure 5-3, to another equilibrium point. It is assumed that in any application where the dual unit actuator is used as the main actuating device, the desired movement will be between equilibrium points. Since the dual unit actuator has five equilibrium points, there exists a large number of switching sequences that could be studied. The full list of position switching sequences is tabulated in Table 5-1. From this list, the position switch that is most likely to be exploited in a real application is the movement from the $-Y_{EQUIL\text{-}OUTER}$ to $+Y_{EQUIL\text{-}OUTER}$ position. This position switch is indicated in the top row of Table 5-1. Table 5-2 lists all of the potential equilibrium configurations, and thus activation state sequences, to go from the negative outer equilibrium point to the positive outer equilibrium point.

From	To	Category	Notes
(1) $-Y_{Equil.-outer}$	$+Y_{Equil.-outer}$	Outer – outer	Also (+) → (-)
$-Y_{Equil.-outer}$	$+Y_{Equil.-mid}$	Outer – opp. middle	Also (+) → (-)
$+Y_{Equil.-outer}$	Y_0	Outer – center	Also (-) → (0)
$+Y_{Equil.-outer}$	$+Y_{Equil.-mid}$	Outer – middle	Also (-) → (-)
Y_0	$+Y_{Equil.-outer}$	Center – outer	Also (0) → (-)
Y_0	$+Y_{Equil.-mid}$	Center - middle	Also (0) → (-)
$+Y_{Equil.-mid}$	$+Y_{Equil.-outer}$	Middle – outer	Also (-) → (-)
$+Y_{Equil.-mid}$	Y_0	Middle – center	Also (-) → (0)
$-Y_{Equil.-mid}$	$+Y_{Equil.-mid}$	Middle – middle	Also (+) → (-)
$-Y_{Equil.-mid}$	$+Y_{Equil.-outer}$	Middle - opp. outer	Also (+) → (-)

Table 5-1: The complete list of potential switching sequences between equilibrium points of the dual unit buckling actuator.

Consider switching from Config. (1) → Config. (5)

Sequence	Quasi-static (Y/N)	Dynamic (Y/N)	Notes
2 – Trajectories			
1 → 2 → 5	No	No	Requires an initial condition beyond equilibrium point
1 → 3 → 5	(2) No	Yes	Dependent on mass (m), damping (B), friction (C) parameters
1 → 4 → 5	Yes	Yes	
3-Trajectories			
1 → 2 → 3 → 5	No	Yes	Dependent on m, B, C parameters (optimal switching: 1→3→5)
1 → 2 → 4 → 5	Yes	Yes	Optimal switching will default to: 1→4→5
1 → 3 → 4 → 5	(1) Yes	Yes	Minimum transition time
4 – Trajectories			
1 → 2 → 3 → 4 → 5	Yes	Yes	Not Analyzed (optimal switch.: 1→3→4→5)

Table 5-2: The complete list of potential activation sequences to switch between one outer equilibrium point and the other.

From Table 5-2, two switching sequences are highlighted, the **1→3→4→5** sequence and the **1→3→5** sequence. The **1→3→5** switching sequence does not provide a quasi-static position switch from $-\mathbf{Y}_{\mathbf{EQUIL\text{-}OUTER}}$ to $+\mathbf{Y}_{\mathbf{EQUIL\text{-}OUTER}}$. Switching using this sequence can only be performed dynamically. In contrast, the **1→3→4→5** sequence has a dynamic aspect to it, but if there is a timing issue, the sequence can always be completed quasi-statically.

5.4.1. Optimal Switching

The following phase plane trajectories describe the **1→3→4→5** sequence and introduce a switch position control law which guarantees the minimum transition time between (–) $\mathbf{Y}_{\mathbf{EQUIL\text{-}OUTER}}$ to (+) $\mathbf{Y}_{\mathbf{EQUIL\text{-}OUTER}}$ using this sequence. The control law is generalized, will function for any switching sequence, and provides the minimum transition time. However, it should be noted that for underdamped systems, the "spiraling" effect at the end of phase plane trajectories, which represents system oscillation, must be dealt with separately.

Figure 5-8 shows the first full trajectory corresponding to the **1→3→4→5** sequence. The color of the curve matches the force color code defined previously in Figure 5-3. At the start of the switching sequence, it is assumed that the dual unit actuator is at rest and at the negative outer equilibrium position also known as equilibrium/activation state (1). This leads to initial conditions shown in Figure 5-8. The dual unit actuator is then switched to the activation state (3). If no other switching occurs, the full trajectory will come to an end with zero velocity and a near zero position. By close inspection, it can be seen that the trajectory in this plot overshoots $Y = 0$ and due to the modelled coulomb friction, the actuator output reaches an equilibrium position slightly above the zero position.

In Figure 5-9, a family of blue curves is shown which represent the next activation state, state (4), of the switching sequence. By definition, any secondary trajectory will have initial conditions belonging to some location along the primary trajectory. This figure represents a subset of the infinite trajectories that could be drawn off of the primary trajectory. Note that all of the blue trajectories terminate at the $+\mathbf{Y}_{\mathbf{EQUIL\text{-}MID}}$ position. From the static force behavior in Figure 5-5, the dual unit actuator has only one equilibrium position during this activation state. As a result, all state (4) trajectories will approach this equilibrium position unless an offset coulomb friction force causes the actuator output to stop short.

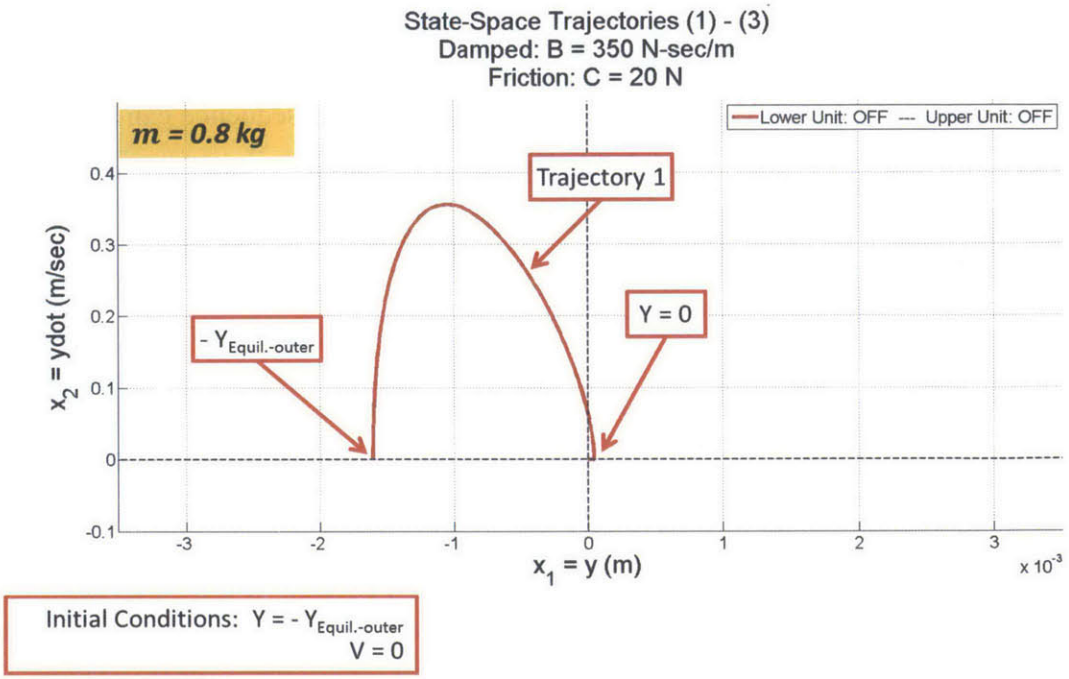

Figure 5-8: Switching Sequence 1-3-4-5: Trajectory 1 with initial conditions at the negative outer equilibrium, and subject to activation state (3).

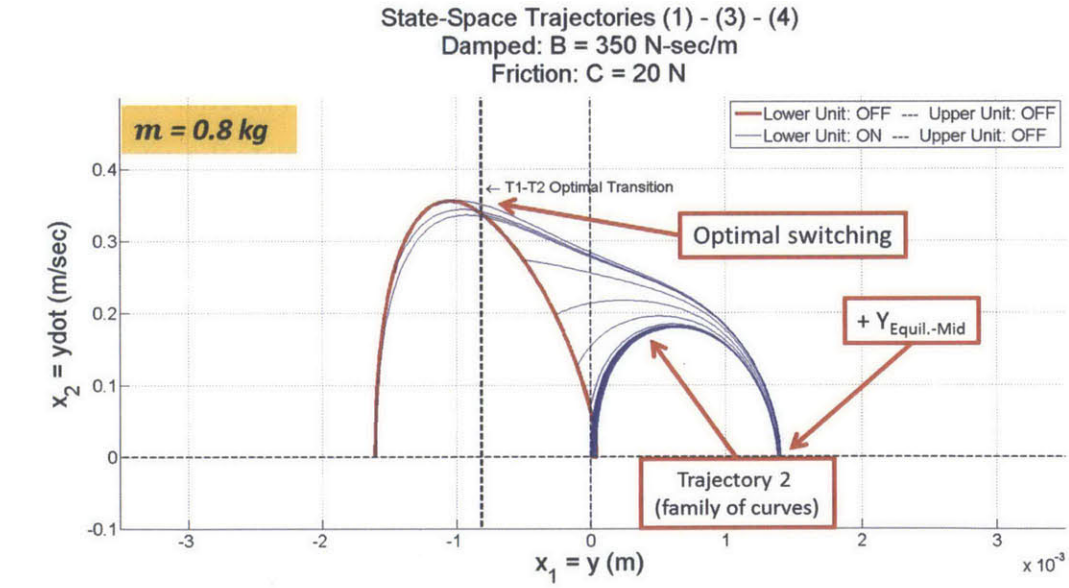

Figure 5-9: Switching Sequence 1-3-4-5: Family of curves for Trajectory 2 with initial conditions occurring on Trajectory 1, and subject to activation state (4).

While all of the blue trajectories in Figure 5-9 are appropriate for providing positive displacement during the **1→3→4→5** sequence, a single optimal trajectory may be identified. The primary objective during dynamic actuation is to obtain the shortest possible transition time, or,

in other words, the fastest switching sequence. By remembering that the switching distance between (–) $\mathbf{Y_{EQUIL\text{-}OUTER}}$ ←→ (+) $\mathbf{Y_{EQUIL\text{-}OUTER}}$ is constant regardless of the shape or length of the phase plane trajectory, the fastest transition is then achieved by maximizing the velocity state, point by point, along the position state from (–) $\mathbf{Y_{EQUIL\text{-}OUTER}}$ to (+) $\mathbf{Y_{EQUIL\text{-}OUTER}}$. In effect, this is done by choosing the secondary trajectory (and subsequently tertiary trajectory) which immediately exceeds the previous trajectory's velocity at the secondary trajectory's initial conditions.

From Figure 5-9, all of the blue trajectories which initiate to the left of the vertical dashed line labeled "T1-T2 optimal transition" immediately exhibit a velocity value lower than the original red trajectory. Thus, none of these trajectories are optimal for shortest transition time. All of the blue trajectories which initiate to the right of the T1-T2 optimal transition line immediately exceed the velocity of the primary trajectory and are therefore candidates for the optimal trajectory.

However, one additional behavior of phase plane analysis must be pointed out to identify the optimal trajectory. Assuming the forcing function is single valued, the slope of a trajectory at any position in the phase plane, other than at zero velocity and zero position, will only have one value and therefore no trajectories belonging to the same activation configuration will cross [15]. Then, the optimal secondary trajectory begins at the first instance where the velocity of that trajectory immediately begins to exceed that of the first trajectory. In the limit of infinitely closely spaced trajectories, this occurs when the slopes of the two trajectories match as is described in Eq. (5.11) and shown in Figure 5-10. Thus the switch position control law is defined by Eq. (5.11).

$$\left.\frac{dx_2}{dx_1}\right|_{Traj.(n+1)} = \left.\frac{dx_2}{dx_1}\right|_{Traj.n}$$
$$where: \qquad (5.11)$$
$$x_2 = \dot{y}$$
$$x_1 = y$$

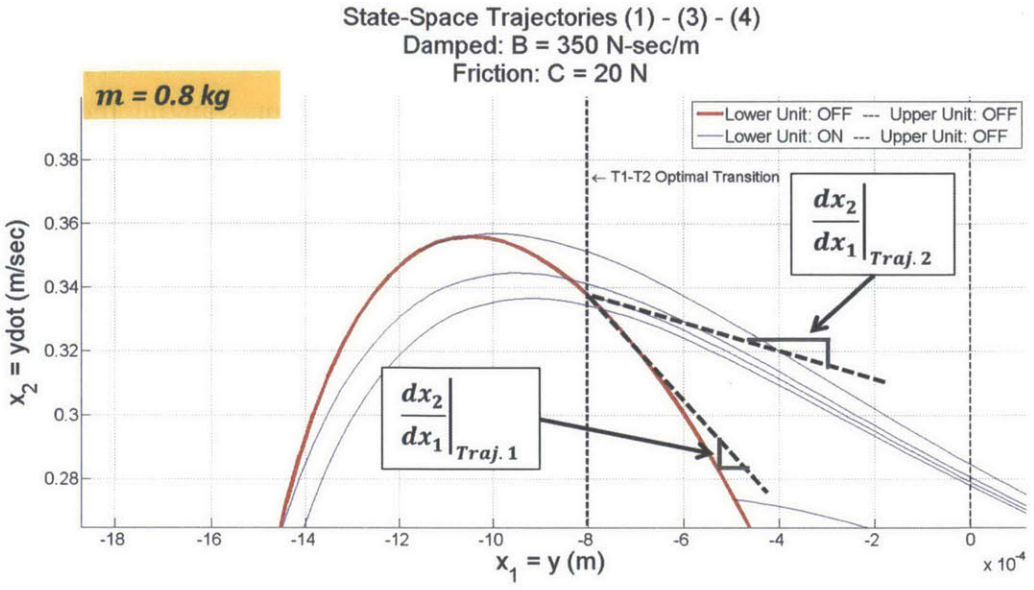

Figure 5-10: Close up view of the switching sequence 1-3-4-5 and the optimal T1-T2 transition point.

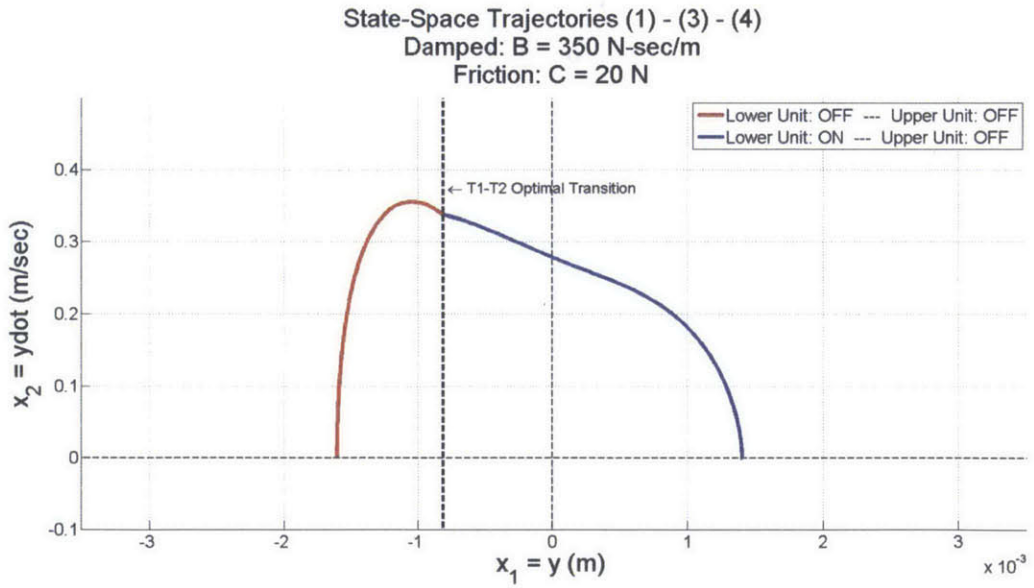

Figure 5-11: Switching Sequence 1-3-4-5: Optimal Trajectory 2 is plotted in blue extending from Trajectory 1 in red. The optimal switching position was numerically solved using the switch position control law.

Figure 5-11 then displays the optimal secondary trajectory which has been solved numerically using Eq. (5.11). The secondary trajectory does not reach the positive outer equilibrium so the final activation state (4) and its corresponding equilibrium configuration (5) must be applied. This last state leads to the set of green curves shown in Figure 5-12. The green curves represent activation state (1) where both actuator units are energized. From Figure 5-5, this activation can lead to two equilibrium configurations (1) or (5). This effect is visible in the figure below where a switching position threshold exists. Along Trajectory 2 and prior to this threshold, switching prematurely to activation state (1) will drive the output back to the original starting point at (–) $Y_{EQUIL\text{-}OUTER}$. This would defeat the purpose of switching the dual unit actuator. By delaying the switching until some position beyond this threshold is reached, full transition to the intended equilibrium point is achieved.

Following the switch position control law of Eq. (5.11), the optimal trajectory 3 can be obtained. By linking trajectory 1 with optimal trajectories 2 and 3, the composite trajectory representing the minimum total transition time is plotted in Figure 5-13. This procedure may be repeated for any switching sequence such as those listed in Table 5-1 and Table 5-2.

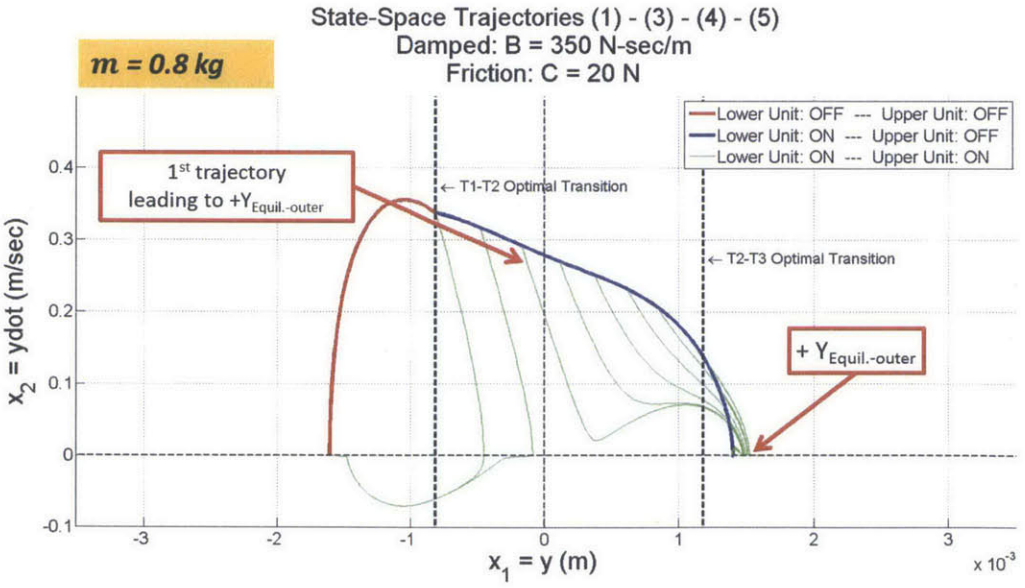

Figure 5-12: Switching Sequence 1-3-4-5: A family of curves representing Trajectory 3 is plotted departing the optimal Trajectory 2. The green curve represents configuration (5) which uses activation state (1).

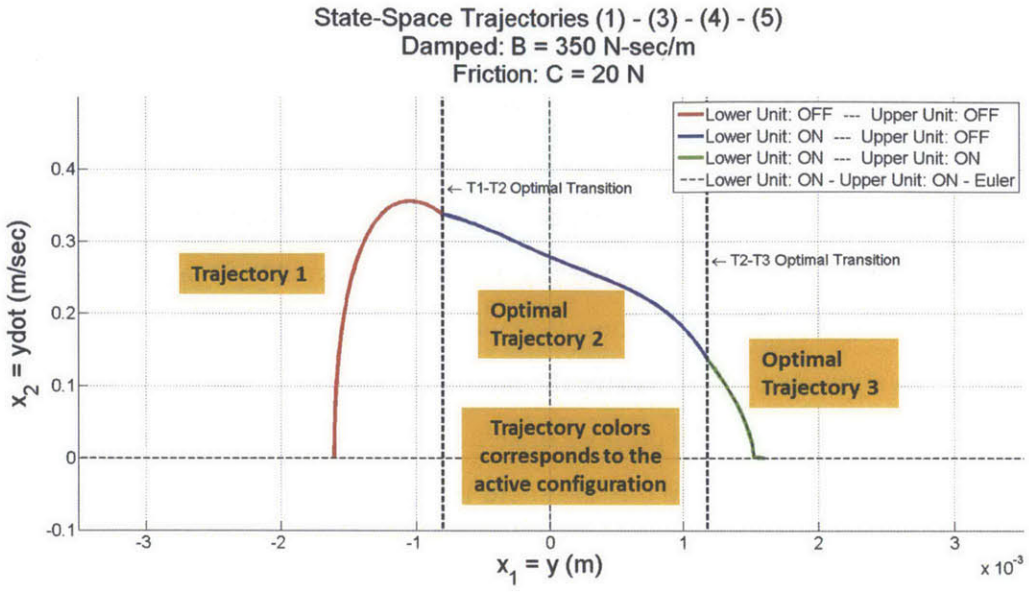

Figure 5-13: Switching Sequence 1-3-4-5: Optimal Trajectory 3 is combined with optimal Trajectory 2, and Trajectory 1 to represent the composite trajectory.

With the optimal composite trajectory plotted, the total transition time from initial conditions to the "destination" position of the desired switching motion may be derived in the general form by Eq. (5.12). Since a closed form solution does not exist, numerical integration must be used. Calculating the switch position timing, T1, and T2 is trivial since these times correspond to the time steps where the switch position control law of Eq. (5.11) is met. These time steps may be extracted directly from the numerical integrator. This is shown in the MATLAB code of APPENDIX A. Calculating the transition time for the last trajectory is a bit more challenging. For this trajectory, the number of time steps to reach a y-position within a tolerance band is tabulated. An example of this tolerance band is shown in Figure 5-14.

$$\dot{y}(t) = \frac{dy(t)}{dt} \quad \rightarrow \quad \int_{t_0}^{t_{final}} dt = \int_{-Y_{initial}}^{+Y_{final}} \left(\frac{1}{\dot{y}}\right) dy \tag{5.12}$$

A tabulation of some comparative total transition times for several switching sequences is listed in Table 5-3. In these simulations, a load of 0.5 kg, damping of 350 N-sec/m, and a friction force of 20 N is assumed. As is highlighted in green, the **1→4→5** sequence is the fastest transition sequence at 0.176 sec while the **1→3→4→5** sequence is barely slower at 0.177 seconds.

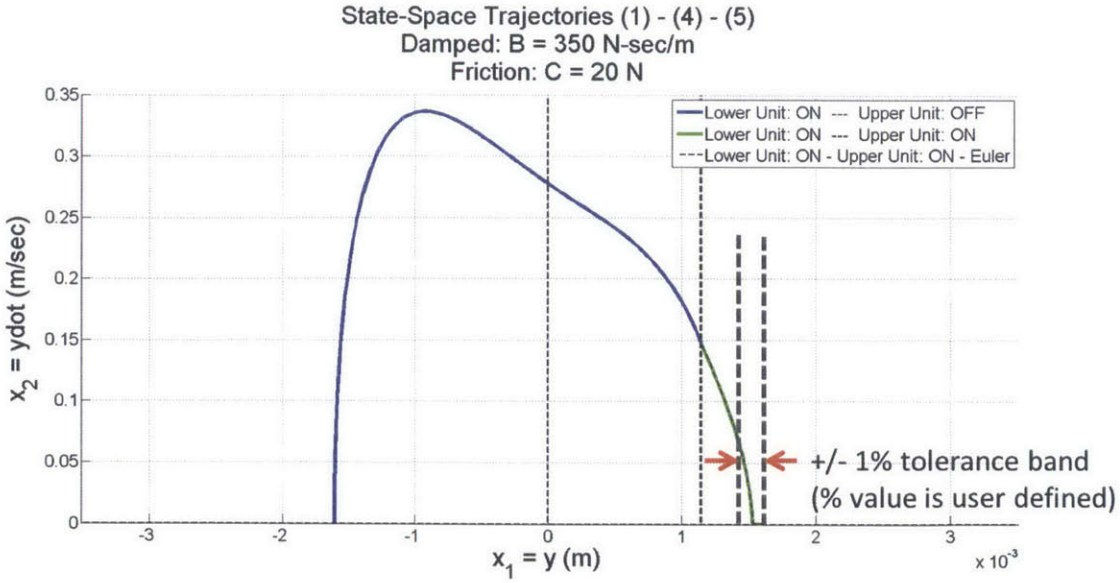

Figure 5-14: Phase plane plot indicating the tolerance band method to define the upper limit of integration during transition time calculation.

Sequence M = 0.8 kg B = 350 N-s/m C = 20 (N)	Quasi-static (Y/N)	Dynamic (Y/N)	Total Transition Time (s)	Notes
1 → 2 → 5	No	No	N/A	Requires an initial condition beyond equilibrium point
1 → 3 → 5	No	Yes	**T_T = 0.508 sec** (T_1 = 0.0081 sec)	Dependent on mass (m), damping (B), friction (C) parameters
1 → 4 → 5	Yes	Yes	**T_T = 0.176 sec** (T_1 = 0.0111 sec)	
1 → 2 → 3 → 5	No	Yes	N/A	Dependent on m, B, C parameters (optimal switching: 1→3→5)
1 → 2 → 4 → 5	Yes	Yes	N/A	Optimal switching will default to: 1→4→5
1 → 3 → 4 → 5	Yes	Yes	**T_T = 0.177 sec** (T_1 = 0.0031 sec) (T_2 = 0.0112 sec)	Minimum transition time

Table 5-3: Tabulation of comparative total transition times for several difference switching sequences.

5.5. Measured Performance

5.5.1. Static Force-Displacement Experimental Performance

A prototype dual unit actuator has been assembled to experimentally validate the static force properties, the dynamic model, and to confirm the optimal switch position control law described earlier in this chapter. This prototype, which couples together two flexure free buckling actuators, is shown in Figure 5-15 below. The buckling units in this figure are contained within large steel frames which not only give the actuators a stiff structure but also provide a platform for attaching measurement and load equipment. The dual unit actuator degree of freedom is shown by the blue arrow situated above the rigid coupler. Prior to measuring the aggregate dual unit force property, the individual force behaviors of each unit have been measured as shown in Figure 5-16 and Figure 5-17.

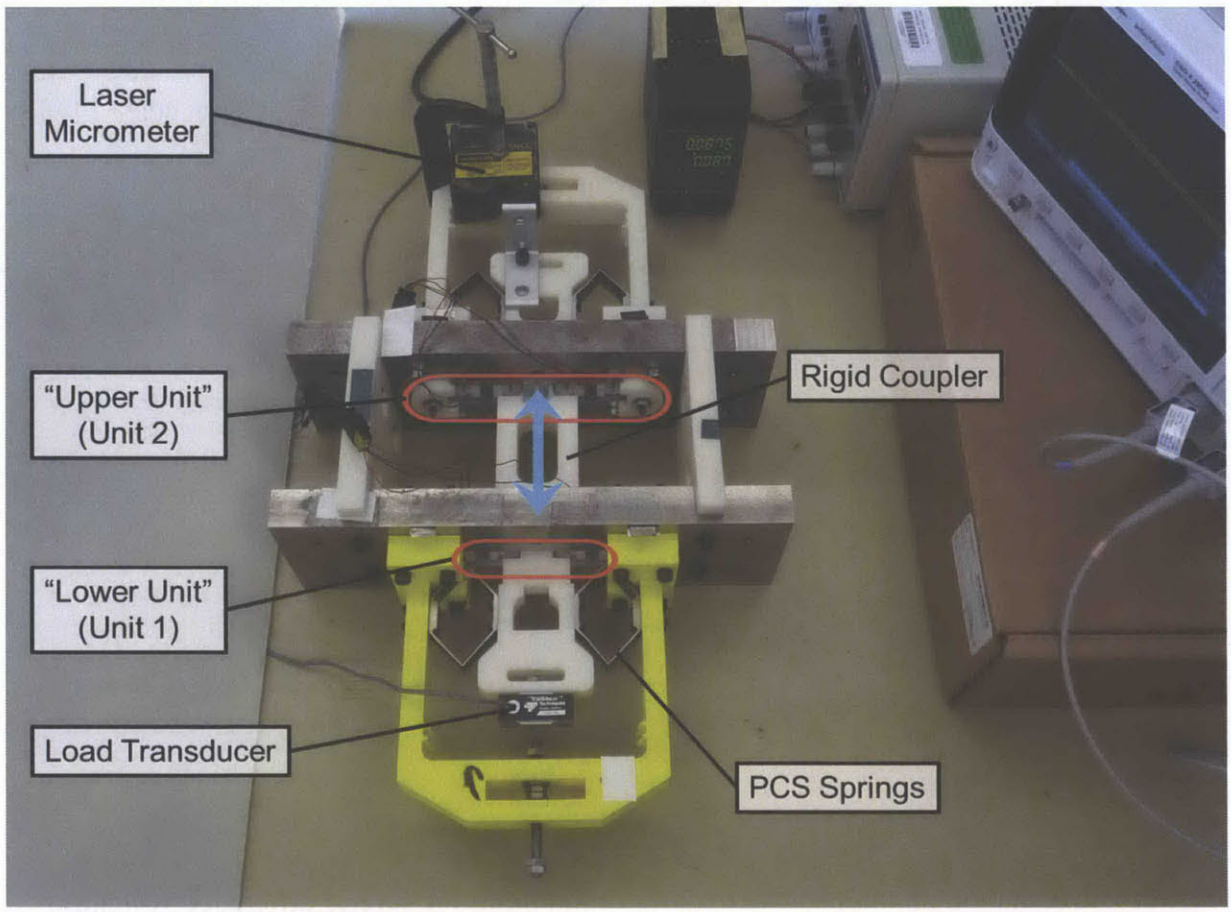

Figure 5-15: Prototype of the dual unit buckling actuator used in experimental testing and measurement. The lower and upper units are labelled with the PCS and coupler components, as well as the displacement and force measurement devices.

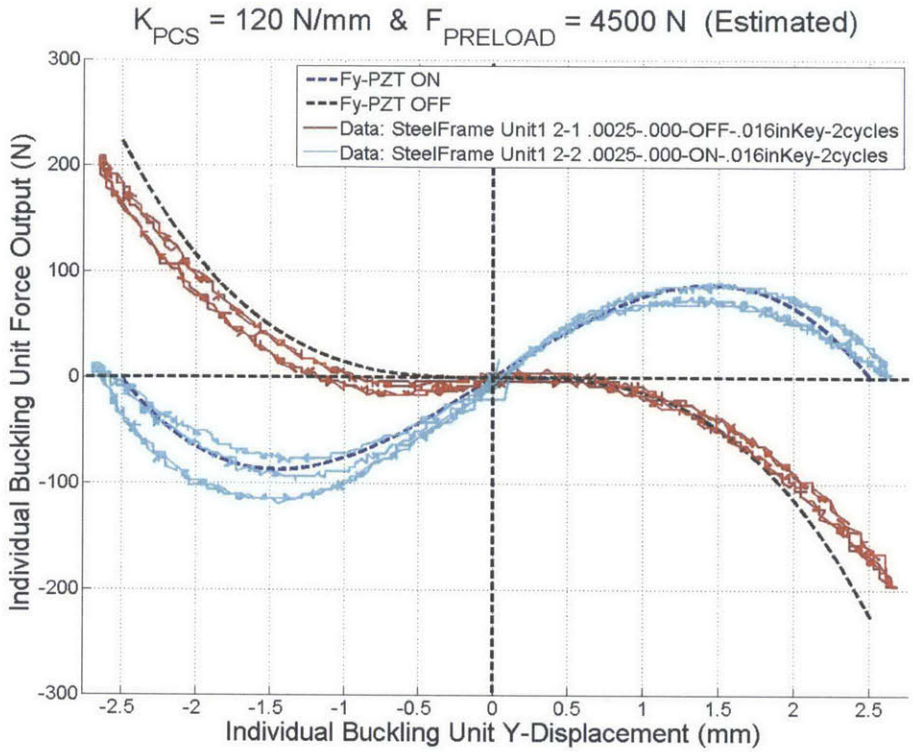

Figure 5-16: Individual performance of the Lower Unit (Unit 1). Note that the preload force is estimated at 4500 N.

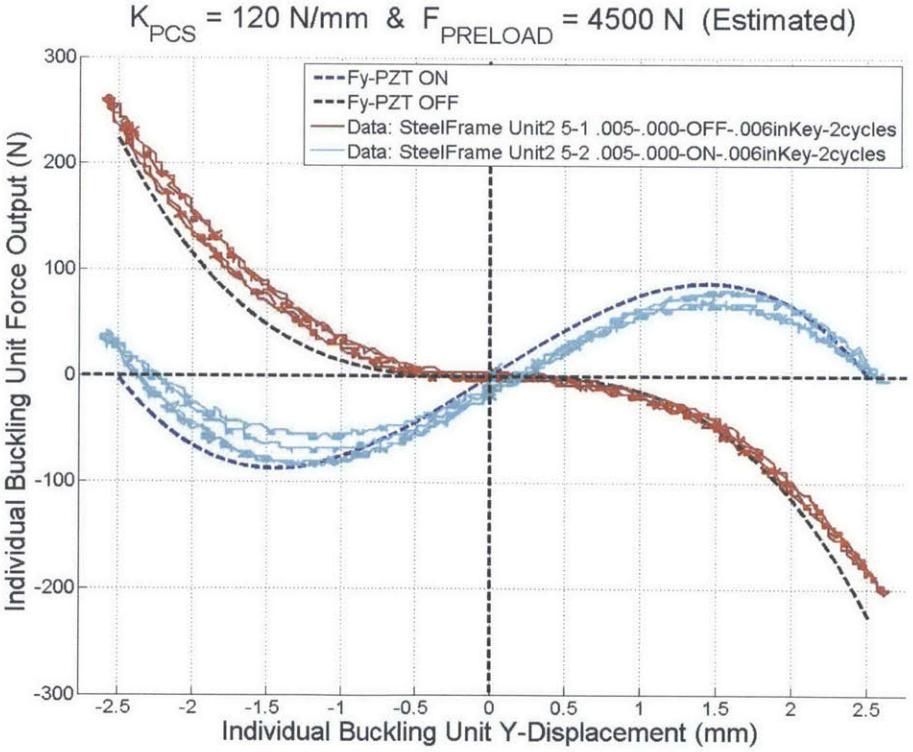

Figure 5-17: Individual performance of Upper Unit (Unit 2). Note that the preload force has been estimated at 4500 N.

In the experimental prototype, preloading of the buckling units is performed by shimming between the PZT stack actuators and the PZT caps. Shimming is performed incrementally using shims of .0005 inch thickness. This results in a coarse preload force increment, and it is important to "fit" individual buckling unit simulations to the measured data. Although the preload force accounts for only one of the unmeasured variables, it is assumed from previous measurements that the stiffness of the PZTs and PCS springs are well known, and that the PZT force is as published in manufacturer data.

Figure 5-16 and Figure 5-17 show that the force preload estimation of 4500 N for each individual buckling actuator is appropriate. This observation is important for two reasons. First, the preload value is lower than the preload assumed in the static force simulation of Figure 5-5. This means that an updated static force simulation for comparison against the measurement data in Figure 5-18 will be required. This is shown in Figure 5-19. The second reason is balancing the individual units against each other to prevent load biasing in the aggregate output force.

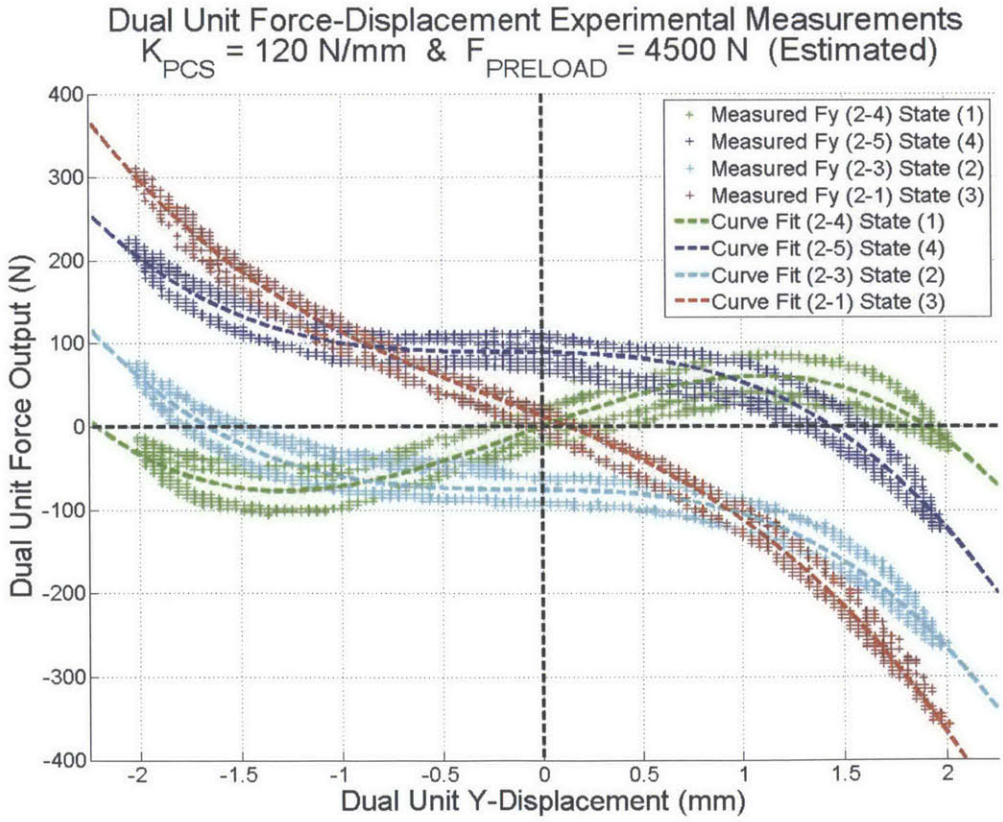

Figure 5-18: Static force-displacement measurement data of the dual unit actuator for the four activation states. Curve fitting via cubic polynomials is also shown.

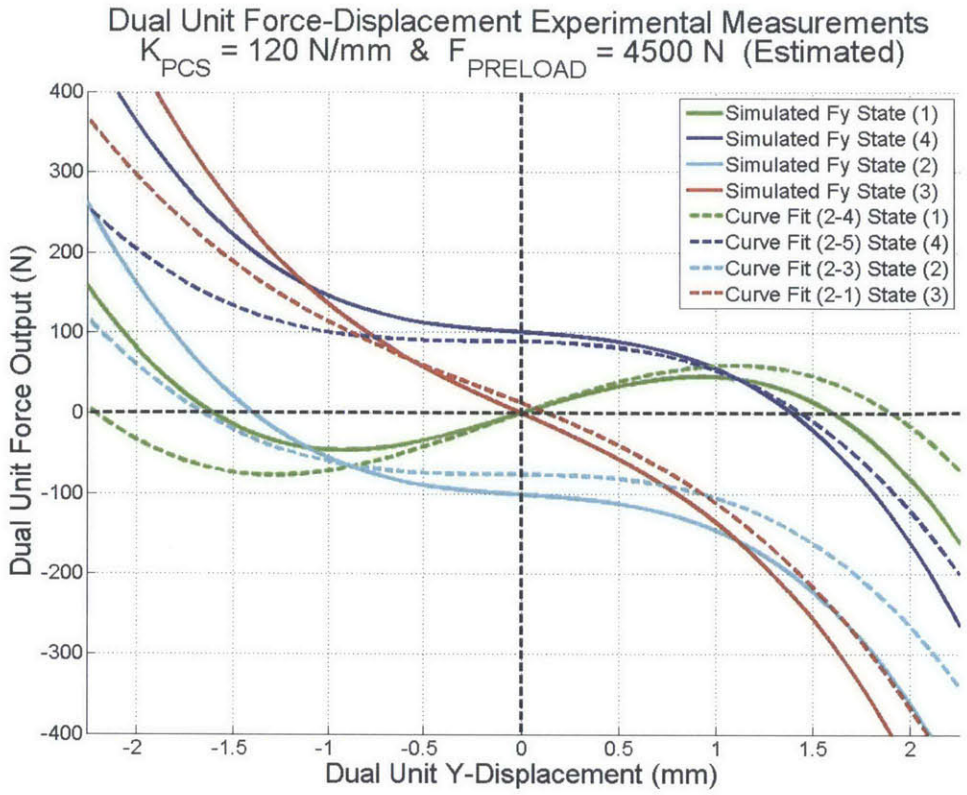

Figure 5-19: Updated force-displacement simulation at preload force of 4500 N vs. the measured data fitted curves.

The final static force properties of the experimental dual unit actuator are shown in the above two figures. The wide spread of the raw measurement data of Figure 5-18 shows the effect that hysteresis within the PZT stack actuators has upon the aggregate force output. To compress this data slightly, curves have been fit to the raw data using cubic polynomials. These fitted curves are then shown against the simulated static force property, now updated with a preload force of 4500 N, in Figure 5-19. The measured data performs better than the simulation in state (1) where both units are active. In states (2) and (4), where only one unit is active, the aggregate force underperforms by approximately 15% throughout the range. In state (3) where both units are off, the fitted curve and simulation show good correlation between +/- 1 mm displacement. Outside of this range, the correlation degrades. These behaviors indicate that the preload estimate of 4500 N may be an underestimate. For the purposes of general discussion however, the static force properties seem to follow the model derived earlier in this chapter.

5.5.2. Experimental Dynamic Performance

Preliminary dynamic evaluation of the dual unit actuator is shown here. Initial testing has shown quick transition on the order of less than 30-40 milliseconds for the actuator to transition between the outer equilibrium points without driving a load. Underdamped oscillations can be heard by a short "ringing" but the oscillatory displacement is not visible to the eye. To increase the transition time and study the damping characteristics, a load mass of 3.6 kg was attached to the coupler shown in Figure 5-15 in addition to the equivalent mass of 0.3 kg of the moving components in the actuator. The laser micrometer data was sent to an oscilloscope and sampled at 10 kHz. Using the forward difference method, the actuator output velocity was derived from the raw data position and the oscilloscope timing. The position and velocity have then been plotted to create the following three phase portraits. Figure 5-20 represents the dual unit actuator initially positioned at the negative outer equilibrium with both upper and lower units turned on. Both units are then simultaneously turned off and the following position and velocity data can be extracted.

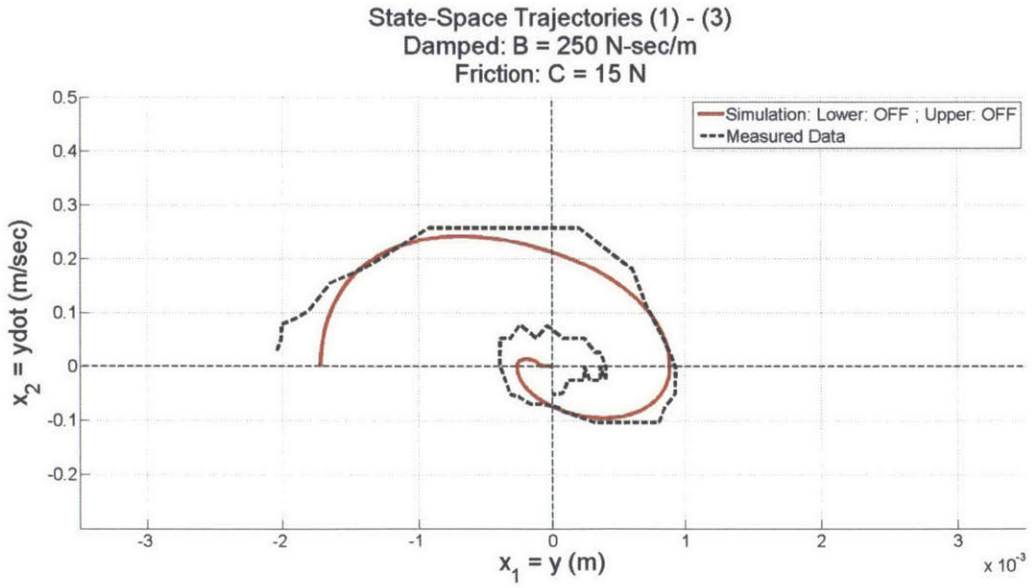

Figure 5-20: Simulation and measured data plotted as a phase plane trajectory indicating the switch from state (1) to state (3)

The black dotted line represents the measured data while the red line is a simulation trajectory. The fitting of the two trajectories has been performed by trial and error with the damping coefficient arriving at 250 N-sec/m, and a constant coulomb friction value of 15 N.

With the approximate fit between trajectories shown above, the simulation code outputs an optimal switching position and time to go from state (3) to state (4). In this experiment, the first optimal transition, T1, is 0.0051 seconds. This timing becomes an input for the next block of simulation code. Measuring and plotting the position and velocity again provides the phase portrait of Figure 5-21. Note that there is relatively good agreement between the simulated and measured trajectories until reaching the vicinity of the positive outer equilibrium. Here the measurement data appear to run into enough friction to dampen any oscillation. The optimal switch position control law provides a second transition time, T2, or .0142 seconds.

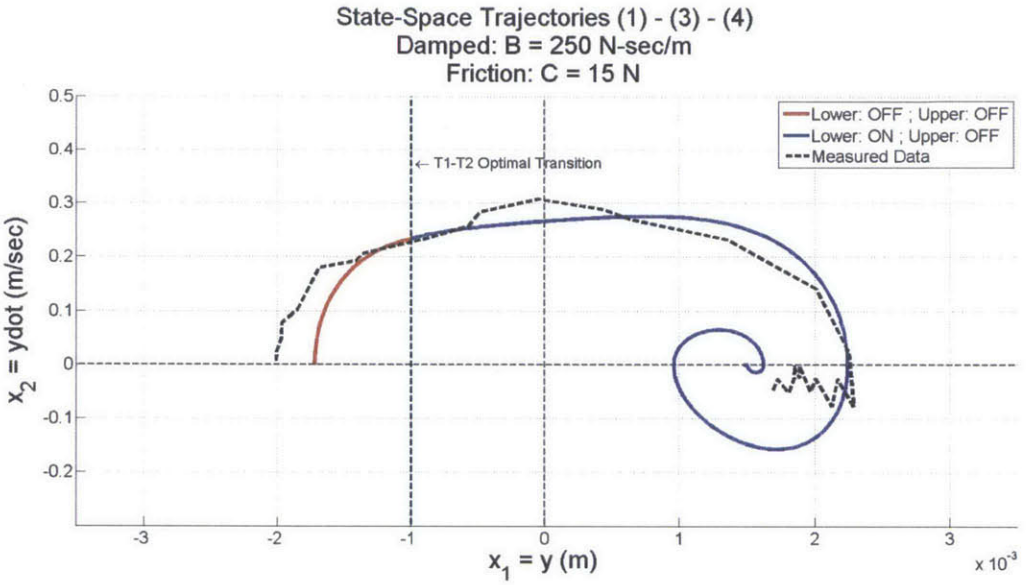

Figure 5-21: Simulation and measured data plotted for the phase plane trajectory now indicating two transitions: state (1) to state (3) to state (4).

The final piecewise trajectory is shown in Figure 5-22. Here the two units are both turned on and driving the output towards the positive outer equilibrium. The measured data and simulation correlation has broken down significantly at this point. The simulation underestimates velocity crossing through Y=0, and then indicates at least one cycle of oscillation of greater magnitude than the measurements shows. The total transition time for this trajectory is 0.0328 milliseconds.

This data is preliminary and more concerted efforts should be applied to verify that the estimated damping and friction parameters are close to the true values. Clearly from the data the model does not fully match the measured results. The position measurement using the laser micrometer is very accurate, but the sampling rate of the laser micrometer is not sufficient to

keep up with the speed of the dual unit actuator. An alternate velocity measurement technique is necessary. Regardless of the complete accuracy between the model and measured data, these three figures indicate that the nonlinear dynamic model developed in this chapter is in fact representative of the actual dynamic performance of the dual unit actuator. Future efforts to characterize the damping and friction values will close the gap between measurement and simulation.

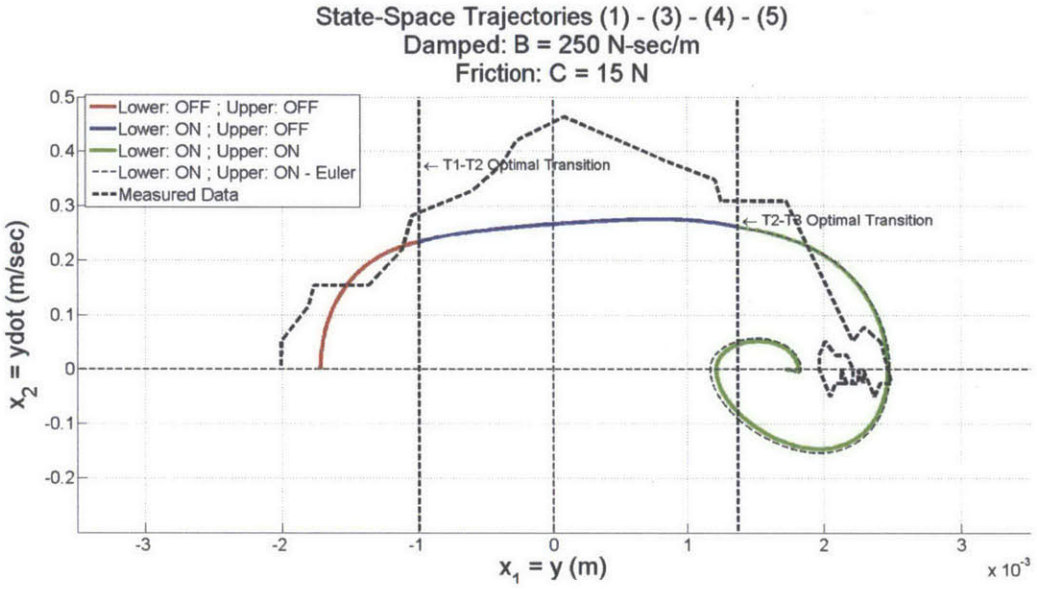

Figure 5-22: Simulation and measured data plotted for the full trajectory now indicating three transitions: state (1) to state (3) to state (4) to state (5).

Chapter 6

6. Conclusions

This thesis has expanded upon previous piezoelectric buckling actuator research to improve form factors, explore new methods of deterministic direction control, and to study dynamic motion and optimal actuation sequencing. Beginning with a well-developed buckling actuator design, two design changes have been proposed which promise to improve performance while at the same time making the actuator device more compact and lighter. The use of carbon fiber to build the stiff actuator frame is ideal particularly if the anisotropic properties of the material are exploited. The specific Young's modulus, can reach values of 253 (GPa/(g/cc)) compared to that of structural steels which is only ~25 (GPa/(g/cc)) for a specific elastic modulus improvement of 8-10x. Another potential design improvement involves the geometry and material choice for the rolling contact components. This thesis has presented that the optimal geometry for rolling contact stiffness is to use rolling contact of parallel cylinders. In addition, while steel bearing elements are most common, synthetic sapphire (Al_2O_3) and tungsten carbide represent two materials which have greater elastic modulus than that of steel. The Young's modulus of steel is approximately 210 GPa, whereas for synthetic sapphire it approaches 450 GPa, and tungsten carbide can exceed 600 GPa. In the specific prototype design, this leads to a joint stiffness of 6.645 when normalized to the PZT stiffness. By using synthetic sapphire and tungsten carbide, the normalized joint stiffness increases to 12.61 and 17.22, respectively.

This thesis has also explored a new method to control output stroke direction when functioning as a standalone unit. Prior research has considered linking multiple buckling units together or asynchronously activating the PZTs of a single buckling actuator to control output. If minimizing the number of active elements (PZTs) in a device is of interest, then switching mechanism reviewed here can act as an alternative design to the asynchronous activation technique. The switching mechanism has several features which must be considered when deciding on whether or not to include that device in an application. First, the output of the coupled switching mechanism – buckling actuator will be deterministic but also alternating. Design of the cam-groove shape provides for both energy storage into the cam plate spring, as well as a method to "shape" or transform the nonlinear buckling actuator force into a more useful force shape.

The experimental prototype of the switching mechanism shows that the fundamental concept will work however there are several implementation challenges that need consideration. The first is that the device has a higher number of moving components than the asynchronous switching device mentioned above. This raises the overall level of complexity. The output of the buckling actuator is also small, and therefore the scale of the cam-groove, the latching gate, and the cam-follower linking the switching mechanism to the buckling unit is also very small. This limits the minimum size that such a device can practically be manufactured.

The final section of this thesis studies the dual unit buckling actuator which has buckling units arranged in parallel but spatially out of phase. This design and the asynchronous activation technique that is used in conjunction have been previously studied however this thesis has developed the dynamic model and arrived at an optimal switching technique to minimize total switching time. Although the system is highly nonlinear, phase plane analysis has been effective in graphically demonstrating the behavior of the device. The static force properties show that under appropriate geometry the device can achieve a displacement of 4 mm while producing a nearly constant 100 N force through the middle 2-3 mm of the range. The experimental device has also been used dynamically. The parameters for damping and friction used in the simulation are exaggerated, and the actual transition motion of the dual unit actuator is significantly faster than expected. As the dynamic data indicates, the device can switch between outer equilibrium points while driving a 4 kg load in less than 33 milliseconds. Multiple switching sequences have

been suggested, and the position switching control law allows any specific load, damping, and friction parameters to be accommodated with minimal transition timing.

Future work in this area can expanded upon the promising results of the dual unit actuator in its dynamic operating mode. Implementation of improved position and velocity measurements to a prototype or beta device will allow for closer estimation of the dynamic model to the actual device. This further aligns the calculated optimal switching with reality.

APPENDIX A

The following MATLAB script and function were used to calculate and plot the phase plane trajectories for the dual unit buckling actuator simulations. Specifically this script runs the (1)-(3)-(4)-(5) switching sequence. The optimal switch position control law is contained herein and the optimal transition positions, velocities, and timing are outputs of running the code.

MATLAB Calling Function:
"Dynamic_EOM_FUNC_DmpFric.m"

```
function xdot = Dynamic_EOM_FUNC_DmpFric(~,x)
global PP QQ RR SS CC DD

% Template for state equations.
% Extract states (just for readability)
x1 = x(1);
x2 = x(2);

% State equations
x1dot = x2;
x2dot = PP*x1^3 + QQ*x1 + RR + SS*x2 + CC*tanh(DD*x2);
% Return the state derivatives to the ODE solver
xdot = [x1dot; x2dot];
```

MATLAB Script:
"Dual_BucklingUnit_NonLinear_Dynamic_DmpFric_Optimal_1_3_4_5.m"

```
%% BLOCK 1
%Flexure Free Rolling Contact, Dual - Buckling Unit
%Phase-Plane Analysis

clear
clc

%Buckling Unit Parameters
F_B = 5250;      %N (Max Blocking Force @ 150 V)

F_B12_ON = 5250;     %N Force in lower unit PZT pair - ON (each PZT)
F_B12_OFF = 0;       %N Force in lower unit PZT pair - OFF (each PZT)

F_B34_ON = 5250;     %N Force in upper unit PZT pair - ON (each PZT)
F_B34_OFF = 0;       %N Force in upper unit PZT pair - OFF (each PZT)

F_PL = 5100;         %N (Preload force, ideal = 5250, experimental = 5100)
z_free = 42E-3;      %mm, 42 micron (Published Value)

r = 23;              %mm; cap radius
R = 14.5;            %mm; end cap and keystone radius
L = 2*(r+R);         %Characteristic length (at rest)
Lmeter = L/1000;  %meters (use for dynamic calcs)
```

```
Kpzt = F_B/z_free;          % N/mm; Published PZT stiffness
Kj = 531600;                % N/mm (Kj/Kpzt = 6.645 when Kpzt = 80 N/mcrn)
K_frame_2 = 1600000;        % N/mm (K_frame_2 / Kpzt = 20, when Kpzt = 80 N/mcrn)

Kserial = 1/((1/K_frame_2)+(2/Kj));
% Kpcs = (2*F_PL)/L
Kpcs = 120;                 %Measured stiffness of PCS (experimental setup)
Kpcsmeter = Kpcs*1000;      %N/m(use for dynamic calcs)


delta_PL = F_PL*((Kpzt+Kserial)/(Kpzt*Kserial));
z_max = z_free + delta_PL;

K1 = ((Kpzt*Kserial)/(Kpzt+Kserial));
K1meter = K1*1000;                          %N/m use this for dynamic calcs
K2 = (Kserial/(Kpzt+Kserial));              %[-] dimensionless

%Layout Parameters
theta = 0.850               %Degrees (misalignment angle)
theta_rad = theta*(pi/180);

%Dynamic System Parameters
M_equiv = 0.3;              %kg (PCSs, Keystones, Caps, PZTs, Coupler, etc...)
M_load = 0.5;               %kg

M = M_equiv + M_load;       %kg

B_Dmp = 350;                %Estimated damping coefficient %N-sec/m
Cfric = 20;                 %Friction Force (N) coefficient
Dfric = 500;                %Factor addressing tanh()"step"
                            %larger Dfric --> approaches signum

% Solve for Equilibrium Point - Mid (Numerically - MATLAB)
% Set Fy_comb = 0, with F_B34 = 0
% Solve for roots of cubic Ax^3 + Bx^2 + Cx + D = 0
% A = 1, B= 0

A = 1;
B = 0;
C =   ((L^2)/(-2*K1))*(  ((4*F_PL)/L)  -  2*Kpcs  -  K1*6*(tan(theta_rad)^2)  ...
      +2*(K2/L)*(F_B12_ON + F_B34_OFF) );

D =   ((L^2)/(-2*K1))*(2*K2*tan(theta_rad)*(F_B12_ON - F_B34_OFF));

G = [A B C D];
G_roots = roots(G);
Y_Equil_mid = max(abs(real(G_roots)))          % Equilibrium point
Y_Equil_mid_meter = Y_Equil_mid/1000;          % Equilibrium point (meters
                                               % use for dynamic calc)

% Solve for Equilibrium Point - Outer (Numerically - MATLAB)
A2 = 1;
B2 = 0;
C2 =   ((L^2)/(-2*K1))*(   ((4*F_PL)/L)   -   2*Kpcs   -   K1*6*(tan(theta_rad)^2)
      +2*(K2/L)*(F_B12_ON + F_B34_ON) );
```

```
D2 =  ((L^2)/(-2*K1))*(2*K2*tan(theta_rad)*(F_B12_ON - F_B34_ON));

G2 = [A2 B2 C2 D2];
G2_roots = roots(G2);
Y_Equil_outer = max(abs(real(G2_roots)))          % Equilibrium point
Y_Equil_outer_meter = Y_Equil_outer/1000;         % Equilibrium point (meters
                                                  % use for dynamic calc)

%%%%%%%%%%%%%%%%%%%%%%%%%%%%%%%%%%%%%%%%%%%%%%%%%%%%%%%%%%%%%%%%%%%%%%%%%%%
%%%%%%%%%%%%%%%%%%%%%%%%%%%%%%%%%%%%%%%%%%%%%%%%%%%%%%%%%%%%%%%%%%%%%%%%%%%



%% BLOCK 2
% Plotting Trajectory 1 of this switching sequence
%(i.e. State (3) Both Units OFF)

% Time-integration of state equations.
clear global;                  % clear any pre-existing global variables
global PP QQ RR SS CC DD;      % pass system parameters to the function called
                               % below in ODE##, 4 var. reqd. for this system

% Dynamic System Parameter Coefficients
%%%%%%%%%%% Units: Lower OFF, Upper OFF %%%%%%%%%%
% Note all parameters are divided by mass M

PP = (-2*K1meter)/((Lmeter^2)*M);

QQ = ( (4*F_PL)/(Lmeter*M) - 2*(Kpcsmeter/M) - ...
       (K1meter/M)*6*(tan(theta_rad)^2) + ...
           2*(K2/(Lmeter*M))*(F_B12_OFF + F_B34_OFF) );

RR = 2*(K2/M)*tan(theta_rad)*(F_B12_OFF - F_B34_OFF);
SS = -(B_Dmp/M);
CC = -Cfric/M;
DD = Dfric;

% Simulation time
tsim = 0.5;       %seconds

% Define the simulation time vector
sfrq = 10000;                  % sampling frequency Hz
tvec = (0:1:sfrq*tsim)/sfrq;
tstep = 1/sfrq;
totsteps = length(tvec);
tfinal = (sfrq*tsim)/sfrq;

% Starting state (Initial Conditions)
x1_T1 = -Y_Equil_outer_meter;       %m
x2_T1 = 0;                     %m/sec

% Initial state vector
x0_T1 = [ x1_T1; x2_T1 ];

% Use ode23s to integrate the state equations (Stiff, Low to med. accuracy)
[t, x] = ode23s('Dynamic_EOM_FUNC_DmpFric', tvec, x0_T1);
```

```
% Extract states (just for readability)
x1_T1 = x(:,1);                 %Full vector of State 1 - Traj. 1
x2_T1 = x(:,2);                 %Full vector of State 2 - Traj. 1


% Plot State-Space Trajectory:
figure(1);
clf(1);
set(gca,'FontSize',20)
hold on;
grid on;
plot(x1_T1,x2_T1,'r', 'LineWidth',4)
xlim([-.0035 .0035])
ylim([-0.1 0.5])

title({'State-Space Trajectories (1) - (3)'; ...
      ['Damped: B = ', num2str(B_Dmp), ' N-sec/m']; ...
      ['Friction: C = ', num2str(Cfric), ' N']},'FontSize',30);
xlabel('x_1 = y (m)','FontSize',30);
ylabel('x_2 = ydot (m/sec)','FontSize',30);
legend('Lower Unit: OFF  ---  Upper Unit: OFF');

%Place darker lines over Y and X axes
Xaxis = get(gca,'XLim');
line(Xaxis,[0 0],'Color','k','LineStyle','--','LineWidth',2);
Yaxis = get(gca,'YLim');
line([0 0],Yaxis,'Color','k','LineStyle','--','LineWidth',2);

%%%%%%%%%%%%%%%%%%%%%%%%%%%%%%%%%%%%%%%%%%%%%%%%%%%%%%%%%%%%%%%%%%%%%%%%%%%%%%%
%%%%%%%%%%%%%%%%%%%%%%%%%%%%%%%%%%%%%%%%%%%%%%%%%%%%%%%%%%%%%%%%%%%%%%%%%%%%%%%



%% BLOCK 3
% Now Plot set of secondary Trajectories from Trajectory 1 I.C.
% (i.e. state (3) - state (4)'s) - also find optimal switching point and
% trajectory 2

% New Figure
figure(2);
clf(2);
set(gca,'FontSize',20)
hold on;
grid on;

% REPLOT Trajectory 1:
plot(x1_T1,x2_T1,'r', 'LineWidth',4)
xlim([-.0035 .0035])
ylim([-0.1 0.5])

title({'State-Space Trajectories (1) - (3) - (4)'; ...
      ['Damped: B = ', num2str(B_Dmp), ' N-sec/m']; ...
      ['Friction: C = ', num2str(Cfric), ' N']},'FontSize',30)
xlabel('x_1 = y (m)','FontSize',30)
ylabel('x_2 = ydot (m/sec)','FontSize',30)

T1_final_step = length(x1_T1);      %number of points (steps) in T1 curve
```

```
clear global;                   % clear any pre-existing global variables
global PP QQ RR SS CC DD;       % pass system parameters to the function called
                                %below in ODE##, 4 var. reqd. for this system

% Dynamic System Parameter Coefficients
%%%%%%%%%%% Units: Lower ON, Upper OFF %%%%%%%%%%
% Note all parameters are divided by mass M
PP = (-2*K1meter)/((Lmeter^2)*M);

QQ = ( (4*F_PL)/(Lmeter*M) - 2*(Kpcsmeter/M) -...
      (K1meter/M)*6*(tan(theta_rad)^2) +...
          2*(K2/(Lmeter*M))*(F_B12_ON + F_B34_OFF) );

RR = 2*(K2/M)*tan(theta_rad)*(F_B12_ON - F_B34_OFF);
SS = -(B_Dmp/M);
CC = -Cfric/M;
DD = Dfric;

T2_init_step = 10;              %Number of steps to jump for each curve
i=0;                        %index "switch" for "FALSE" in nested if statement

for n = 1:T2_init_step:T1_final_step-1     %n = index for set of curves
                                           %corresponding to "Trajectory 2"

    %Trajectory 1 states at Step n
    x1_T2 = x1_T1(n);
    x2_T2 = x2_T1(n);

    % Initial state vector (Trajectory 2)
    x0_T2 = [ x1_T2; x2_T2 ];

    % Use ode23s to integrate the state equations (Stiff, Low- med. accuracy)
    [t, x] = ode23s('Dynamic_EOM_FUNC_DmpFric', tvec, x0_T2);

    % Extract states (just for readability)
    x1_T2 = x(:,1);
    x2_T2 = x(:,2);

    % Plot State-Space Trajectory 2:
    plot(x1_T2,x2_T2,'b', 'LineWidth',1)

    % optimal switch point control law (numerically)
    if x2_T2(2) > x2_T1(n+1) && i<1
        fprintf('Optimal Switching Point is: \n');
        SwitchPositionT2 = x1_T1(n)
        SwitchVelocityT2 = x2_T1(n)
        SwitchStepT2 = n
        SwitchT2_Time = SwitchStepT2*tstep;
        fprintf(['Optimal 1st Switching Time:  ',num2str(SwitchT2_Time), ...
                 ' seconds \n\n']);
        i = i+1;
    else
%         fprintf('Still searching...');
    end
end
```

```
legend('Lower Unit: OFF  ---  Upper Unit: OFF', ...
       'Lower Unit: ON  ---  Upper Unit: OFF');

TransitionT2 = get(gca,'YLim');
line([SwitchPositionT2
SwitchPositionT2],TransitionT2,'Color','k','LineStyle','--','LineWidth',3);
text(SwitchPositionT2, .375,' \leftarrow T1-T2 Optimal ...
     Transition','Fontsize',18,'HorizontalAlignment','left');

%Place darker lines over Y and X axes
Xaxis = get(gca,'XLim');
line(Xaxis,[0 0],'Color','k','LineStyle','--','LineWidth',2);
Yaxis = get(gca,'YLim');
line([0 0],Yaxis,'Color','k','LineStyle','--','LineWidth',2);

%%%%%%%%%%%%%%%%%%%%%%%%%%%%%%%%%%%%%%%%%%%%%%%%%%%%%%%%%%%%%%%%%%%%%%%%%%%%
%%%%%%%%%%%%%%%%%%%%%%%%%%%%%%%%%%%%%%%%%%%%%%%%%%%%%%%%%%%%%%%%%%%%%%%%%%%%



%% BLOCK 4
%Plot truncated Trajectory 1 with Optimal Trajectory 2

% x1_T1 , x2_T1 states have not been modified since BLOCK 2 (just truncate)
x1_T1_short = zeros(SwitchStepT2,1);     %create empty vectors of length equal
                                         %to SwitchStepT2
x2_T1_short = zeros(SwitchStepT2,1);

for nn = 1:1:SwitchStepT2            %Shorten Trajectory 1 state vectors to
                                     %nn = 1 thru SwitchStepT2
    x1_T1_short(nn) = x1_T1(nn);
    x2_T1_short(nn) = x2_T1(nn);
end


% x1_T2 , x2_T2 states were overwritten in the BLOCK 3  "FOR" loop,
% and need to be recalculated beginning at the optimal transition point

clear global;                  % clear any pre-existing global variables
global PP QQ RR SS CC DD;      % pass system parameters to the function called
                               %below in ODE##, 4 var. reqd. for this system

% Dynamic System Parameter Coefficients
%%%%%%%%%%% Units: Lower ON, Upper OFF %%%%%%%%%%
% Note all parameters are divided by mass M
PP = (-2*K1meter)/((Lmeter^2)*M);

QQ = ( (4*F_PL)/(Lmeter*M) - 2*(Kpcsmeter/M) -...
      (K1meter/M)*6*(tan(theta_rad)^2) +...
          2*(K2/(Lmeter*M))*(F_B12_ON + F_B34_OFF) );

RR = 2*(K2/M)*tan(theta_rad)*(F_B12_ON - F_B34_OFF);
SS = -(B_Dmp/M);
CC = -Cfric/M;
DD = Dfric;
```

```
%Define Trajectory 2 initial condition at "SwitchPositionT2",
"SwitchVelocityT2"
x1_T2 = SwitchPositionT2;
x2_T2 = SwitchVelocityT2;

% % Initial state vector (Trajectory 2)
x0_T2 = [ x1_T2; x2_T2 ];

% Use ode23s to integrate the state equations (Stiff, Low to med. accuracy)
[t, x] = ode23s('Dynamic_EOM_FUNC_DmpFric', tvec, x0_T2);

% Extract states (just for readability)
x1_T2 = x(:,1);
x2_T2 = x(:,2);

% Plot State-Space Trajectory:
figure(3);
clf(3);
set(gca,'FontSize',20)
hold on;
grid on;

%Plot Trajectory 1-Short
plot(x1_T1_short,x2_T1_short,'r', 'LineWidth',4)

%Plot Trajectory 2-from initial condition (SwitchStepT2)
plot(x1_T2,x2_T2,'b', 'LineWidth',4)

xlim([-.0035 .0035])
ylim([-0.1 0.5])

title({'State-Space Trajectories (1) - (3) - (4)'; ...
      ['Damped: B = ', num2str(B_Dmp), ' N-sec/m']; ...
      ['Friction: C = ', num2str(Cfric), ' N']},'FontSize',30)
xlabel('x_1 = y (m)','FontSize',30)
ylabel('x_2 = ydot (m/sec)','FontSize',30)
legend('Lower Unit: OFF  ---  Upper Unit: OFF', ...
       'Lower Unit: ON  ---  Upper Unit: OFF');

TransitionT2 = get(gca,'YLim');
line([SwitchPositionT2
SwitchPositionT2],TransitionT2,'Color','k','LineStyle','--','LineWidth',3);
text(SwitchPositionT2, .375,' \leftarrow T1-T2 Optimal ...
     Transition','Fontsize',18,'HorizontalAlignment','left');

%Place darker lines over Y and X axes
Xaxis = get(gca,'XLim');
line(Xaxis,[0 0],'Color','k','LineStyle','--','LineWidth',2);
Yaxis = get(gca,'YLim');
line([0 0],Yaxis,'Color','k','LineStyle','--','LineWidth',2);

%%%%%%%%%%%%%%%%%%%%%%%%%%%%%%%%%%%%%%%%%%%%%%%%%%%%%%%%%%%%%%%%%%%%%%%%%%%%
%%%%%%%%%%%%%%%%%%%%%%%%%%%%%%%%%%%%%%%%%%%%%%%%%%%%%%%%%%%%%%%%%%%%%%%%%%%%



%% BLOCK 5
```

```
% Plot set of tertiary Trajectories from "optimal" Trajectory 2 I.C.
%  (i.e. state (3) - (4) - (5)'s), find optimal switching point 2 (T3)
& %trajectory 3

%Plot truncated Trajectory 1, Optimal Trajectory 2, then set of Traj. 3's
% New Figure
figure(4);
clf(4);
set(gca,'FontSize',20)
hold on;
grid on;

%Re-plot Trajectory 1-Short
plot(x1_T1_short,x2_T1_short,'r', 'LineWidth',4)

%re-plot Optimal Trajectory 2-from initial condition (SwitchStepT2)
plot(x1_T2,x2_T2,'b', 'LineWidth',4)

xlim([-.0035 .0035])
ylim([-0.1 0.5])

title({'State-Space Trajectories (1) - (3) - (4) - (5)'; ['Damped: B = ',
num2str(B_Dmp),  '  N-sec/m'];  ['Friction:  C  =  ',  num2str(Cfric),  '
N']},'FontSize',30)
xlabel('x_1 = y (m)','FontSize',30)
ylabel('x_2 = ydot (m/sec)','FontSize',30)


T2_final_step = length(x1_T2);    %number of points (steps) in Traj 2 curve

clear global;                  % clear any pre-existing global variables
global PP QQ RR SS CC DD;       % pass system parameters to the function called
                               %below in ODE##, 4 var. reqd. for this system

% Dynamic System Parameter Coefficients
%%%%%%%%%%% Units: Lower ON, Upper ON %%%%%%%%%%
% Note all parameters are divided by mass M
PP = (-2*K1meter)/((Lmeter^2)*M);

QQ = ( (4*F_PL)/(Lmeter*M) - 2*(Kpcsmeter/M) -...
      (K1meter/M)*6*(tan(theta_rad)^2) +...
          2*(K2/(Lmeter*M))*(F_B12_ON + F_B34_ON) );

RR = 2*(K2/M)*tan(theta_rad)*(F_B12_ON - F_B34_ON);
SS = -(B_Dmp/M);
CC = -Cfric/M;
DD = Dfric;

T3_init_step = 10;        %Number of steps to jump for each curve
j=0;                      %index "switch" for "FALSE" the nested if statement

for m = 1:T3_init_step:T2_final_step-1    %n = index for set of curves
                                          %corresponding to "Trajectory 2"

    %Trajectory 2 states at Step m
    x1_T3 = x1_T2(m);
```

```
    x2_T3 = x2_T2(m);

    % % Initial state vector (Trajectory 3)
    x0_T3 = [ x1_T3; x2_T3 ];


    % Use ode23s to integrate the state equations (Stiff, Low-med. accuracy)
    [t, x] = ode23s('Dynamic_EOM_FUNC_DmpFric', tvec, x0_T3);

    % Extract states (just for readability)
    x1_T3 = x(:,1);
    x2_T3 = x(:,2);

    % Plot State-Space Trajectory 3:
    plot(x1_T3,x2_T3,'g', 'LineWidth',1)


    if x2_T3(2) > x2_T2(m+1) && j<1
        fprintf('Optimal Switching Point is: \n');
        SwitchPositionT3 = x1_T2(m)
        SwitchVelocityT3 = x2_T2(m)
        SwitchStepT3 = m
        SwitchT3_Time = SwitchStepT3*tstep + SwitchT2_Time;
        fprintf(['Optimal 2nd Switching Time:  ',num2str(SwitchT3_Time), ...
                 ' seconds \n\n']);
        j = j+1;
    else
%         fprintf('Still searching...');
    end
end

% Legend and text below to come after last "plot" command in the block
legend('Lower Unit: OFF  ---  Upper Unit: OFF', ...
       'Lower Unit: ON  ---  Upper Unit: OFF', ...
       'Lower Unit: ON  ---  Upper Unit: ON');

%First Transition point
TransitionT2 = get(gca,'YLim');
line([SwitchPositionT2
SwitchPositionT2],TransitionT2,'Color','k','LineStyle','--','LineWidth',3);
text(SwitchPositionT2, .375,' \leftarrow T1-T2 Optimal
     Transition','Fontsize',18,'HorizontalAlignment','left');

%Second Transition point
TransitionT3 = get(gca,'YLim');
line([SwitchPositionT3
SwitchPositionT3],TransitionT3,'Color','k','LineStyle','--','LineWidth',3);
text(SwitchPositionT3, .275,' \leftarrow T2-T3 Optimal
     Transition','Fontsize',18,'HorizontalAlignment','left');

%Place darker lines over Y and X axes
Xaxis = get(gca,'XLim');
line(Xaxis,[0 0],'Color','k','LineStyle','--','LineWidth',2);
Yaxis = get(gca,'YLim');
line([0 0],Yaxis,'Color','k','LineStyle','--','LineWidth',2);

%%%%%%%%%%%%%%%%%%%%%%%%%%%%%%%%%%%%%%%%%%%%%%%%%%%%%%%%%%%%%%%%%%%%%%%%%%%%%%%
```

```
%%%%%%%%%%%%%%%%%%%%%%%%%%%%%%%%%%%%%%%%%%%%%%%%%%%%%%%%%%%%%%%%%%%%%%


%% BLOCK 6

%Plot truncated Trajectory 1 with Optimal Trajectory 2 then Optimal
%Trajectory 3

% x1_T2 , x2_T2 states have not been modified since BLOCK 3 (just truncate)
x1_T2_short = zeros(SwitchStepT3,1);     %create empty vectors of length equal
                                         %to SwitchStepT3
x2_T2_short = zeros(SwitchStepT3,1);

for mm = 1:1:SwitchStepT3          %Shorten Trajectory 2 state vectors to mm =
                                  %1 thru SwitchStepT3
    x1_T2_short(mm) = x1_T2(mm);
    x2_T2_short(mm) = x2_T2(mm);
end

% x1_T3 , x2_T3 states were overwritten in BLOCK 5  "FOR" loop, need to be
%recalculated beginning at the optimal transition point (T3)

clear global;                  % clear any pre-existing global variables
global PP QQ RR SS CC DD;       % pass system parameters to the function called
                               %below in ODE##, 4 var. reqd. for this system

% Dynamic System Parameter Coefficients
%%%%%%%%%%% Units: Lower ON, Upper ON %%%%%%%%%%%
% Note all parameters are divided by mass M
PP = (-2*K1meter)/((Lmeter^2)*M);

QQ = (  (4*F_PL)/(Lmeter*M) - 2*(Kpcsmeter/M) -...
      (K1meter/M)*6*(tan(theta_rad)^2) +...
          2*(K2/(Lmeter*M))*(F_B12_ON + F_B34_ON) );

RR = 2*(K2/M)*tan(theta_rad)*(F_B12_ON - F_B34_ON);
SS = -(B_Dmp/M);
CC = -Cfric/M;
DD = Dfric;

%Define Trajectory 3 initial condition at "SwitchPositionT3",
"SwitchVelocityT3"
x1_T3 = SwitchPositionT3;
x2_T3 = SwitchVelocityT3;

% % Initial state vector (Trajectory 2)
x0_T3 = [ x1_T3; x2_T3 ];

% Use ode23s to integrate the state equations (Stiff, Low to med. accuracy)
[t, x] = ode23s('Dynamic_EOM_FUNC_DmpFric', tvec, x0_T3);

% Extract states (just for readability)
x1_T3 = x(:,1);
x2_T3 = x(:,2);
```

```
% Euler Method Numerical Integration
%%%%%%%%%%%%%%%%%%%%%%%%%%%%%%%%%%%%%%%%%%%%%%%%%%%%%%%%%%%%%%%%%%%%%%%%%%%%
%Create vectors for position (y) and velocity (v) with length of tvec
y = zeros(totsteps,1);
v = zeros(totsteps,1);

% Starting state (Initial Conditions)
y(1) = SwitchPositionT3;    %mm
v(1) = SwitchVelocityT3;     %mm/sec

Y_Final = .0016079;    % meters Final y-position for integration upper bound
PrctBand = 0.005;    %+/-boundary of equilibrium point as a percentage of that
                     %y-position magnitude (underdamped - first crossing)

Y_Final = Y_Final*(1-PrctBand)
TimeAccum = SwitchT3_Time;

for i = 1:1:totsteps
    v(i+1) = (PP*(y(i)).^3 + QQ*y(i) + RR + SS*v(i) + CC*tanh(DD*v(i)))*tstep
+ v(i);
    y(i+1) = v(i)*tstep + y(i);

    if y(i+1) < Y_Final
        if v(i) == 0
            TimeAccum = TimeAccum + tstep;
        else
            deltaT = (y(i+1)-y(i))/v(i);
            TimeAccum = TimeAccum + deltaT;
        end
    else
        %do nothing
    end
end

TimeAccum;
TLast_steps = (TimeAccum - (SwitchT2_Time + SwitchT3_Time))/tstep;

fprintf(['Total Accumulated Transition Time: \n\n', num2str(TimeAccum), ...
         ' seconds \n\n\n']);
fprintf(['Time steps on last trajectory: \n\n', num2str(TLast_steps), ...
         ' steps \n\n']);


% Plot State-Space Trajectory:
figure(5);
clf(5);
set(gca,'FontSize',20)
hold on;
grid on;

%Plot Trajectory 1-Short
plot(x1_T1_short,x2_T1_short,'r', 'LineWidth',4)

%Plot Trajectory 2-Optimal-Short
plot(x1_T2_short,x2_T2_short,'b', 'LineWidth',4)

%Plot Trajectory 3-from initial condition (SwitchStepT3)
```

```
plot(x1_T3,x2_T3,'g', 'LineWidth',4)

%Plot Trajectory 3-EULER METHOD-from initial condition (SwitchStepT3)
plot(y,v,'k--', 'LineWidth',2)

xlim([-.0035 .0035])
ylim([-0.1 0.5])
title({'State-Space Trajectories (1) - (3) - (4) - (5)'; ...
      ['Damped: B = ', num2str(B_Dmp), ' N-sec/m']; ...
      ['Friction: C = ', num2str(Cfric), ' N']},'FontSize',30)
xlabel('x_1 = y (m)','FontSize',30)
ylabel('x_2 = ydot (m/sec)','FontSize',30)
legend('Lower Unit: OFF  ---  Upper Unit: OFF', ...
       'Lower Unit: ON  ---  Upper Unit: OFF', ...
       'Lower Unit: ON  ---  Upper Unit: ON', ...
       'Lower Unit: ON - Upper Unit: ON - Euler');

%First Transition point
TransitionT2 = get(gca,'YLim');
line([SwitchPositionT2
SwitchPositionT2],TransitionT2,'Color','k','LineStyle','--','LineWidth',3);
text(SwitchPositionT2, .375,' \leftarrow T1-T2 Optimal
     Transition','Fontsize',18,'HorizontalAlignment','left');

%Second Transition point
TransitionT3 = get(gca,'YLim');
line([SwitchPositionT3
SwitchPositionT3],TransitionT3,'Color','k','LineStyle','--','LineWidth',3);
text(SwitchPositionT3, .275,' \leftarrow T2-T3 Optimal
     Transition','Fontsize',18,'HorizontalAlignment','left');

%Place darker lines over Y and X axes
Xaxis = get(gca,'XLim');
line(Xaxis,[0 0],'Color','k','LineStyle','--','LineWidth',2);
Yaxis = get(gca,'YLim');
line([0 0],Yaxis,'Color','k','LineStyle','--','LineWidth',2);
```

References

[1] J. Huber, N. Fleck and M. Ashby, "The Selection of Mechanical Actuators Based on Performance Indices," *Proceedings of the Royal Society of London* , no. 453 (1965), pp. 2185-2205, 1999.

[2] J. Garcia-Bonito, M. Brennan, S. Elliot, A. David and R. Pinnington, "A novel high displacement piezoelectric actuator for active vibration control," *Smart Material Structures,* vol. 7, no. 31, pp. 31-42, 1998.

[3] R. C. Fenn, J. R. Downer, D. A. Bushko, V. Gondhalekar and N. D. Ham, "Terfenol-D driven flaps for helicopter vibration reduction," *Smart Material Structures,* vol. 5, pp. 49-57, 1996.

[4] E. F. Prechtl and S. R. Hall, "Design of a high efficiency, large stroke, electromechanical actuator," *Smart Material Structures,* vol. 8, no. 13, pp. 13-30, 1999.

[5] K.-B. Choi, J. Jong Lee and S. Hata, "A piezo-driven compliant stage with double mechanical amplification mechanisms arranged in parallel," *Sensors and Actuators A,* vol. 161, pp. 173-181, 2010.

[6] C. Niezrecki, D. Brei, S. Balakrishnan and A. Moskalik, "Piezoelectric Actuation: State of the Art," *The Shock and Vibration Digest,* vol. 33, no. 4, pp. 269-280, July 2001.

[7] K. Uchino, "Piezoelectric ultrasonic motors: overview," *Smart Material Structures,* vol. 7, pp. 273-285, 1998.

[8] S. Tsukahara, L. Penalver-Aguila, J. Torres and H. Asada, "Design of a Piezoelectric Poly-Actuated Linear Motor," in *Proceedings of the 2013 ASME Dynamic Systems and Controls Conference*, Palo Alto, Oct. 2013.

[9] H.-W. Ma, S. M. Yao, L.-Q. Wang and Z. Zhong, "Analysis of the displacement amplification ratio of bridge-type flexure hinge," *Sensors and Actuators A,* vol. 132, pp. 730-736, 2006.

[10] D. Neal and H. Asada, "Bipolar Piezoelectric Buckling Actuators," *IEEE/ASME Transactions on Mechatronics,* vol. 19, no. 1, pp. 9-19, 2014.

[11] D. Neal and H. Asada, "Nonlinear, Large-Strain PZT Actuators Using Controlled Structural Buckling," in *Proceedings of the IEEE International Conference on Robotics and Automation*, Kobe, 2009.

[12] J. Torres, S. Tsukahara and H. Asada, "Maximizing Output Work of PZT Stacks While Gaining Large Displacement Amplification," in *Proceedings of the 2013 IEEE International Conference on Robotics and Automation*, Karlsruhe, May 2013.

[13] D. Neal and H. Asada, "Phased-Array Piezoelectric Actuators Using a Buckling Mechanism Having a Large Displacement Amplification And Nonlinear Stiffness," in *Proceedings of the 2010 IEEE International Conference on Robotics and Automation*, May 2010.

[14] J. Torres and H. Asada, "A Non-Flexure Type Displacement Amplification Mechanism for Piezoelectric Stack Actuators Utilizing Rolling Contact Joints," in *IEEE International Conference of Robotics and Automation*, 2013.

[15] J.-J. E. Slotine and W. Li, "Phase Plane Analysis," in *Applied Nonlinear Control*, Englewood Cliffs, New Jersey, Prentice-Hall, 1991, pp. 17-39.

[16] S. C. Chapra and R. P. Canale, "Runge-Kutta Methods," in *Numerical Methods for Engineers*, New York, McGraw-Hill, 2002, pp. 682-692.